Superconducting Properties from First Principles Calculations: An Ab-Initio Study of the properties of Superconductors under Perturbations

BYRNE, PETER,JOHN,PHARES

Superconducting Properties from First Principles Calculations:

An *Ab-Initio* Study of the properties of Superconductors under Perturbations

Peter John Phares Byrne

A thesis submitted in partial fulfilment

of the requirements for the degree of

Doctor of Philosophy

The University of Durham

Department of Physics

2017

Abstract

Superconductors are commonly used in many magnet systems available today. One of the most popular is Nb_3Sn, due to its high upper critical field and uncomplicated structure. It is however, not particularly well understood at the microscopic scale with respect to grain boundaries and strain. Grain boundaries appear when forming the material and are used as an effective way to increase the upper critical field by increasing the normal state resistivity, but there is a trade-off, as the critical current density drops as the material becomes more disordered. In addition, when the material is strained by magnetic fields, the superconducting properties will vary. Much experimental work has been performed to study these experimental effects, but a first-principles study gives a unique insight into the intrinsic properties of the material itself. This thesis gives a record of investigations into the strain and grain boundary dependence of Nb_3Sn as well as determining whether we can use density functional theory to determine superconducting properties from first principles. This work includes an efficient implementation of a method to calculate the electron-phonon coupling matrix elements from first principles via density functional perturbation theory. This method is tested on some simple metallic elements and shown to provide coupling strengths close in agreement to experimental work.

Acknowledgements

First and foremost, I would like to thank my supervisor Stewart Clark for his help and comments over the last few years. I would also like to thank my co-supervisor Damian Hampshire for adding experimental insight into the investigation, and everybody from the Durham condensed matter group. In particular, I would like to thank Thomas Hollins and Paul Tulip for enlightening conversations and the occasional rant. Outside of work, I would like to thank my friends and family for all the support they have given me throughout.

Work to be Published

The work here will be published in the following papers which are being prepared for submission.

- *Symmetric Tilt Grain Boundaries in Nb_3Sn and Au from Density Functional Theory*, P. J. P. Byrne, S.J.Clark
- *Calculation of Electron-Phonon Coupling from First Principles in CASTEP*, P. J. P. Byrne, S.J.Clark
- *Calculation of the Superconductivity-Strain Function for Nb_3Sn from First Principles*, P. J. P. Byrne, S.J.Clark

Declaration

The work presented here was undertaken within the Department of Physics at the University of Durham between October 2010 and October 2016. I confirm that no part of this work has previously been submitted for a degree at this or any other institution and, unless otherwise stated, it is the original work of the author.

Contents

1 Introduction **19**

1.1 Superconductivity 19

1.2 Thesis Outline 21

2 Theory **24**

2.1 Introduction 24

2.2 Ground State Electronic Structure 25

2.2.1 Many-body Schrödinger Equation 25

2.2.2 Born-Oppenheimer Approximation 26

2.2.3 Density Functional Theory 30

2.2.4 Exchange and Correlation 32

2.2.5 Exchange and Correlation(XC) Functionals 33

2.2.6 Periodic Boundary Conditions 34

2.2.7 Bloch's Theorem and Plane Wave Basis Sets 35

2.2.8 Pseudopotentials 36

2.3 Dynamics of Nuclear Motion 39

2.3.1 Introduction 39

2.3.2 Lattice Dynamics 39

2.3.3 Boundary Conditions 41

2.3.4 Solving the Dynamical Matrix 42

2.3.5 Derivatives of the Total Energy 43
2.3.6 Perturbation Theory 43
2.3.7 Metals 46
2.3.8 Electron-Phonon Coupling 50

3 Ground State Calculations in Practice 53
3.1 Introduction 53
3.2 Ground State 53
3.2.1 Total Energy and Density 54
3.3 Basis Sets 54
3.3.1 Wavefunctions 56
3.3.2 Real Space Grids 57
3.3.3 Reciprocal Space Sampling 59
3.4 Orthonormality 59
3.5 Minimization 60
3.5.1 Steepest Descents 61
3.5.2 Conjugate Gradients 62
3.5.3 Preconditioning 63
3.5.4 Charge Sloshing and Density Mixing 63
3.5.5 Occupancy and Fermi Energy 65
3.5.6 Convergence Tolerance 66
3.6 Symmetry 66
3.7 Conclusion 67

4 Electron-Phonon Coupling 69
4.1 Introduction 69
4.2 Ground State 69
4.3 Fermi Surface 70

4.4 Perturbation . . . 73
4.5 Finite Displacement . . . 73
4.6 Linear Response . . . 74
4.6.1 Full Sternheimer Equation in Bloch form . . . 74
4.6.2 Brillouin Zone Sampling . . . 75
4.6.3 Solving the Sternheimer Equation . . . 76
4.6.4 Second-Order Energy . . . 76
4.7 Electron-Phonon Coupling . . . 76
4.8 Symmetry . . . 77
4.8.1 Finding Symmetry Operations . . . 79
4.9 Interpolation . . . 80
4.10 Acoustic Sum Rule . . . 81
4.11 Convergence . . . 82
4.11.1 Basis Set Size . . . 83
4.11.2 Brillouin Zone Sampling . . . 86
4.11.3 Optimisation . . . 88
4.12 Calculation Summary . . . 89

5 Grain Boundaries in Au and Nb_3Sn 91

5.1 Introduction . . . 91
5.2 Periodic Grain Boundaries . . . 94
5.3 Commensurate Site Lattice . . . 95
5.3.1 Materials Studied . . . 96
5.4 Results . . . 100
5.4.1 Grain Boundaries in Gold . . . 100
5.4.2 Impurities in Au Grain Boundaries . . . 102
5.4.3 Grain Boundaries in Nb_3Sn . . . 105
5.5 Discussion . . . 110

5.5.1 Gold 110
5.5.2 Nb_3Sn 114
5.6 Conclusion 116

6 Nb Low Temperature Phase **118**
6.1 Introduction 118
6.2 Method 119
6.3 Results 120
6.4 Discussion 123
6.5 Conclusion 123

7 Electron-Phonon Coupling in Simple Metals **125**
7.1 Calculation of the Eliashberg Spectral Function 126
7.1.1 Splitting the Eliashberg Spectral Function 127
7.2 Modified McMillan Transition Temperature 129
7.3 Materials Studied 131
7.4 Method 132
7.5 Results 133
7.5.1 Structure 133
7.5.2 Electronic Properties 134
7.5.3 Phonon DOS 138
7.5.4 Spectral Function and Superconducting Transition Temperature 143
7.6 Discussion 147
7.6.1 Structure 147
7.6.2 Electronic Properties 147
7.6.3 Phonon Properties 148
7.6.4 Electron-Phonon Coupling 149

7.7 Conclusion 150

8 Nb_3Sn under Uni-Axial Strain **151**

8.1 Background 151

8.2 Strain 153

8.3 Literature Review 153

8.3.1 Method 154

8.3.2 Results 156

8.3.3 Strain 160

8.3.4 Phonon Spectral Function 162

8.3.5 Discussion 168

8.3.6 Strain 169

8.4 Conclusions 172

9 Conclusion **175**

Bibliography **179**

List of Figures

2.1 The all electron(dashed) and pseudo-partial(solid) wavefunctions from a pseudopotential for Sn. Only the 5s(red) and 5p(blue) electrons are considered as valence. The cutoff radius is shown as a dashed line at 2.28 Bohr. 38

2.2 The Fermi surface for Au shown within the first Brillouin zone. 47

3.1 A flowchart showing the process used to calculate the ground state density and total energy. 55

4.1 A 2d example of how the Fermi surface finding algorithm works for a spherical Fermi surface in a system with 1 band crossing the Fermi surface. Brillouin zone k-points are shown as circles. Red circles indicate the k-point has an occupation number 1 less than in blue circles. The green shaded area is the regions in which a band must cross the Fermi energy. . . 72

4.2 An example of the effects of enforcing the acoustic sum rule on an under-converged phonon spectrum in Nb_3Sn. One coarse and fine sampling dispersion curve are shown in blue and red respectively. The linear dispersion at the zone centre as calculated from the ground state is shown in dashed lines. The anomaly is circled at the M point. 83

4.3 Frequency of the 3 phonon branches in Au as a function of cutoff energy used at an arbitrary $\mathbf{q} = (0.1, 0.2, 0.3)$. The Brillouin zone sampling grid was $18 \times 18 \times 18$. to ensure that the calculation was converged with respect to BZ sampling. 84

4.4 Modulus of the electron-phonon matrix element calculated between two arbitrary bands for the phonon branches shown in figure 4.3. The phase information was discarded as only the amplitude is necessary to find transition probabilities for electron-phonon scattering events. 85

4.5 Comparison of the computational time with the cutoff energy used in the calculations. Plotted also is an E_{cut}^2 fit to the graph displaying the superlinear scaling of the calculation. The calculation was performed in serial to negate the effects of interprocess communication. 85

4.6 Frequency of the 3 phonon branches in Au as a function of Brillouin zone sampling grid ($N \times N \times N$) used at an arbitrary $\mathbf{q} = (0.1, 0.2, 0.3)$. The cutoff energy was set at 600 eV 87

4.7 Modulus of the electron-phonon matrix element calculated between two arbitrary bands for the phonon branches shown in figure 4.6. The phase information was discarded as only the amplitude is necessary to find transition probabilities for electron-phonon scattering events. 87
4.8 The process used to calculate the electron-phonon matrix elements from the ground state wavefunctions. 90

5.1 The simplest Σ5 grain boundary in a simple cubic material with rotations about the c-axis (into the plane). It involves a mismatch angle of 53.13°. Figure a.) shows the original unit cell and the generating vector (1 2 0). Figure b.) shows two crystals rotated in opposite directions by half of this amount overlapped. Shown in black are the overlaps of atoms. Finally, Figure c.) shows the resulting periodic grain boundary in its simplest form. 96
5.2 The second Σ5 grain boundary in a simple cubic material with rotations about the c-axis (into the plane). It involves a mismatch angle of 36.87° . Figure a.) shows the original unit cell and the generating vector (1 3 0). Figure b.) shows two crystals rotated in opposite directions by half of this amount overlapped. Shown in black are the overlaps of atoms. Finally, Figure c.) shows the resulting periodic grain boundary in its simplest form including the extra commensurate lattice site in the centre of the unit cells. 97
5.3 The unit cell of Nb_3Sn with Sn atoms at the corners and the centre and Nb atoms arranged on the sides as ribbons. . . . 98

5.4 The periodic unit cell for an asymmetric Σ5 grain boundary in Au. The cubic unit cell is shown in the top left with a lattice parameter of 4.078 ÅAn example of the commensurate site lattice is shown as the larger square in the centre. As expected, the CSL cell has a volume of 5 times that of the simple unit cell. 99

5.5 The density of states in fcc Au decomposed into angular momentum channels around atomic sites. 101

5.6 The density of states of the two Σ5 symmetric tilt grain boundaries plotted against the bulk density of states for pure fcc Au. The energy is given relative to the Fermi energy(0 eV). The DOS has been normalised per unit volume to allow comparison between different GB volumes. 103

5.7 The density of states of the larger symmetric Σ13 tilt grain boundary compared with that of the perfect bulk Au crystal. The energies are relative to the Fermi energy. 104

5.8 A comparison of the volume normalised density of states in the symmetric and asymmetric Σ5 grain boundaries in Au. . 105

5.9 The density of states of a symmetric Σ5 with Ag and Ne impurities introduced in the grain boundary region. The energy scale is given relative to the Fermi energy. 106

5.10 The localised states corresponding to the Ne atoms placed in the GB are shown in blue. The Au atoms are shown in gold and the Ne atoms in blue. 106

5.11 The total density states of Nb_3Sn compared with the partial density of states for each of the Sn and Nb atoms in the pure A15 structure. Every atom of each species is symmetry equivalent in the structure and has the same pDOS. 107

5.12 The density of states of bulk Nb_3Sn compared with that from the two main types of $\Sigma 5$ grain boundary which could be created. The Fermi energy is marked at 0 eV. 108

5.13 The partial density of states at the Fermi energy associated with each atom in the grain boundary relative to the bulk value. The origin has been shifted so that the grain boundaries are at $\frac{1}{4}$ and $\frac{3}{4}$ of the horizontal axis. The local DOS was found by projecting the total DOS onto atomic orbitals centred around each atom. 109

5.14 Example of atomic relaxation in Nb_3Sn for the GB with Sn on the CSL lattice site. a.) Unrelaxed unit cell, which is effectively two bulk regions with different orientations. b.) Relaxed unit cell where atoms were free to move to the local minimum. Only the atoms very close to the grain boundary show any noticable change. 111

5.15 a.) The total ground state density of the $\Sigma 5$ grain boundary in Nb_3Sn. b.) An example of the electron density of orbitals whose eigenvalues cross the Fermi energy. c.) The electron density from the KS orbitals whose eigenvalues lie just above the Fermi energy. 112

6.1 Phonon dispersion curves for the bcc-form of Nb. It was calculated with an energy cut-off of 700 eV and a Brillouin zone sampling grid of $40 \times 40 \times 40$. Negative phonon frequencies are used to indicate imaginary phonon modes. 121

6.2 Phonon dispersion curves for the relaxed low temperature structure of Nb. The special points used the same points from the bcc structure. It was calculated with an energy cut-off of 700 eV and a Brillouin zone sampling grid of $40 \times 40 \times 40$. . 122

6.3 The phonon density of states of both bcc and rhombohedral($R\bar{3}M$) structures of Nb. These were sampled at wavevectors on a $40 \times 40 \times 40$ grid in the Brillouin zone. Negative phonon frequencies indicate modes which are unstable. 122

7.1 Demonstration of the interpolation of the EP coupling strength as a function of frequency. The bins show the average EP matrix element magnitude across 200 sample points. 129

7.2 The electronic band structure and density of states for Au. The DOS was sampled on a grid of $50 \times 50 \times 50$. The band structure was sampled on points that were a maximum of 0.01 Å apart. 134

7.3 The electronic band structure and density of states for Zr. The density of states was sampled on a grid of $50 \times 50 \times 50$. The band structure was sampled on points that were a maximum of 0.01 Å apart. 135

7.4 The electronic band structure and density of states for Nb. The density of states was sampled on a grid of $50 \times 50 \times 50$. The band structure was sampled on points that were a maximum of 0.01 Å apart. 136

7.5 The electronic band structure and density of states for Mo. The density of states was sampled on a grid of 50 × 50 × 50. The band structure was sample on points that were a maximum of 0.01 Å apart. 137
7.6 The phonon dispersion and density of states for Au. DFPT calculations were computed for phonon wavevectors on a 9 × 9 × 9 grid across the Brillouin zone and interpolated to find the dispersion and DOS. 139
7.7 The phonon dispersion and density of states for Nb. DFPT calculations were computed for phonon wavevectors on a 12 × 12 × 12 origin-shifted grid across the Brillouin zone and interpolated to find the dispersion and DOS. 140
7.8 The phonon dispersion and density of states for Mo. DFPT calculations were computed for phonon wavevectors on a 10 × 10 × 10 origin-shifted grid across the Brillouin zone and interpolated to find the dispersion and DOS. 141
7.9 The phonon dispersion and density of states for Zr. DFPT calculations were computed for phonon wavevectors on a 24 × 24 × 20 origin-shifted grid across the Brillouin zone and interpolated to find the dispersion and DOS. 142
7.10 The Eliashberg spectral function for Au. 143
7.11 The Eliashberg spectral function for Nb. 144
7.12 The Eliashberg spectral function for Mo. 145
7.13 The Eliashberg spectral function for Zr. 145

8.1 Schematic of one of the common structures for Nb_3Sn wires. 152
8.2 Crystal structure of Nb_3Sn which consists of a bcc Sn cell with Nb ribbons running along the edges. 155

8.3 The band structure and density of states for cubic Nb_3Sn for a path across the Brillouin zone. 157
8.4 The Fermi surface for Nb_3Sn with bands going from a.) lowest to f.) highest Kohn-Sham index. Of note are the similar bands around the edges of the BZ which are almost parallel and close together which allow additional low energy scattering interactions. This calculation was performed with a $40 \times 40 \times 40$ MP grid across the BZ. 158
8.5 The phonon dispersion spectrum for cubic Nb_3Sn is shown in red for a path across the Brillouin zone. The dashed lines indicate accoustic modes around the Γ-point that were calculated by the linear displacement method. The lower of these modes is the transverse accoustic mode and the higher mode is the longitudinal mode (speed of sound). 159
8.6 The unrestricted lattice parameter compared with the fixed (strained) lattice parameter. Shown in red is the line where the lattice parameters are equal. 160
8.7 Comparison of the δ value (a measure of the distortion of the Nb ribbons) with the strain for the full range of pressures. . 161
8.8 A sample of the DOS around the Fermi energy with decreasing strain values from the cubic point, calculated by sampling the Brillouin zone on a grid of $40 \times 40 \times 40$ 162
8.9 A sample of the DOS around the Fermi energy with increasing strain values from the cubic point calculated by sampling the Brillouin zone on a grid of $40 \times 40 \times 40$ 163
8.10 The overall effect of strain on the DOS at the Fermi energy in Nb_3Sn for the range of strain values from -1% to $+0.5\%$. 163

8.11 The phonon spectral function, $F(\omega)$ for decreasing values of the strain from just below the cubic point. These values were interpolated from a grid of $4 \times 4 \times 4$ samples of the 2nd order energy across the Brillouin zone. 164

8.12 The phonon spectral function, $F(\omega)$ for values approaching the cubic point from compression. These values were interpolated from a grid of $4 \times 4 \times 4$ samples of the 2^{nd} order energy across the Brillouin zone. 165

8.13 The phonon spectral function, $F(\omega)$ for increasing values of the strain from the cubic point. These values were interpolated from a grid of $4 \times 4 \times 4$ samples of the 2nd order energy across the Brillouin zone. 166

8.14 The value of $\int \frac{F(\omega)}{\omega} d\omega$ plotted against the strain. 167

8.15 The electron-phonon strain function for Nb_3Sn around the cubic point. These values have been normalised to the highest value as that is commonly used as the zero strain point in experimental work. 167

Chapter 1

Introduction

1.1 Superconductivity

Much of the high impact science performed today depends on being able to produce large magnetic fields. For example, the fusion project ITER and the particle accelerators at the Large Hadron Collider all need strong magnetic fields to contain charged particles. The efficiency of these machines relies on the use of superconductors to carry currents with little loss of energy.

Superconductors are materials which exhibit no resistance below their transition(or critical) temperature. They were first discovered in 1911 by Heike Kamerlingh Onnes who previously had been the first to liquefy helium in 1908. Upon cooling of mercury below 4.2 K, the electrical resistance suddenly vanished. This was found to occur for different materials at different temperatures and some did not show this property at all. The name superconductor is distinguished from perfect conductors. The defining property of a superconductor is that it acts to expel any magnetic field from its interior whereas a perfect conductor can have any internal field so long as it is constant[1].

It was many years before a microscopic theory of superconductivity came about, in the form of BCS theory[2], which was realised by John Bardeen, Leon Cooper, and John Robert Schrieffer in 1957. Cooper had shown[3] that, with any attractive potential, electrons near the Fermi energy will form bound pairs. Due to the isotope effect, this attraction was thought to be linked to the electron-phonon coupling in the material. This coupling causes non-localised pairs to form which have a large overlap with other cooper pairs in the material. Due to this overlap, the amount of energy required to break one of the pairs can be larger than that of thermal atomic motion. The thermal energy from phonons is not large enough to break these pairs and so the electron pairs move with effectively no scattering.

This theory was a success in describing 'low temperature' superconductors. The BCS theory predicted a maximum temperature for superconductors on the order of 30 K[1]. The first high temperature superconductor, Lanthanum barium copper oxide, with a transition temperature above this limit, was discovered in 1986[4]. These materials are believed to have a different mediator than the electron-phonon interaction as their transition temperatures are much higher than the predicted upper limit for BCS superconductors, and are not fully understood at present.

Although it is easy to characterise the bulk properties of superconductors experimentally, it is difficult to directly measure microscopic superconducting properties of the materials at very low temperatures. Many of the materials with high transition temperatures or high critical magnetic fields are ceramic and therefore brittle and are produced in a composite wire with many defects and so it is difficult to separate the intrinsic and extrinsic effects in an experiment.

Rather we would like to study the materials from a computational per-

spective using density functional theory(DFT) which allows us to solve the Schrödinger equation for materials which gives us insight about ground state properties. As superconducting properties are dynamic, we combine DFT with perturbation theory to access information about phonon modes. The interaction of these modes with the ground state electronic structure can give us the leading terms to describe the electron-phonon interaction in BCS theory. With knowledge of the average electron-phonon interaction in the material, BCS theory gives us a way to predict the superconducting transition temperature. These calculations allow us to easily access properties which would be difficult in practice, such as changes in the phonon frequencies due to strain in ceramic materials such as Nb_3Sn.

All equations will be given in atomic units unless otherwise stated. Upper and lower case indices refer to nuclear and electronic coordinates respectively.

1.2 Thesis Outline

In this work, we seek to perform electronic structure calculations to compute superconducting properties from first principles. The chapter overviews are as follows:

Chapter 2

The many body Schrödinger equation is introduced and developed into the density functional theory framework for ground state calculations. The application of Bloch's theorem and the conversion from direct space to reciprocal space is discussed, along with a number of approximations used, including the choice of exchange-correlation functional and pseudo potentials. This framework is then expanded to examine perturbations in materials un-

der the harmonic approximation and the definition of the electron-phonon coupling constant.

Chapter 3

The method of computing the calculation of ground state properties in CASTEP is given. The representation of wavefunctions and densities are discussed. Methods for maintaining orthonormality and performing total-energy minimization are given. The effects of symmetry on the memory and processing requirements are also given.

Chapter 4

The implemented method of computing the phonon dispersion and electron-phonon coupling of a material is shown. Practical details including how the Fermi surface is found and how the electron-phonon matrix elements are calculated are given. Also discussed are the effects of symmetry in reducing the number of perturbative calculations that need to be performed.

Chapter 5

The chapter details a study of the effect of grain boundaries in Au and Nb_3Sn. The main quantity of interest is the electronic density of states at the Fermi energy and this is studied both across the whole region and as a function of distance across the grain boundary. This quantity is of interest as it is directly related to the superconducting critical temperature and gives information about which regions act as normal in a polycrystalline sample.

Chapter 6

The room-temperature body-centered cubic phase of Nb is shown to be unstable at low temperatures. A new rhombohedral state is investigated and compared with recent experimental results from the literature.

Chapter 7

The electron-phonon coupling is calculated for a range of simple metals purely from first principles. The ground state properties, phonon dispersion curves and Eliashberg spectral functions are discussed. The expected superconducting transition temperatures are also calculated.

Chapter 8

The effects of uni-axial strain in Nb_3Sn are examined with respect to the electron-phonon coupling. A range of strains from -1% to +0.5% were simulated and allowed to relax to their lowest energy geometries. Electronic and phononic properties were then calculated, and combined to estimate the overall effects on the electron-phonon coupling.

Chapter 9

In this chapter, general conclusions are presented for the chapters along with ideas for further work and investigation.

Chapter 2

Theory

2.1 Introduction

At the ångström-scales of atomic interactions, effects are very much in the quantum regime and described by quantum mechanics. At the heart of this is the many body Schrödinger equation. In its unadulterated form, it is intractable to solve directly so approximations are required to allow ground state solutions to be found. Approximations in this chapter will lead us to Hohenberg–Kohn–Sham density functional theory(DFT).

In this work, perturbation theory is used to study dynamical effects close to these ground state solutions. In particular, to look at the effects of the nuclear motion on the electronic structure and how an effective interaction between phonons and electrons can be calculated. Finally quantum field theoretical techniques can be used to link this effective electron-phonon interaction to macroscopic properties of materials and this is discussed.

The primary goal of study is to calculate how structural changes, stresses and deformations in materials may change the superconducting properties.

2.2 Ground State Electronic Structure

2.2.1 Many-body Schrödinger Equation

The (non-relativistic) Schrödinger Equation describes the behaviour of small-scale physical systems — effectively those where gravity is not a factor and velocities are much lower than the speed of light. The general form for a system of nuclei and electrons is the time dependent equation,

$$i\hbar\frac{\partial}{\partial t}\Psi\left(\{\mathbf{r}_i\},\{\mathbf{R}_I\},t\right)=\hat{H}\Psi\left(\{\mathbf{r}_i\},\{\mathbf{R}_I\},t\right), \tag{2.1}$$

where $\hbar$ is Planck's constant (1 in atomic units), $\mathbf{r}_i$ is the coordinate of electron i, $\mathbf{R}_j$ is the coordinate of nucleus j, Ψ is the full many body wavefunction, which includes both electronic and nuclear coordinates, and $\hat{H}$ is the Hamiltonian operator. This equation is unwieldy due to the large number of dimensions involved ($3n_{electrons}+3N_{atoms}+1$) and the resulting wavefunctions can be difficult to interpret due to the time evolution. Rather than solve this equation directly, we solve for the stationary states (or orbitals) given by the time independent equation,

$$E\Psi\left(\{\mathbf{r}_i\},\{\mathbf{R}_I\}\right)=\hat{H}\Psi\left(\{\mathbf{r}_i\},\{\mathbf{R}_I\}\right), \tag{2.2}$$

where E is the total ground state energy of the system. These stationary states can be combined with the time evolution equation ($H\Psi=i\frac{\partial\Psi}{\partial t}$). If we limit ourselves to dealing with nuclei and electrons, we can explicitly write

the Hamiltonian,

$$\begin{aligned}\hat{H} &= \hat{T}^N + \hat{T}^e + \hat{V}^{NN} + \hat{V}^{Ne} + \hat{V}^{ee} \\ &= -\frac{1}{2}\sum_I \frac{1}{M_I}\nabla^2_{\mathbf{R}_I} - \frac{1}{2}\sum_i \nabla^2_{\mathbf{r}_i} \\ &+ \sum_{I>J} \frac{Z_I Z_J}{|\mathbf{R}_I - \mathbf{R}_J|} - \sum_{i,J} \frac{Z_J}{|\mathbf{r}_i - \mathbf{R}_J|} + \sum_{i>j} \frac{1}{|\mathbf{r}_i - \mathbf{r}_j|}\end{aligned} \tag{2.3}$$

where $\hat{T}$ is the kinetic energy operator, and $\hat{V}$ is the potential produced by the 3 distinct interactions – nuclear-nuclear, nuclear-electron and electron-electron. Z_I, M_I and $\mathbf{R}_I$ are the atomic number, mass and position of nucleus I and $\mathbf{r}_i$ is the position of electron i.

The ground state is the state of lowest energy, and this can be found by minimization of the functional,

$$E_{gs} = \min_{\Psi} E[\Psi] = \min_{\Psi} \frac{\left\langle \Psi \middle| \hat{H} \middle| \Psi \right\rangle}{\langle \Psi | \Psi_. \rangle} \tag{2.4}$$

Equations 2.2 and 2.3 have a large number of degrees of freedom; it is a partial differential differential equation in $3N_{nuclei} + 3N_{electrons}$ dimensions. This grows quickly for any realistic system and so some simplifications are required.

2.2.2 Born-Oppenheimer Approximation

We begin with the adiabatic assumption that the nuclear state is frozen in some configuration that the electrons explore. One argument for this is that the nuclei move on much longer time scales and so the electrons will effectively move into the lowest energy state much more quickly than the atoms react. Alternatively, this can be phrased that the motion of the ions is so slow as to allow the electrons, in a spin unpolarised system, to always

find the minimum energy state for any atomic configuration.

We start by making an ansatz for the form of the full wavefunction, Ψ, which can be written due to this argument as a nuclear part and an electronic part that has a parametric dependence on the nuclear state,

$$\Psi\left(\{\mathbf{r}_i\},\{\mathbf{R}_I\}\right) = \psi^N\left(\{\mathbf{R}_I\}\right) \times \psi^e_{\mathbf{R}}\left(\{\mathbf{r}_i\}\right). \tag{2.5}$$

The parametric dependence of the electronic wavefunction upon the nuclear coordinates is expressed by the subscript $\mathbf{R}$. We then define an electronic Hamiltonian, which is simply the parts of the total Hamiltonian which act on electron coordinates,

$$\hat{H}^e_{\mathbf{R}} = \hat{T}^e + \hat{V}^{Ne}_{\mathbf{R}} + \hat{V}^{ee}. \tag{2.6}$$

Writing a version of the Hamiltonian for the electronic wavefunction, we get an electronic Schrödinger equation,

$$\hat{H}^e_{\mathbf{R}}\psi^e_{\mathbf{R}}\left(\{\mathbf{r}_i\}\right) = E^e_{\mathbf{R}}\psi^e_{\mathbf{R}}\left(\{\mathbf{r}_i\}\right). \tag{2.7}$$

The full Hamiltonian is expressed as

$$\hat{H} = [\hat{T}^N + \hat{V}^{NN}] + \hat{H}^e_{\mathbf{R}}. \tag{2.8}$$

Applying the full Hamiltonian to the wavefunction product, Ψ, we see that only the nuclear kinetic energy operator acts directly on the electronic

wavefunction through the product rule,

$$\begin{aligned}\hat{T}^N\psi^N\psi^e_{\mathbf{R}} &= -\sum_I \frac{1}{2M_I}\frac{\partial^2}{\partial\mathbf{R}_I^2}\psi^N\psi^e_{\mathbf{R}} \\ &= -\sum_I \frac{1}{2M_I}\left[\frac{\partial^2\psi^N}{\partial\mathbf{R}_I^2}\psi^e_{\mathbf{R}} + 2\frac{\partial\psi^N}{\partial\mathbf{R}_I}\frac{\partial\psi^e_{\mathbf{R}}}{\partial\mathbf{R}_I} + \psi^N\frac{\partial^2\psi^e_{\mathbf{R}}}{\partial\mathbf{R}^2}\right].\end{aligned}$$

The full result can be rewritten in a more familiar form,

$$\begin{aligned}\hat{H}\Psi &= \hat{T}^N\psi^N\psi^e_{\mathbf{R}} + \hat{V}^{NN}\psi^N\psi^e_{\mathbf{R}} + E^e_{\mathbf{R}}\psi^N\psi^e_{\mathbf{R}} \\ &= \psi^e_{\mathbf{R}}\left[-\sum_I \frac{1}{2M_I}\frac{\partial^2}{\partial\mathbf{R}_I^2} + V(\{\mathbf{R}_I\}) + E^e_{\mathbf{R}}\right]\psi^N \\ &\quad - \sum_I \frac{1}{2M_I}\left[2\frac{\partial\psi^N}{\partial\mathbf{R}_I}\frac{\partial\psi^e_{\mathbf{R}}}{\partial\mathbf{R}_I} + \psi^N\frac{\partial^2\psi^e_{\mathbf{R}}}{\partial\mathbf{R}_I^2}\right].\end{aligned} \tag{2.9}$$

The final two terms in 2.9 present a problem as they couple the electronic and nuclear wavefunctions. They introduce coupling between nearby nuclear states. We can find a loose approximation for the size of the last term, as it should be of the same order as the derivative with respect to the electronic positions as they are across the same length scales[5],

$$\frac{1}{2M_I}\frac{\partial^2\psi^e_{\mathbf{R}}}{\partial\mathbf{R}_I^2} \sim \frac{1}{2M_I}\frac{\partial^2\psi^e_{\mathbf{R}}}{\partial\mathbf{r}_i^2} = \frac{p_e^2}{2M_I}\psi^e_{\mathbf{R}} = \frac{m_e}{M_I}E_e\psi^e_{\mathbf{R}},$$

where E_e is the kinetic energy of an average electron. This term is of the order m/M which will be very small and can be ignored with little loss of accuracy in systems without light elements.

The second last term is the more interesting. It affects both the electronic and nuclear coordinates. For a stationary nuclear state, this term is equal to the rate of change of total charge of the system with respect to the nuclear coordinates, which is obviously zero. For dynamical systems, it acts as a coupling between excitations of the nuclear and electronic wavefunctions and

we can define an electron-phonon operator,

$$-\sum_I \frac{1}{M_I}\frac{\partial\psi^N}{\partial\mathbf{R}_I}\frac{\partial\psi^e_{\mathbf{R}}}{\partial\mathbf{R}_I} = \hat{H}^{ep}\psi^N\psi^e_{\mathbf{R}}, \tag{2.10}$$

which acts on both the nuclear and electronic wavefunctions. We will return to this operator in the discussion of electron-phonon coupling in chapter 3. For the purpose of our calculations, this term is ignored and then reintroduced via perturbation theory as it is difficult to calculate directly as it would require perturbations in both nuclear and electronic wavefunctions.

Ignoring the coupling terms, we can write,

$$\left[-\sum_I \frac{1}{2M_I}\frac{\partial^2}{\partial\mathbf{R}_I^2} + V(\{\mathbf{R}_I\}) + E^e_{\mathbf{R}}\right]\psi^N = E\psi^N, \tag{2.11}$$

and the problem becomes fully separable as $\hat{H}\psi^N\psi^e_{\mathbf{R}} = E\psi^N\psi^e_{\mathbf{R}}$ and so the product wavefunctions are eigenfunctions of the full Hamiltonian.

In practice, the atoms are treated in a semi-classical way and we assume that their wavefunctions are delta functions in real space. The electronic Schrödinger equation, 2.7, is solved for fixed nuclear positions and then optionally, the nuclear system can be solved using these electronic wavefunctions.

The full Schrödinger equation has been simplified to one dealing with only the electrons in a fixed nuclear potential interacting with one another, but for any system larger than a few electrons the dimensionality of the equation is still much too big to be solved using current computing resources[6]. The main difficulty with solving this equation is the electron-electron interaction term. As this term involves interactions between every pair of electrons, it couples the electrons together leading to correlation between electronic states. If this term were neglected, equation 2.7 could be reduced

from 1 N-body equation to N 1-body equations and would be much easier to solve. Unfortunately neglecting this interaction is far from reality and so the approximation is not accurate for systems more advanced than the nearly-free electron model. Instead we will use density functional theory to help separate these terms into something more manageable.

2.2.3 Density Functional Theory

The Hohenberg Kohn Theorems[7] state that,

1. The ground state energy of a system of electrons is a unique functional of the ground state electronic density.

2. The true ground state density of the system is the density which minimizes the variational energy of the system.

The first of these allows one to write each of the terms that make up the Hamiltonian as a functional of the density of the system. The second allows us to find the minimum energy by varying the ground state density, and the density which gives this minimum must be the true ground state density.

Although these theorems tell us that it is possible to calculate the ground state density and energy, it does not explicitly tell us how to go about this. A major advance was in the formulation of the Kohn-Sham equations[8], where the electrons are non-interacting in a fictitious potential which gives the same ground state density as the real system. The system interacts only through the total density, but as this is bijective with the ground state energy, it should contain the full information about the system. This allows a simplification of the problem into coupled single particle equations

interacting only through the electronic density,

$$E_i\psi_i(\mathbf{r}) = \left(-\frac{1}{2}\nabla^2 + V_H[n(\mathbf{r})] + V_{XC}[n(\mathbf{r})] + V_{ext}(\mathbf{r})\right)\psi_i(\mathbf{r}), \qquad (2.12)$$

where E_i and $\psi_i(\mathbf{r})$ are the energy and wavefunction of electron i and $n(\mathbf{r})$ is the electronic density at point $\mathbf{r}$ and given by,

$$n(\mathbf{r}) = 2\sum_{i\ occ}\psi_i^*(\mathbf{r})\psi_i(\mathbf{r}), \qquad (2.13)$$

where the index i runs only over occupied bands and the factor 2 comes from spin degeneracy. Here we assume (and will throughout) that there is no magnetism present.

Equation 2.12 has several immediately recognizable terms. The first term with ∇ is the kinetic energy of the Kohn-Sham electrons. The second term, V_H, is the potential of a continuous distribution of charge, also known as the Hartree potential. The third term, V_{XC}, is known as the exchange and correlation potential(XC) which is discussed in the next section. The very last term, V_{ext}, is the external potential due to the fixed nuclei which is constant.

This separation is only made possible as the ground state density has a one to one correspondence with the external potential and the total energy. All the interaction between the individual electrons occurs in this formulation through the density in the middle terms of equation 2.12. Both of the Hartree and XC terms are functionals of the density and in the case of the Hartree energy, the form of the functional is known,

$$V_H[n(\mathbf{r})] = \int \frac{n(\mathbf{r}')}{|\mathbf{r}-\mathbf{r}'|}d\mathbf{r}'. \qquad (2.14)$$

This term represents the interaction of a distribution of charge within the system, but ignores the discrete nature of electrons in that they will not interact with themselves. Immediately this tells us that the XC functional should remove this self-interaction error. For the exchange-correlation potential there is no clear form like this, but in general it is dominated by the other terms in the equation. For an exact form of the XC functional, the ground state energy and density would be exact but in practice this is impossible to achieve.

2.2.4 Exchange and Correlation

The final term in equation 2.12 is V_{XC}, the exchange and correlation potential. This term effectively contains all the differences between the adiabatic time-independent Schrödinger equation, and the Kohn-Sham equations. It is made of two parts, the exchange (X) and correlation (C) potentials. It is defined as,

$$V_{XC} = \frac{\partial E_{XC}}{\partial n(\mathbf{r})}, \tag{2.15}$$

where E_{XC} is the total exchange and correlation energy and $n(\mathbf{r})$ is the density at a point $\mathbf{r}$.

Electron exchange is a quantum mechanical effect caused by the discrete nature of the electronic charge. Firstly, every electron will contribute to the charge density and, if just the bare Hartree energy were used, would have some interaction energy with itself that is not physical. Secondly as the electron is a fermion, the all-electron wavefunction must be antisymmetric with respect to swapping the indices of the electrons. In the single particle view, this enforces the Pauli exclusion principle and causes a spatial repulsion between wavefunctions.

The correlation energy is the energy difference between the non(directly)

interacting system and the true interacting system. In the true case, the electrons will have correlated positions and are highly unlikely to be found very close together. Extra degrees of freedom are added to the electronic wavefunction and the total energy must be lowered. The inclusion of this term in the single particle KS equation acts to include the effects of these electronic correlations within the system.

The exchange energy only affects electrons of the same spin as spatial asymmetry is only required among these. The correlation energy occurs between all electrons and is a many body effect but is only about 10% of the magnitude of the exchange energy[9] for the vast majority of materials, but there are some exotic strongly correlated materials, which have strong correlation between electronic states. Although it is possible to exactly calculate the exchange potential, it is computationally expensive as this involves performing products between every pair of wavefunctions and so will scale poorly with system size. Calculating the correlation exactly would require as much effort as solving the many body Schrödinger equation and so it must be approximated to achieve any gain from using DFT. Usually both are approximated to make calculations with many electrons feasible.

2.2.5 Exchange and Correlation(XC) Functionals

The simplest (non-trivial) approximation for the exchange and correlation is called the local density approximation (LDA). This states that the exchange and correlation energy for an electron at a point $\mathbf{r}$ where the density is $n(\mathbf{r})$ is the same as that in a homogeneous electron gas (HEG) with the same density. This leads to a functional of the following form,

$$E_{XC}^{LDA}[n(\mathbf{r})] = \int n(\mathbf{r})\epsilon_{XC}^{HEG}(n(\mathbf{r}))d\mathbf{r}, \tag{2.16}$$

where $\epsilon_{XC}^{HEG}(n(\mathbf{r}))$ is the exchange and correlation energy density for a HEG with density $n(\mathbf{r})$. The approximation relies on a very slowly varying density to be valid, and predicts that interactions are isotropic. Despite these issues, LDA is found to give good results in many materials[10] as the energy relies on the spherical average[9]. It is local as it only takes into account the density at the point $\mathbf{r}$.

Another local approximation is to take into account some information about the gradient of the density at $\mathbf{r}$ and this is called the generalised gradient approximation(GGA)[11], which is a type of semi-local functional. One issue is that, unlike the LDA case, there is some choice in which form the gradient should enter the form of ϵ_{XC}^{HEG}, and there are many different functionals available[12][13]. In general,

$$E_{XC}^{GGA}[n(\mathbf{r})] = \int n(\mathbf{r})\epsilon_{XC}^{GGA}(n(\mathbf{r}), \nabla n(\mathbf{r}))d\mathbf{r}. \tag{2.17}$$

The form that will be used in this study is that developed by Perdew, Burke and Ernzerhof (PBE)[14]. This functional retains the better features from more complicated GGA methods to reproduce the most important physical results while being relatively simple to implement. Unlike some functions which rely on tuning parameters, it relies only on fundamental limits that the correct XC functional should have.

2.2.6 Periodic Boundary Conditions

At this point, we have the basic tools required to solve the Schrödinger equation for a simple system containing a few tens of electrons, but in trying to study the properties of bulk materials, we still run into some problems. The number of electrons and atoms in any macroscopic amount of material is

huge. Taking the Kohn-Sham equations as they are, and trying to directly solve for the wavefunctions would be an enormous task and require impossibly large amounts of memory and computational time.

Many of the materials of interest in solid state physics have translational symmetry. Those that do in 3 linearly independent directions can be described by a repeating unit cell of atoms. Taken to infinity, this repeating unit cell is a good approximation of the bulk regions in crystals where the atoms and electrons are screened from surface effects.

Since we are generally more interested in bulk effects, the approximation can be made that the crystal is infinitely repeating in these 3 linearly independent directions. Bloch's theorem then allows a vast reduction in the number of electronic states, and the real-space domain that we must calculate them over.

2.2.7 Bloch's Theorem and Plane Wave Basis Sets

In trying to study the properties of bulk materials, we still run into some problems. The number of electrons in the system will be huge and the domain of the wavefunctions will also have to be very big in comparison to atomic scales. As we are interested in crystals, we can take advantage of the periodic nature of the unit cell. and write the wavefunction as a set of Bloch waves,

$$\psi(\mathbf{r})_{j,\mathbf{k}} = e^{-i\mathbf{k}.\mathbf{r}}\phi_{j,\mathbf{k}}(\mathbf{r}), \tag{2.18}$$

where $\mathbf{k}$ is a wavevector within the first brillouin zone and j is a band index. The allowed values of $\mathbf{k}$ are defined by the boundary conditions of the crystal. ϕ is a function which is periodic over the unit cell.

This converts the problem from being the calculation of the wavefunction over all space to calculating a periodic function over the unit cell. The most

natural basis set to expand a periodic function is the plane waves and so we use this to expand the wavefunction as,

$$\phi_{j,\mathbf{k}}(r) = \sum_{\mathbf{G}} C_{j,\mathbf{k},\mathbf{G}} e^{-i\mathbf{G}.\mathbf{r}}, \tag{2.19}$$

where $\mathbf{G}$ is a wavevector within the first brillouin zone and $C_{j,\mathbf{k},\mathbf{G}}$ are the plane wave coefficients. The full wavefunction is then given by,

$$\psi(\mathbf{r})_{j,\mathbf{k}} = \sum_{\mathbf{G}} C_{j,\mathbf{k},\mathbf{G}} e^{-i(\mathbf{k}+\mathbf{G}).\mathbf{r}}. \tag{2.20}$$

The problems are thus alleviated by this transformation to reciprocal space and sampling over a limited range of $\mathbf{k}$. Due to the periodicity of reciprocal space, the calculation of $\psi_{\mathbf{k}}$ can be restricted to within the first Brillouin zone as the solutions outside of this are degenerate with those inside.

Alternative basis sets can be used, for example linear combinations of atomic orbitals or Gaussian functions. The advantage with these is that the required size of the basis set is much smaller, and the Hamiltonian easier to construct and diagonalise. The main disadvantage is that they are not particularly well suited to describing electrons in metallic systems, add additional terms to operators, and are more computationally intensive to transform between phase space and real space.

2.2.8 Pseudopotentials

Most of the physical properties of atoms in crystals are due to the electrons which are far from the nucleus. The core electrons are shielded from the environment by the outer or valence electrons and conversely, the valence electrons are shielded from the nucleus by the core electrons. In general,

changes to the wavefunctions of the core electrons are small compared with changes to the valence electrons which are involved with bonding. The computational effort involved scales as N_e^3 as the wavefunctions must be orthonormal in the Kohn-Sham scheme. This restricts the size of the systems that can be studied. Additionally, as the outer electrons must be orthogonal to core electrons, very large basis sets are needed to allow high frequency oscillations near the nucleus.

As the core electrons are relatively insensitive to the chemical environment, it is preferable to combine the potential of these electrons with the nuclear potential to create a pseudopotential for an ion. These are created such that the wavefunctions of valence electrons are identical to the all electron results outside of a certain radius r_c and that they have no nodes within this radius.

This decreases the computational complexity for several reasons:

- Reducing the short wavelength oscillations close to the nucleus, leading to a much lower basis set size.
- Decreasing the number of electronic states that must be calculated.
- Certain atoms have non-negligible relativistic effects for core electrons and these can be included in the pseudopotential.

Figure 2.1 shows an example of the all-electron and pseudo wavefunctions for Sn. The wavefunctions are identical above the cutoff radius, but the pseudo wavefunctions are much smoother inside the core region.

For plane wave methods, pseudopotentials are generally employed because of these reasons. Another optional requirement for pseudopotentials is that the normalisation of the wavefunctions should be preserved. The integral of the square amplitude of the valence pseudo-wavefunctions should

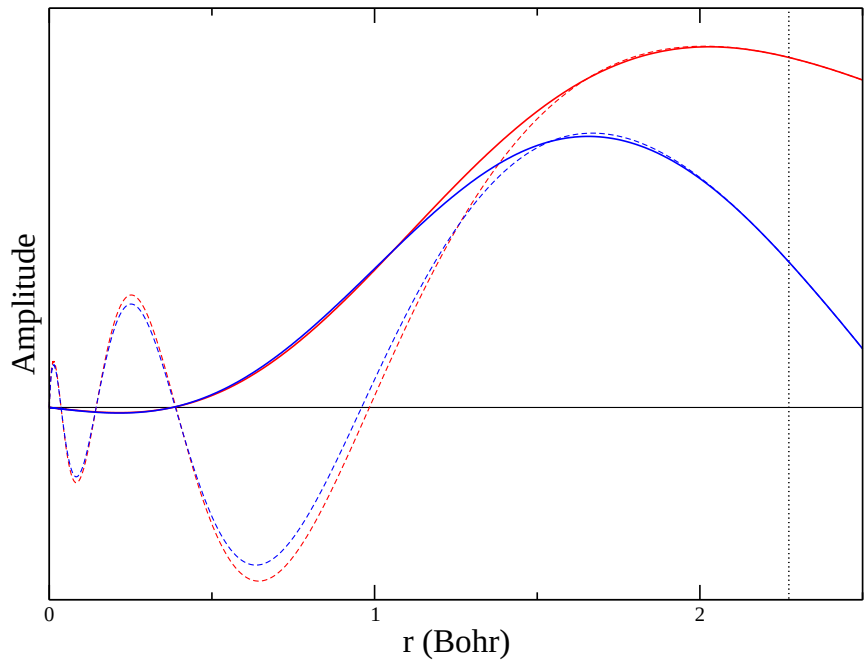

Figure 2.1: The all electron(dashed) and pseudo-partial(solid) wavefunctions from a pseudopotential for Sn. Only the 5s(red) and 5p(blue) electrons are considered as valence. The cutoff radius is shown as a dashed line at 2.28 Bohr.

be equal to that of the all-electron wavefunctions. These normalisation preserving pseudopotentials help to ensure the scattering properties of the ion are reproduced correctly. These pseudopotentials have the general form

$$V_{ps} = V_{ps}^{loc} + \sum_{i,j} D_{i,j} \left|P_i\right\rangle \left\langle P_j\right|, \tag{2.21}$$

where $D_{i,j}$ is a matrix unique to each pseudopotential and is parametrized by reference to the all electron result and P_i is a projector onto an angular momentum state, i. The all-electron KS equations are replaced by

$$\left(T + V_{ps} + V_H^v + V_{XC}\right) \left|\psi_i^{ps}\right\rangle = \epsilon_i^{ps} \left|\psi_i^{ps}\right\rangle, \tag{2.22}$$

where V_H^v is the hartree potential from only the valence electrons and i runs only over the valence states. The requirements for pseudopotentials are that $\epsilon_i^{ps} = \epsilon_i^{KS}$ and that $|\psi_i^{ps}(r)\rangle = |\psi_i^{KS}(r)\rangle$ when $r > r_c$.

The norm-conservation requirement can be relaxed by allowing the norm of the pseudo-wavefunctions to differ from the all electron result within r_c at the expense of additional computational effort in calculating the KS equations but allows further reduction in basis set size. In general the reduction in basis set size outweighs the computational effort to calculate the additional terms required but this is not the case for perturbative calculations and will not be used in this study.

2.3 Dynamics of Nuclear Motion

2.3.1 Introduction

Ground state properties can give us basic information about condensed matter systems. These include properties like lattice constants, band gaps and total energies. For the majority of physical systems, it is the dynamics of interactions that are of interest. We want to study what happens when a perturbation is introduced into the system and how the ground state picture is affected.

2.3.2 Lattice Dynamics

Dynamical processes in materials can be extraordinarily complicated and generally infeasible to calculate directly. Electronic interactions happen very rapidly in comparison with nuclear interactions due to the same arguments as with the Born Oppenheimer approximation. For a direct time dependent simulation of a single phonon mode, many instantaneous timesteps would

have to be calculated to conserve the energy of the system. This would have to be repeated for many possible phonon configurations to build up a sample of atomic vibrations in the material.

A major simplification is to assume that we can work in the harmonic approximation. This allows the separation of phonons into well defined modes that add linearly. The potential wells that the atoms feel are only dependent on the position up to the 2nd order derivative.

If we separate the position of an atom as

$$\mathbf{R}_{l,s} = \mathbf{R}_l + \boldsymbol{\tau}_s + \boldsymbol{\mu}_{l,s}, \tag{2.23}$$

where $l = (l_a, l_b, l_c)$ is the index of the unit cell in which the atom is, s is the index of the atom within a single unit cell, $\mathbf{R}_l$ is the position of the origin of cell l, $\boldsymbol{\tau}_s$ denotes the equilibrium position of atom s within a single unit cell and $\boldsymbol{\mu}_{l,s}$ is the deviation from the equilibrium position of atom s in cell l.

For a total energy E given at the equilibrium position as E_0, we can expand in a Taylor series in $\boldsymbol{\mu}_{l,s}$,

$$E = E_0 + \sum_{l,s} \frac{\partial E}{\partial \boldsymbol{\mu}_{l,s}} \boldsymbol{\mu}_{l,s} + \frac{1}{2} \sum_{l,s,m,t} \frac{\partial^2 E}{\partial \boldsymbol{\mu}_{l,s} \partial \boldsymbol{\mu}_{m,t}} \boldsymbol{\mu}_{l,s} \boldsymbol{\mu}_{m,t} + \dots, \tag{2.24}$$

where the derivatives are given at the equilibrium positions of the atoms. Since the equilibrium point is defined where the forces on any atom are 0, the first order derivatives must also be 0, therefore

$$E \approx E_0 + \frac{1}{2} \sum_{l,s,m,t} \frac{\partial^2 E}{\partial \boldsymbol{\mu}_{l,s} \partial \boldsymbol{\mu}_{m,t}} \boldsymbol{\mu}_{l,s} \boldsymbol{\mu}_{m,t}. \tag{2.25}$$

These second derivatives of the energy are called the interatomic force

constants(IFCs) by analogy to the spring constant of a simple harmonic oscillator. They are defined as

$$C_{l,m,s,t} = \frac{\partial^2 E}{\partial \boldsymbol{\mu}_{l,s} \partial \boldsymbol{\mu}_{m,t}}. \tag{2.26}$$

2.3.3 Boundary Conditions

We are still left with the problem that these IFCs must be calculated between pairs of atoms across the entire crystal. By applying Born-von Karman boundary conditions to the problem, we can then make it tractable. If we assume our crystal is very large, it becomes very likely that the phonon displacements repeat across some integer number, $T = (T_a, T_b, T_c)$, unit cells. Applying Bloch's theorem, we find that the allowed phonon modes are of the form

$$\boldsymbol{\mu}_{l-m,s} = e^{i\mathbf{q}.\mathbf{R}_m} \boldsymbol{\mu}_{l,s}, \tag{2.27}$$

where l, m are unit cell indexes, s the atom index in the unit cell and $\mathbf{R}_m$ is a vector to the origin of cell m. The allowed values of the phonon wavevector q are given by

$$\mathbf{q} = (\frac{2\pi}{T_a}, \frac{2\pi}{T_b}, \frac{2\pi}{T_c}) = (\frac{2\pi n_a}{L_a}, \frac{2\pi n_b}{L_b}, \frac{2\pi n_c}{L_c}), \tag{2.28}$$

where n_a, n_b, n_c are integers, and as $L \to \infty$, q becomes a continuum as in the electronic case. The wavelength of a phonon is given by $\lambda = \frac{2\pi}{|q|}$. Thus we only need to calculate the eigenvectors for phonons within the first Brillouin zone, and the others are related to these by equation 2.27.

Now as the IFCs can only depend on relative positions of unit cells rather than absolute positions, the IFCs cannot directly depend on l and m but only upon the differences. We write a new form for the IFCs and then take

the Fourier transform,

$$C_{s,t}(l-m) = C_{l,m,s,t}, \tag{2.29}$$

$$D_{s,t}(\mathbf{q}) = \frac{1}{N}\sum_{l,m} C_{s,t}(l-m)e^{i\mathbf{q}.(\mathbf{R}_l-\mathbf{R}_m)}, \tag{2.30}$$

$$= \sum_{l} C_{s,t}(l)e^{i\mathbf{q}.\mathbf{R}_l}, \tag{2.31}$$

where N is the number of atoms and the second line comes from translational invariance or alternatively by the substitution $\mathbf{l'} = \mathbf{l} - \mathbf{m}$. $D_{s,t}(\mathbf{q})$ is known as the dynamical matrix and governs the atomic interactions for a specific phonon wavevector.

2.3.4 Solving the Dynamical Matrix

With knowledge of the dynamical matrix, we can search for harmonic solutions. We first write the equation of motion which follows from equation 2.25:

$$M_s\ddot{\boldsymbol{\mu}}_{l,s} = \sum_{l,s,m,t} C_{s,t}(l-m)\boldsymbol{\mu}_{m,t}, \tag{2.32}$$

where M_s is the mass of atom s. We write an ansatz for the form of the solution,

$$\boldsymbol{\mu}_{l,s} = \frac{1}{2\sqrt{M_s}} e_s(\mathbf{q})e^{i(\mathbf{q}.\mathbf{r}-\omega(\mathbf{q})t)}, \tag{2.33}$$

where $e_s(\mathbf{q})$ are the phonon eigenvectors (or modes) and $\omega(\mathbf{q})$ are the frequencies. Substituting this into equation 2.32, the equations reduce to

$$\omega^2(\mathbf{q})e_s(\mathbf{q}) = \sum_t \frac{D_{s,t}(\mathbf{q})}{\sqrt{M_s M_t}} e_t(\mathbf{q}). \tag{2.34}$$

This equation can be solved directly for the phonon eigenvector, $e_s(\mathbf{q})$, and squared frequency, $\omega^2(\mathbf{q})$. It is usually solved by standard generalised eigen-

value methods as the number of atoms tend to be much fewer than the number of plane wave basis states.

2.3.5 Derivatives of the Total Energy

Many physical properties depend on the response of a system to some external stimuli. For example, polarization is the response to an external electric field. Lattice dynamics is the response of the system due to ionic displacement from the equilibrium value. The forces on an atom are given by the Hellman-Feynman theorem[15],

$$\frac{\partial E}{\partial \lambda_i} = \langle \psi | \frac{\partial H}{\partial \lambda_i} | \psi \rangle = \int \frac{\partial V}{\partial \lambda_i} n(\mathbf{r}) dr. \tag{2.35}$$

Only the ground state density is required to calculate the first order response of the total energy to external perturbations. Unfortunately for second order energy derivatives, the first order response of the charge density is required:

$$\frac{\partial^2 E}{\partial \lambda_i \partial \lambda_j} = \int \frac{\partial^2 V}{\partial \lambda_i \lambda_j} n(\mathbf{r}) dr + \int \frac{\partial V}{\partial \lambda_i} \frac{\partial n(\mathbf{r})}{\partial \lambda_j} dr. \tag{2.36}$$

These are the first two terms of the $2n + 1$ theorem which states that the response of the total energy can be calculated up to order $2n + 1$ with knowledge of only up to the n^{th} derivative of the electronic wavefunctions. To calculate the IFCs, we will need to calculate the first order response to an external perturbation, in this case a phonon of wavevector $\mathbf{q}$.

2.3.6 Perturbation Theory

As we are already able to calculate the ground state of the system, the obvious place to start to attempt to calculate the 2nd order energy change is by using perturbation theory. Firstly, we expand the external potential

in terms that are constant, linear, quadratic and of higher orders in some external parameter λ:

$$v_{ext}(\lambda) = v_{ext}^{(0)} + \lambda v_{ext}^{(1)} + \lambda^2 v_{ext}^{(2)} + \dots \,. \tag{2.37}$$

We can expand any physical quantity, X, in terms of how they respond to a change with respect to this variable, λ

$$X(\lambda) = X^{(0)} + \lambda X^{(1)} + \lambda^2 X^{(2)} + \dots \,, \tag{2.38}$$

where X is the physical quantity in question and λ is a small value so that these results converge.

The values of the $X^{(n)}$ are given by Taylor's theorem:

$$X^{(n)} = \frac{1}{n!} \frac{\partial^n X}{\partial \lambda^n}\bigg|_{\lambda=0}. \tag{2.39}$$

If we now write out the Schrödinger equation in these new forms, and separate into powers of λ, we find that

$$H_{KS}^{(0)} \left|\psi_n^{(0)}\right\rangle = \epsilon_n^{(0)} \left|\psi_n^{(0)}\right\rangle, \tag{2.40}$$

and

$$H_{KS}^{(1)} \left|\psi_n^{(0)}\right\rangle + H_{KS}^{(0)} \left|\psi_n^{(1)}\right\rangle = \epsilon_n^{(1)} \left|\psi_n^{(0)}\right\rangle + \epsilon_n^{(0)} \left|\psi_n^{(1)}\right\rangle. \tag{2.41}$$

Equation 2.40 is just the ground state HKS equation. Equation 2.41 can be rearranged to give us the Sternheimer equation,

$$(H_{KS}^{(0)} - \epsilon_n^{(0)}) \left|\psi_n^{(1)}\right\rangle = -(H^{(1)} - \epsilon_n^{(1)}) \left|\psi^{(0)}\right\rangle. \tag{2.42}$$

From standard first order perturbation theory, the correction to the 1st

order wavefunctions can be given by a sum over states:

$$\left|\psi_n^{(1)}\right\rangle = \sum_{n\neq m} \left|\psi_m^{(0)}\right\rangle \frac{\left\langle\psi_m^{(0)}\right| H^{(1)} \left|\psi_n^{(0)}\right\rangle}{\epsilon_n - \epsilon_m}. \tag{2.43}$$

Expanding equation 2.13 for the density, we find,

$$\begin{aligned} n^{(1)}(\mathbf{r}) &= 2\sum_{n\ occ} \psi_n^{(1)*}(\mathbf{r})\psi_n^{(0)}(\mathbf{r}) + \psi_n^{(0)*}(\mathbf{r})\psi_n^{(1)}(\mathbf{r}) \\ &= 4Re\sum_{n\ occ} \psi_n^{(0)*}(\mathbf{r})\psi_n^{(1)}(\mathbf{r}) \\ &= 4Re\sum_{n\ occ}\sum_{m\neq n} \psi_n^{(0)*}(\mathbf{r})\psi_m^{(0)} \frac{\left\langle\psi_m^{(0)}\right| H^{(1)} \left|\psi_n^{(0)}\right\rangle}{\epsilon_n - \epsilon_m}. \end{aligned}$$

We see that the contributions from pairs of occupied bands cancel and the first order densities are only affected by coupling to unoccupied bands. The value of the index m is thus restricted to the conduction bands. This allows a modification of equation 2.42 by projecting the first order wavefunctions onto the conduction manifold using the projection operator,

$$P_c = \sum_{c\ unocc} \left|\psi_c^{(0)}\right\rangle \left\langle\psi_c^{(0)}\right| = \mathbf{1} - \sum_{v\ occ} \left|\psi_v^{(0)}\right\rangle \left\langle\psi_v^{(0)}\right| \tag{2.44}$$

where $\mathbf{1}$ is the identity matrix. The second form of this equation is used in practice, so as to avoid a sum over unoccupied states which may not be converged. This is important as the occupied subspace is much smaller than the unoccupied subspace.

Equation 2.42 can be then made invertible by only considering changes in this region,

$$P_c(H^{(0)} - E_n^{(0)}) \left|\psi_n^{(1)}\right\rangle = -P_c H^{(1)} \left|\psi^{(0)}\right\rangle. \tag{2.45}$$

This formulation does not take into account the possible change in occupation levels at the Fermi energy due to infinitesimal perturbations (eg equation 2.13). This is acceptable in semiconductors and insulators as we would not expect to see any change as the energy gap is normally much larger than the phonon energy. A finite density of states at the Fermi energy is required for our current theories of superconductivity and so we must further look to extensions to allow for partial band occupations.

2.3.7 Metals

Ground State

A metal is defined by having a finite density of states at the Fermi energy. This is due to the highest occupied band only being partially filled, whether it be due to having an odd number of electrons in the unit cell or by the shape of the bands themselves. The Fermi surface is the collection of points in the Brillouin zone where a change between the number of bands being occupied and unoccupied occurs. Different bands may cross at different gradients and some may cross the Fermi energy for only a very small region of phase space. To accurately capture the physics around these points, a high sampling of the Brillouin zone is required.

Another problem presents itself due to the sharp cut-off defined by the Fermi-Dirac distribution at low temperature. There is a discontinuity in which electronic states contribute to the total density. This creates problems in attempting to solve the Schrödinger equation whereby minima-finding algorithms may be unstable around a solution by band occupation number changing due to very small changes in band energy levels. This effect is known as charge-sloshing.

One solution to this is to attempt to interpolate the electronic band

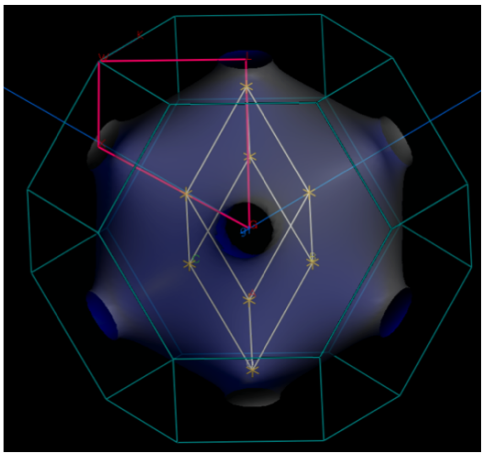

Figure 2.2: The Fermi surface for Au shown within the first Brillouin zone.

energies between sampling points. This procedure divides the Brillouin zone into symmetry breaking phase space elements and attempts to infer the band energies from the values at the vertexes.

Another solution is to smear the electron distribution by a finite amount. This allows bands above the Fermi energy to be sampled as part of the electronic minimization. A smearing function is defined as

$$\delta_\sigma(\epsilon) = \frac{1}{\sigma}\tilde{\delta}(\epsilon/\sigma), \tag{2.46}$$

where $\tilde{\delta}(x)$ is a function which integrates to 1 and is an approximation of the delta function. The energy of a band is modified to have a spectrum of values around the sampled value. The ground state density is modified to

$$n(\mathbf{r}) = 2\sum_i \tilde{\theta}\left(\frac{\epsilon_f - \epsilon_i}{\sigma}\right)\psi_i^*(\mathbf{r})\psi_i(\mathbf{r}), \tag{2.47}$$

where $\tilde{\theta}(x) = \int_{-\infty}^{x}\tilde{\delta}(x)dx$ is a smooth approximation to the heaviside step function. In the limit where σ is small, it is seen to reduce to equation 2.13. We can define occupation numbers $f_i = \tilde{\theta}\left(\frac{\epsilon_f-\epsilon_i}{\sigma}\right)$ which simplify the

notation.

The total number of states below the Fermi energy must be equal to the number of electrons so we have the constraint

$$N = \sum_i \int_{-\infty}^{\epsilon_f} \tilde{\delta}(\epsilon_i) d\epsilon = \sum_i \tilde{\theta}\left(\frac{\epsilon_f - \epsilon_i}{\sigma}\right), \tag{2.48}$$

which defines the Fermi energy in this case. The total energy is no longer variational and we must instead minimize the free energy:

$$F = E - \sigma \sum_i S\left(\frac{\epsilon_f - \epsilon_i}{\sigma}\right), \tag{2.49}$$

where σ may be seen as an effective temperature for the case of the Fermi-Dirac distribution. S is the entropy of the particular distribution. In practice, this entropic contribution is taken as part of the kinetic energy, T.

For this form to actually be useful, we must pick a function to use as the smearing function. Many reasonable choices exist, and the only constraint is that it must integrate to 1 and be smooth. Commonly used functions are the Gaussian error function, or the Fermi-Dirac distribution. There are issues in that the ground state that we end up in effectively has a fictitious electronic temperature. Furthermore, in some materials with low lying conduction bands, the total energy will be slightly modified from the 0 K result by the slight occupation of these levels and this will be discussed in a later chapter.

Perturbations

The modifications for metals in the ground state also modify the first order equations. In particular, the first order density is modified as

$$n^{(1)}(\mathbf{r}) = 2\sum_n f_n \left[\psi_n^{(0)*}(\mathbf{r})\psi_n^{(1)}(\mathbf{r}) + c.c.\right] + \delta_\sigma\left(\epsilon_f - \epsilon_i\right)\left(\epsilon_f^{(1)} - \epsilon_n^{(1)}\right)\psi_n^{(0)*}(\mathbf{r})\psi_n^{(0)}(\mathbf{r}). \tag{2.50}$$

The density is modified by an additional term which is due to the variation of occupation numbers and possibly in the Fermi energy. Changes in the Fermi energy can only be caused by phonons at the Γ point and for a general case can be ignored. We can rewrite the remaining expression as

$$n^{(1)}(\mathbf{r}) = \sum_{n,m} \psi_n^{(0)*}(\mathbf{r})\psi_m^{(0)}(\mathbf{r})\frac{f_n - f_m}{\epsilon_n - \epsilon_m}\left\langle \psi_m^{(0)}\right| H^{(1)} \left|\psi_n^{(0)}\right\rangle, \tag{2.51}$$

where the extra term in equation 2.50 is represented by the diagonal $n = m$ term in the equation. This equation is numerically stable for any finite smearing width. It has been shown by de Gironoli[16] that the Sternheimer equation is modified to be,

$$\left[H_{KS} + Q + \epsilon_n\right]\left|\psi_n^{(1)}\right\rangle = -\left[f_n - P_n\right] H^{(1)}\left|\psi_n^0\right\rangle, \tag{2.52}$$

with

$$Q = \sum_k \alpha_k \left|\psi_k\right\rangle\left\langle\psi_k\right| \qquad P_n = \sum_m \beta_{n,m}\left|\psi_m\right\rangle\left\langle\psi_m\right|, \tag{2.53}$$

and

$$\beta_{n,m} = f_n\tilde{\theta}\left(\frac{\epsilon_n - \epsilon_m}{\sigma}\right) + f_m\tilde{\theta}\left(\frac{\epsilon_m - \epsilon_n}{\sigma}\right) + \alpha_m\frac{f_n - f_m}{\epsilon_n - \epsilon_m}\tilde{\theta}\left(\frac{\epsilon_m - \epsilon_n}{\sigma}\right),$$

where α is chosen to make the system non-singular for all nonzero $\left|\psi_n^{(1)}\right\rangle$. This is achieved by setting $\alpha_k = max(\epsilon_f + \Delta - \epsilon_k, 0)$ with $\Delta = 3\sigma$. These restrictions makes Q and P require only sums over occupied and partially occupied states. This formalism allows the use of finite temperatures within the perturbative framework. The main advantage is that the sampling required in the Brillouin zone is not as high as the contributions of states just above and below the Fermi energy are slightly smeared giving an approximation to the true distribution of energy levels. It again has the disadvantage that it may not be a good approximation to the properties of the crystal at low temperatures.

2.3.8 Electron-Phonon Coupling

To calculate the transport properties of electrons from the wavefunctions, it is necessary to reintroduce the electron-phonon term in equation 2.10 that were neglected in the Born-Oppenheimer approximation. This term depends on the rate of change of the wavefunction of the electrons with respect to the change in nuclear positions. In neglecting these terms, we have ignored coupling between excited nuclear and electronic states.

Rather than try to apply the operator $\hat{H}^{ep}$ directly, it is more physically insightful to look at the first-order nuclear-electron potential in the system. The most basic form could be calculated by taking the direct change in the ionic potential (the 'naked' or 'bare' potential) due to the perturbation, but this is a very poor approximation. The electrons in the system move in response to this change in potential, effectively screening the 'bare' potential. Instead, the fully self consistent 'dressed' potential is used to allow the reaction of the electrons to be taken into account. The dressed deformation

potential is given by

$$\delta V_{\mathbf{q},j} = \sum_I \delta\tilde{e}_{\mathbf{q},j,I} . \frac{\partial V_{\mathbf{q}}^{SCF}}{\partial \boldsymbol{\mu}_I}, \tag{2.54}$$

where the sum is over atoms, $\tilde{e}_{\mathbf{q},j,I}$ is the mass reduced phonon eigenvector of atom I in the phonon $\mathbf{q}, j$ and $V_{\mathbf{q}}^{SCF}$ is the self consistent potential derived from perturbative calculations.

The electron-phonon matrix element, $g^{\mathbf{q},j}_{\mathbf{k},i,\mathbf{k}',i'}$ represents the scattering of an electron $\left|\mathbf{k}', i'\right\rangle$ from/to a state $|\mathbf{k}, i\rangle$ by adsorbing/emitting a phonon of wavevector $\mathbf{q}, j$. These matrix elements can be calculated between arbitrary states of $\mathbf{k}$,i,$\mathbf{k}'$,i' and $\mathbf{q}$ but only those on the Fermi surface have any physical relevance for electron transport. The matrix elements are given by

$$g^{\mathbf{g},j}_{\mathbf{k},i,\mathbf{k}',i'} = \sqrt{\frac{\hbar}{2\omega_{\mathbf{q},j}}} \left\langle \mathbf{k}', i' \right| \delta V_{\mathbf{q},j} \left| \mathbf{k}, i \right\rangle, \tag{2.55}$$

where $\delta V_{\mathbf{q}}^{SCF}$ is the derivative of the self consistent potential in the Kohn-Sham equations with respect to the atomic positions and $\omega_{\mathbf{q},j}$ are the phonon eigenfrequencies.

These matrix elements are closely related to the Eliashberg Spectral Function[17], $\alpha^2 F(\omega)$, which describes the scattering of electrons between states due to the interaction of all the electronic states with phonons of frequency ω. As the phonon energy scales are of the order of meV which is much less than the electronic energy scale, we make the approximation that only electrons on the Fermi surface can be scattered and that they scatter into states on the Fermi surface. Also for conservation of crystal momentum, the values of $\mathbf{k}'$ are restricted such that $\mathbf{k}' = \mathbf{k} + \mathbf{q}$. The spectral function

becomes

$$\alpha^2F(\omega) = \frac{1}{N_f}\sum_{\mathbf{q},j}\sum_{\mathbf{k},i,i'}|g^{\mathbf{q},j}_{\mathbf{k},i,\mathbf{k}+\mathbf{q},i'}|^2\delta(\epsilon_f - \epsilon_{\mathbf{k},i})\delta(\epsilon_f - \epsilon_{\mathbf{k}+\mathbf{q},i'})\delta(\hbar\omega - \hbar\omega_{\mathbf{q},j}), \tag{2.56}$$

which is a sum over every possible initial and final state but which is restricted by the delta functions involving the Fermi energy, ϵ_f to those states which lie on the the Fermi surface. The electron-phonon matrix elements determine the probability of the scattering occurring. Together these combine to determine the overall strength of scattering for a particular phonon frequency. This form is strictly valid only at 0 K but can be used as an approximation for low temperatures. The equation shows the conservation of crystal momentum as a phonon of wavevector $\mathbf{q}$ can only scatter electrons between states $\mathbf{k}$ and $\mathbf{k}+\mathbf{q}$.

The Eliashberg spectral function is linked to an important parameter for superconducting materials – λ, the electron-phonon coupling constant which gives a dimensionless indicator of the strength of the electron-phonon interaction in the material[17]:

$$\lambda = 2\int\frac{\alpha^2F(\omega)}{\omega}d\omega. \tag{2.57}$$

This quantity can be inferred experimentally and is relevant for those in the experimental superconductivity community as it measures the strength of the electron-phonon coupling and the attractive energy between electrons in the superconducting state.

With these theoretical methods, we will try to build a practical method of calculating the electron-phonon coupling constant in the follow chapters.

Chapter 3

Ground State Calculations in Practice

3.1 Introduction

Although we have set out theoretically how the electron-phonon coupling quantities would be calculated, there are many practical issues to be considered. For example, we do not want to directly minimize all the Kohn-Sham states as we are generally only interested in the occupied bands and need to choose a minimisation method that suits this. We will go into detail on these choices and how they affect ground state calculations in this chapter.

3.2 Ground State

The first quantity required to calculate any physical property using DFT is the ground state total energy and density. This must be calculated efficiently and within a limited amount of memory and with a reasonable amount of CPU time.

3.2.1 Total Energy and Density

Quantities such as the total energy must be self consistent for the DFT arguments to be valid. That is the process used to generate a quantity must also give that quantity when they are used as the input. The primary example is the density which is generated from the occupied Kohn-Sham orbitals, which in turn depend on the Kohn-Sham potential which is generated from the density. Only in the case where self consistency is achieved, will the total energy and other related quantities be the ground state quantities. As the relationship between ground state density and ground state energy is bijective, this is equivalent to getting self consistency in the total energy at a minimum of the energy landscape.

We start with a trial set of wavefunctions, $\psi_{i,k}$ which generate a trial density $n(\mathbf{r})$. This is used to calculate the Kohn-Sham potential v_{KS} and the starting energy E. The total energy is then minimized with respect to the wavefunctions under the KS potential to give a new set of wavefunctions $\psi_{i,k}$ which in turn give a new ground state density, $n(r)$, and total energy E. This total energy is compared with the total energy from previous iterations. If it is within an an arbitrary tolerance, it is considered to be converged as the energy has not varied by more than the tolerance between cycles and so must be near the minimum. This process is shown in figure 3.1

3.3 Basis Sets

The electronic states are given as an Fourier expansion and due to memory constraints and computational effort, this series must be truncated at some point, N_g

$$\psi_{j,\mathbf{k}}(r) = \sum_{G=0}^{N_k} c_{j,k,G} e^{i(k+G).r}. \tag{3.1}$$

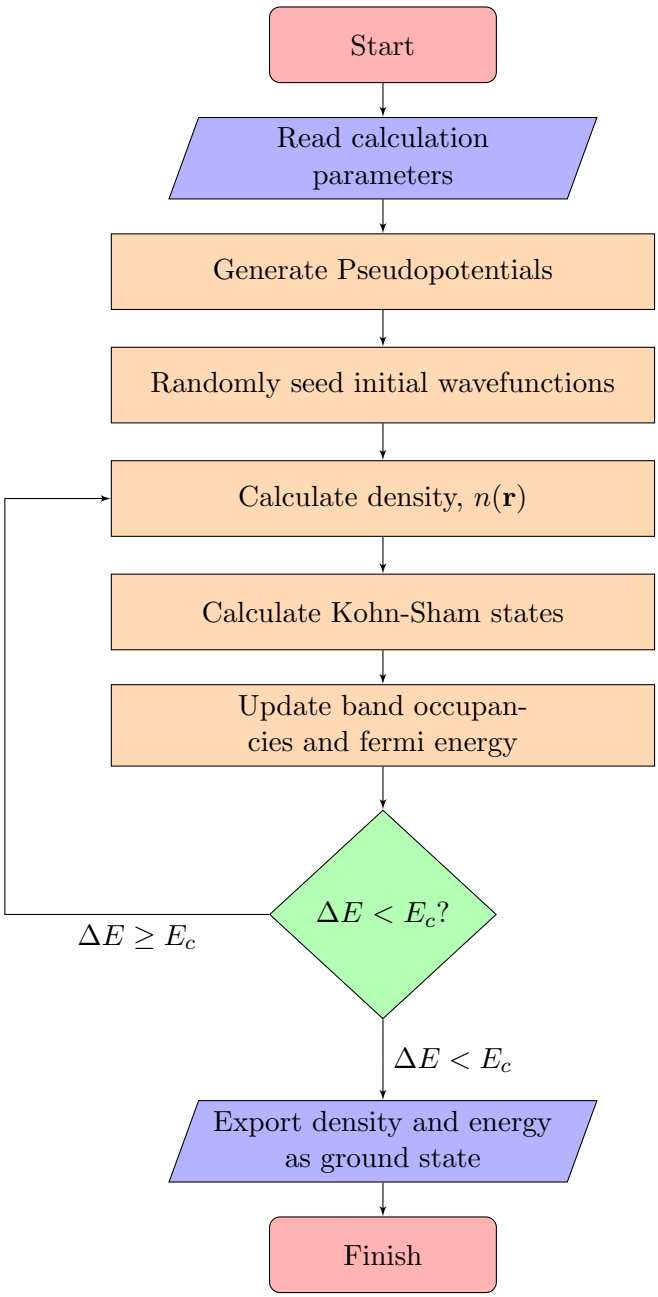

Figure 3.1: A flowchart showing the process used to calculate the ground state density and total energy.

It is most efficient to rewrite the Hamiltonian operator into a mixture of operators on the normal space and Fourier space coefficients. In particular, the kinetic energy has a very simple diagonal form in Fourier space,

$$T[\psi_{i,\mathbf{k}}(r)] = \sum_{\mathbf{G}=\mathbf{0}}^{N_k} c_{i,\mathbf{k},\mathbf{G}} \frac{|\mathbf{k}+\mathbf{G}|^2}{2}. \tag{3.2}$$

Restricting ourselves to basis states below a certain kinetic energy gives a natural way to definite the limit of the Fourier series, $|\mathbf{k}+\mathbf{G}_{max}|^2 \leq E_{cut}$.

The local potentials, such as the XC potential, are diagonal in real space, as they only depend on $\mathbf{r}$. The operators are applied by transforming the density into real-space, applying the operator directly and transforming back to reciprocal space. This is made efficient by the use of fast fourier transforms (FFTs) as the size of the basis set is chosen to be a multiple of small prime numbers. These operations are performed to avoid operators that are non-local and would be expensive to calculate.

3.3.1 Wavefunctions

The KS wavefunctions are solutions of the one particle KS equations given by equation 2.12. This equation when written in matrix form is simply an eigenvector problem and can be solved by matrix diagonalisation with the caveat that there is the possibility of degenerate eigenvalues(energies). Direct matrix diagonalisation is proportional to n_{pw}^3, with n_{pw} being the number of basis set elements. For codes where the basis set is small, such as Gaussian basis sets, this is not the bottleneck in the calculation. On the other hand when using plane wave basis sets, n_{pw} may be $\sim 100,000$ and this diagonalisation becomes much more expensive.

As the Hamiltonian matrix is of size n_{pw}^2, direct diagonalisation give n_{pw}

wavefunctions which is orders of magnitude more than the number of occupied states. An alternative to the direct diagonalisation is to use an iterative minimization technique. This allows an arbitrary number of lowest-energy wavefunctions to be found by directly minimizing their energy through the Kohn-Sham Hamiltonian.

For insulators, the number of bands can be restricted to the number of electrons in the spin polarized system, or the number of electron pairs in an unpolarised system. For metallic systems, the value of n must be larger so as to encompass bands which are only partially occupied across the Brillouin zone.

3.3.2 Real Space Grids

A finite Fourier series must be used as we do not have infinite memory to hold our wavefunctions. The Nyquist-Shannon sampling theorem[18] states such a series can be represented exactly by a discrete set of points in real space which can fully represent all the information stored in the Fourier series. If the Fourier space is a grid of N_x, N_y, N_z components, the size of the real space grid is $N_x \times N_y \times N_z$. Conversion is performed by Fourier expansion using fast Fourier transforms (FFT) which work by a divide and conquer algorithm and reduce the computational complexity.

The use of FFTs requires that the number of coefficients be a multiple of small prime numbers. For the case of powers of 2, the Cooley-Tukey FFT algorithm divides the Fourier transformation into two smaller Fourier

transforms,

$$\begin{aligned} X_k &= \sum_{n=0}^{N-1} x_n e^{-\frac{2\pi i}{N} nk} \\ &= \sum_{n=0}^{N/2-1} x_{2m} e^{-\frac{2\pi i}{N}(2m)k} + \sum_{n=0}^{N/2-1} x_{2m+1} e^{-\frac{2\pi i}{N}(2m+1)k} \\ &= \sum_{n=0}^{N/2-1} x_{2m} e^{-\frac{2\pi i}{N}(2m)k} + e^{-\frac{2\pi i}{N}k} \sum_{n=0}^{N/2-1} x_{2m+1} e^{-\frac{2\pi i}{N}(2m)k} \\ &= E_k + e^{-\frac{2\pi i}{N}k} O_k. \end{aligned} \tag{3.3}$$

The two smaller Fourier transforms operate on the even, E_k, and odd, O_k elements of the original FFT. There is a futher identity, due to the periodicity of these size-$N/2$ Fourier transforms,

$$X_{k+N/2} = E_k - e^{-\frac{2\pi i}{N}k} O_k. \tag{3.4}$$

Thus by doing the two smaller Fourier transforms, we actually get two elements of the full Fourier transform. This process is recursively applied to these smaller Fourier transforms to reduce them to trivial Fourier transformations of size 1. These smaller Fourier transforms can also be performed in parallel. The increase in efficiency comes from caching the intermediate results of the smaller Fourier transformations. This process has been generalized for other prime numbers and is most efficient when the number of elements to be Fourier transformed has only small prime factors.

For terms which are products of wavefunctions, for example the density, higher order Fourier components are produced up to twice those in the wavefunctions, as a result of the convolution theorem. This requires both a larger basis set to represent and a finer grid in real space. Furthermore, for derivatives of quantities on the grid, even higher order terms can be

produced and require even finer grid sizes. The fine detail often has a very small effect on the total energy or density which allow us again to limit the size of our Fourier series for these quantities. The grid scale is the ratio of the Fourier series for product terms, such as the density to that of the wavefunctions. For our calculations, the ratio of grid to fine grid was 2 to ensure accuracy.

3.3.3 Reciprocal Space Sampling

The electronic states need to be sampled at some number of points in the Brillouin zone to accurately solve for the wavefunction of the infinite crystal. The only interaction between these points in the Kohn-Sham equations is through the density which gets updated at the end of a KS minimization step and thus the KS equations can be solved very efficiently in parallel. For sampling, we use an unbiased grid of evenly spaced points in a 3 dimensional grid, called a Monkhurst-Pack grid[19]. This set is useful, as an $n \times n \times n$ grid captures interactions with up to the nearest n^{th} neighbour unit cells.

3.4 Orthonormality

As electronic states are eigenstates of the Hamiltonian, they should be orthogonal. Unfortunately as we are not directly diagonalizing the Hamiltonian, we do not naturally achieve this orthogonality. Instead it must be imposed upon the wave functions. This is achieved by applying an orthogonalisation scheme to both the original trial wave functions and to the search directions.

The Gram-Schmidt scheme is chosen due to its simplicity and ease of implementation. Each vector in turn is orthogonalised to the set of vectors which have been already orthogonalised. This is done by calculating the

projector of the vector onto this set and removing this projection from the original non-orthogonal vector. In this way, a set of vectors $\{v_n\}$, can be orthogonalised in turn,

$$v'_n = v_n - \sum_{i<n} \left(\frac{v_n . v'_i}{v'_i . v'_i} \right) v_i. \tag{3.5}$$

This is applied band by band to achieve a set of orthogonal trial wave functions. It has the disadvantage that it scales particularly poorly for systems with large numbers of electrons as there is a projector between each pair of vectors calculated. The scheme scales as $O(n_b^2)$ and so will come to dominate with large numbers of bands.

The vectors can then be normalised using,

$$v''_n = \frac{v'_n}{|v'_n|} \tag{3.6}$$

to create a set of orthonormal vectors.

The advantage in using this scheme is that the lowest bands are allowed the most freedom to find the energy minimum and this speeds the convergence of the Kohn-Sham energy eigenstates. Alternative mixing methods, such as that used in the Car-Parrinello method tend to leave mixed states which can make convergence difficult[6].

3.5 Minimization

Given the Kohn-Sham equations, one can formulate a method to find the energy minimum. The steepest descent direction (ie the vector in configuration space along which the total energy decreases most rapidly), including

the constraint of normalization, is given by

$$|\zeta_i\rangle = -\frac{\partial E}{\partial \langle\psi_i|} = -(H - \epsilon_i)\,|\psi_i\rangle\,, \tag{3.7}$$

where

$$\epsilon_i = \langle\psi_i|\,H\,|\psi_i\rangle \tag{3.8}$$

is the expectation value of the Kohn-Sham energy of the band. Expanding equation 3.7 in terms of Kohn-Sham states, we find

$$|\zeta_i\rangle = -\sum_{\alpha}(H - \epsilon_i)\,|\psi_\alpha\rangle\,. \tag{3.9}$$

Moving the KS states in this direction will lower their energy, but will break orthogonality. To correct for this, the search directions, ζ_i, are orthogonalised using the Gram-Schmidt scheme.

3.5.1 Steepest Descents

The most basic minimization scheme using this information is the steepest descents algorithm. From a trial starting configuration, x_1, a quadratic line minimizer is used to find the lowest energy point, x_2, along the direction, ζ_i search direction. The line minimizer operates by sampling the value of the function at a trial point along the search direction and then extrapolating a quadratic function to find an approximate minimum.

This point is then used as the starting point for the next line minimization. As the total energy is a minimum along this direction by definition, successive search directions will be orthogonal. This restriction can lead to difficulties when the energy landscape is not quadratic around the energy minimum, and it can take this minimizer a long time to find the actual

minimum.

3.5.2 Conjugate Gradients

The requirement that successive steps in the minimisation of the total energy must be orthogonal can be relaxed by methods such as conjugate gradients. In this method, rather than the search directions being orthogonal, they are made to be conjugate to one another with respect to the gradient operator, G,

$$\langle d_n | \, G \, | d_m \rangle = 0 \text{ for } n \neq m, \tag{3.10}$$

where $|d_m\rangle$ is the conjugate search direction for step m.

At first glance, this would seem to require knowledge of all previous search directions, but by construction, we can create a set of vectors which are mutually conjugate using only the previous search direction, $|d_{m-1}\rangle$ and the current gradient, $|g_m\rangle$,

$$|d_m\rangle = |g_m\rangle + \gamma_m \, |d_{m-1}\rangle \, , \tag{3.11}$$

where

$$\gamma_m = \frac{\langle g_m | \; g_m \rangle}{\langle g_{m-1} | \; g_{m-1} \rangle}. \tag{3.12}$$

This method takes into account the gradient at previous trial points into the current descent direction to improve the rate of convergence. With conjugate search directions, the minimization steps are independent of each other and should converge at a rate of one dimension in the vector space per iteration. When the dimensionality is reduced to 0, the local minimum has been found although it generally takes many less steps than this to actually achieve convergence due to preconditioning.

3.5.3 Preconditioning

The energy landscape has a very large dimensionality due to the number of plane waves in the basis set. It is generally well behaved and (in non-magnetic systems) has a single global energy minimum. Unfortunately, the gradient of the total energy puts greater emphasis on high energy basis states due to the high kinetic energy of these states, as in equation 3.9 and these will tend to be optimised first.

To alleviate this situation, we can amend the search direction by "pre-conditioning" it to favour the lower energy basis states. In principle, it is possible to find a perfect preconditioning matrix which would nullify the prefactor of $(H - \epsilon)$ but this would be very computationally expensive to calculate and apply as it would be a matrix of n_{pw}^2.

As the highest energy eigenstates are dominated by their kinetic energy, an approximation to the perfect preconditioning matrix can be given by a diagonal matrix which is the inverse of the kinetic energy operator for high energy eigenstates. For low energy eigenstates, the potential and kinetic energies are comparable and so this should tend towards unity for these states.

3.5.4 Charge Sloshing and Density Mixing

Charge sloshing is the oscillation of charge between iterations of the self-consistent field. As the density is only recalculated when the KS states have converged, one can imagine a system whereby the electrons repeatedly move from regions of high to low density in one step, only to move back in the next iteration as the density is updated.

Density mixing dampens these oscillations by mixing the new electronic density with previous electronic densities. This mixed density is then used

to generate the potential used for electronic minimization. Linear mixing combines the current and previous density in a linear way:

$$\rho_{in}^{n+1} = \alpha\rho_{out}^{n} - (1-\alpha)\rho_{in}^{n}, \tag{3.13}$$

where ρ_{in}^{n} and ρ_{out}^{n} are the densities at the beginning and end of SCF cycle n and α is the mixing coefficient. Although linear mixing is computationally fast and easy to implement, it is found to converge slowly as it discards information from the subspace explored after the next iteration.

Alternative mixing schemes include Kerker mixing[20], which mixes low spatial frequency(long-range) components more strongly than high frequency components as they contribute more to charge sloshing. It is defined by the operator,

$$K\rho = \alpha\frac{G^2}{G^2 + G_0^2}\rho, \tag{3.14}$$

with G being the Fourier wavenumber and G_0 being an arbitrary value defining a *long-range* for electronic coordinates. The new density is given by

$$\rho_{in}^{n+1} = \rho_{in}^{n} + K\left[\rho_{out}^{n} - \rho_{in}^{n}\right]. \tag{3.15}$$

Generally the Broyden and Pulay schemes[21] are used which use densities from N previous iterations. The Pulay mixing scheme assumes the residual and density are assumed to be close enough to the true solution that they are linear combinations of previous residuals and densities. It constructs an error vector which is given by

$$R_{n+1} = \sum_{i=n-N}^{n} \beta_i \left[\rho_{out}^{i} - \rho_{in}^{i}\right]. \tag{3.16}$$

The value, $|R_{n+1}|^2$ is minimized with respect to β_i under the constraint that

$\sum_{i=n-N}^{n} \beta_i = 1$. The new density is then given by,

$$\rho_{in}^{n+1} = \sum_{i=n-N}^{n} \beta_i \left[\rho_{in}^{i} + K \left(\rho_{out}^{i} - \rho_{in}^{i} \right) \right] \tag{3.17}$$

Although this method requires more computation to calculate the values of the β_i coefficients, it is able to reduce the sloshing much better than straight linear mixing. As this method has knowledge of the previous N steps, it can effectively dampen charge sloshing with periods up to N.

Broyden mixing is a similar scheme but builds a Jacobian matrix from finite differences between SCF cycles. This is then used to give values for the β_i coefficients in equation 3.17. Both Broyden and Pulay schemes are of competitive speeds and the better mixing algorithm to use depends on the system in question.

3.5.5 Occupancy and Fermi Energy

Once the Kohn-Sham equations have been converged for an input potential and density, the energy eigenvalues will have changed unless the system has reached absolute convergence. In a metallic system, there are empty or partially filled bands which will change in energy relative to the Fermi energy. The occupancies, $f_{i,k}$ of these bands must be updated after the KS states have been changed. The simplest way to do this is to simply populate the lowest energy states until the total number of electrons are placed. After this, the electronic density is recalculated.

Doing so breaks the variational nature of a SCF step as the occupation numbers and KS are not then consistent with the density generated. Electronic smearing and density mixing help to alleviate this problem, but sloshing can still occur, especially in larger systems.

In Ensemble-DFT (EDFT), the density is updated every time the wavefunctions and occupation numbers are changed. This makes the whole scheme variational as the energy always decreases at each step, but as the density must be recalculated often, EDFT is much slower than non-variational density mixing. It can be useful in finding high precision solutions in systems that are susceptible to sloshing instabilities.

3.5.6 Convergence Tolerance

The convergence tolerance is the chosen limit in the change in total energy between several cycles that counts as being converged. This is decided upon based on the energy accuracy required for the results that are to be obtained. For example instantaneous nuclear forces require a higher convergence tolerance than large energy differences in defect formation energies. For energy differences on the order of 10 meV, a convergence tolerance of 1 meV would be required and smaller values of the tolerance would give better precision.

3.6 Symmetry

The unit cells of real crystals have many symmetries which we can utilize to reduce the computation required to solve the Kohn-Sham equations. Symmetries in real-space such as reflections in atomic positions cause symmetries in the electronic structure and these apply both in real- and reciprocal-space. Even in cases where the crystal only has P1 symmetry, there is still translational symmetry (discrete Fourier coefficients rather than a continuum). There is also time-reversal symmetry which is present in every system and is due to the invariance of physical laws under a reversal of time. The Hamiltonian is time-invariant and so from Kramer's theorem[22], there is a

degenerate state corresponding to every KS state, $\psi_{i,\mathbf{k}}$, given by

$$\Theta\psi(\mathbf{r})_{j,\mathbf{k}} = \Theta e^{-i\mathbf{k}.\mathbf{r}}\phi_{j,\mathbf{k}}(\mathbf{r}) = e^{i\mathbf{k}.\mathbf{r}}\phi^*_{j,\mathbf{k}}(\mathbf{r}) = \psi(\mathbf{r})_{j,-\mathbf{k}}, \tag{3.18}$$

where Θ is the time reversal operator which has the effect of complex conjugation. This can be optimised further as the density from both points in the BZ will be equal and thus the wavefunctions at these points need not even be calculated.

We require solutions to the Kohn-Sham equations at each k-point, but some of them will be related by symmetry. In the simplest case of an inversion in real space will lead to the degeneracy of energy eigenvalues at $\pm\mathbf{k}$ and the states are related as $\psi_{i,\mathbf{k}} = \psi^*_{i,-\mathbf{k}}$. Only a subset of the k-points are actually required to be solved directly and these are referred to as the irreducible wedge as they are the minimum set of independent k-points.

Futhermore, physical quantities such as the density and potentials must also obey these symmetries and this allows additional constraints to be imposed to reduce the degrees of freedom in the KS equations. Symmetry can also be used to restrict degrees of freedom in geometry optimization, as the forces and displacements on atoms and cell parameters must all be commensurate with the symmetry group.

3.7 Conclusion

We have given a practical method for the calculation of ground state properties as is performed in the CASTEP package. The methods chosen are suited best for small to medium periodic systems which are normally those of interest in condensed matter physics. In particular, they are well suited to studying BCS superconductors as these are generally bulk crystalline.

In the following chapter, we will show how this is expanded to calculate dynamics information about the electron-phonon interaction.

Chapter 4

Electron-Phonon Coupling

4.1 Introduction

In this chapter, we will show how the linear response algorithm works in practice. As we are calculating the first-order electronic response to a perturbation in the position of the ions, we require that we have a well defined ground state and that the energy landscape is smooth around this minimum as we will be examining its derivatives.

4.2 Ground State

The perturbative method gives the second order energy which is closely related to the second derivative of the total energy with respect to the motion of each ion. If we are not close enough to the true minimum, the result will not be the quantity that we are trying to calculate. This is especially likely in systems with anharmonic potential wells as the second derivative will change about the potential well.

4.3 Fermi Surface

The calculation of the Fermi surface is necessary to calculate only the matrix elements which link partially occupied bands in reciprocal space. Crystal momentum conservation requires that the final state satisfies $\mathbf{k}_f = \mathbf{k}_i \pm \mathbf{q}$ where $\mathbf{q}$ is the phonon wavevector. Energy conservation requires that the scattering of an electron is to a state with energy $E_{\mathbf{k}_f,j'} = E_{\mathbf{k}_i,j} \pm \hbar\omega_{\mathbf{q}}$. There is no restriction on the band index that may be scattered to so long as it obeys the energy and crystal momentum conservation. As the energy scale of phonons is much lower than that of the electrons, only occupied states within a few hundredths of an electron-volt of the Fermi energy will be within the phonon energy to an empty state. As this is a very small margin, we approximate this continuum of states by a surface of points which lie on the Fermi surface.

To actually find the Fermi surface, we must first finely sample the Brillouin zone. In order to do this, we require the ground state density which is calculated as shown in the previous chapter. This is then used for a series of non self-consistent calculations at a regular array of points across the Brillouin zone.

A regular array of points spanning the Brillouin zone is chosen depending on how accurately the Fermi surface is required to be. This is reduced by symmetry to an irreducible wedge of points in the Brillouin zone which are unique and do not map to any other point by any of the symmetry operations.

A non-self consistent solution of the Kohn-Sham equations is performed at each of these points using the self-consistent ground state density to get the energy eigenvalues at each point. This consists of solving the KS equations a single time at these points using the self-consistent ground state

density.

Comparing with the Fermi energy from the self-consistent calculation, we consider the eigenvalues below the Fermi energy to be occupied and those above to be unoccupied with a sharp cut-off. For each point we can calculate the number of occupied bands.

The irreducible wedge is then mapped, by symmetry, to give the maximum number of equivalent sampling points spread across the Brillouin zone. These will include the original regular array that was chosen, but may also include others that do not necessarily lie on the MP grid.

Voxels (3d pixels) are formed with corners lying at the original grid points. These voxels have two associated values - a minimum occupancy number, $O_{min}(x, y, z)$ and a maximum occupancy number, $O_{max}(x, y, z)$ of wave function sampled within or on the edge of it.

For each point which matches an original grid point, the occupancy is compared with that of the 8 voxels around it. The minimum and maximum values are modified to include the new value. For points which are not on an original grid point (i.e. they lie inside a voxel), the occupancy of the point is compared with just the cell that it lies in.

When this process has been completed for each k-point sampled, an array exists of the occupancies of the voxels. Any voxel in which the minimum and maximum values are not equal must contain a Fermi surface crossing (by virtue of the intermediate value theorem). All such points are added to an array of Fermi surface points. Furthermore, the values of $O_{max}(x, y, z)$ and $O_{min}(x, y, z)$ show which bands cross the Fermi energy in this region, as every band between $1 + O_{min}(x, y, z)$ and $O_{max}(x, y, z)$ is only partially occupied in this region.

This process will cause aliasing in the calculated Fermi surface, as the

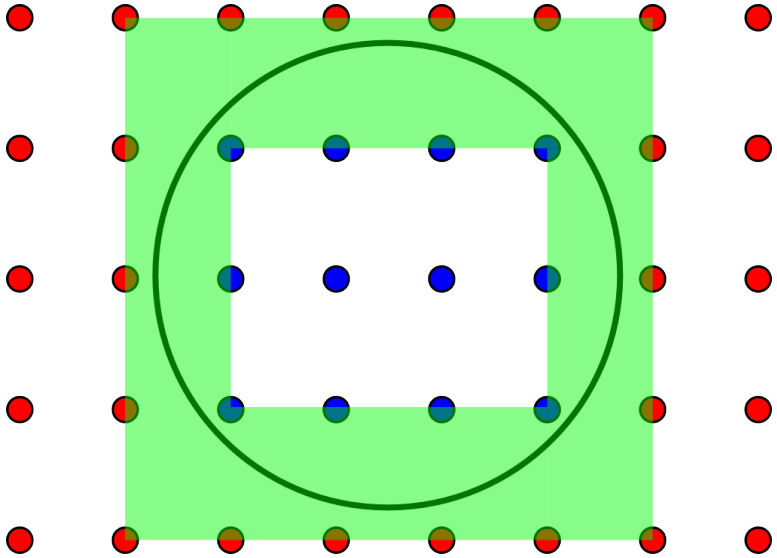

Figure 4.1: A 2d example of how the Fermi surface finding algorithm works for a spherical Fermi surface in a system with 1 band crossing the Fermi surface. Brillouin zone k-points are shown as circles. Red circles indicate the k-point has an occupation number 1 less than in blue circles. The green shaded area is the regions in which a band must cross the Fermi energy.

resulting points are restricted to a grid, but this can be reduced by using a fine sampling mesh. As this is only being used for a non-self consistent calculation, the computational complexity scales linearly with the symmetry reduced number of sampling points.

With knowledge of the full Fermi surface, a set of phonon-wavevectors can be constructed. The difference, $\mathbf{q}_{f,i} = \mathbf{k}_f - \mathbf{k}_i$ is calculated for every pair. These are reduced by symmetry to find those which are most representative of the total set of wavevectors linking Fermi surface points. We then proceed to the perturbative part of the calculation to study the properties of these phonons.

4.4 Perturbation

To be able to calculate phonon properties, we require the second order energy due to an atomic displacement in each of the Cartesian directions. Now many of these will be the same due to the space group of the crystal, but we still require an actual method of calculation.

There are two main methods of calculating the second order energy due to an atomic displacement: finite displacement and linear response.

4.5 Finite Displacement

The first is to directly move an atom a slight distance from the equilibrium point and calculate the resulting force on each atom in the system. This method requires that the displacements be periodic with the simulation cell and thus is restricted to phonon wavelengths that are commensurate with the unit cell, and the Γ point. It is particularly easy to visualise and to implement as it only requires properties that are available by ground state calculations. Each atom is shifted in both positive and negative directions, and the forces are calculated by the central difference approximation,

$$\frac{\partial^2 E}{\partial u_{\kappa,\alpha} \partial u_{\kappa',\alpha'}} = \frac{\partial F\kappa,\alpha}{\partial u_{\kappa',\alpha'}} \approx \frac{F^+_{\kappa,\alpha} - F^-_{\kappa,\alpha}}{2\Delta u_{\kappa',\alpha'}}, \tag{4.1}$$

where $F\kappa,\alpha$ is the force on atom α in unit cell κ and $\Delta u_{\kappa',\alpha'}$ is the finite displacement distance. The $+$ and $-$ superscripts indicate displacements in the positive and negative direction. As each displacement gives the force on each atom in the system, it will give an entire row of the dynamical matrix without requiring further electronic structure calculations. This means that only $3N_{sup}$ ground state calculations are required, but the number of atoms

in the simulation cell N_{sup} will vary with the phonon wavevector as the wavevector must be commensurate with the unit cell. To compute a phonon wavevector that is not commensurate with the unit cell, a supercell must be used which requires additional computational effort and this method will perform poorly.

4.6 Linear Response

The linear response perturbative method is an alternative method to directly calculate the total energy derivatives for perturbations. It has similar computational difficulty to the ground state system in terms of calculations per perturbation, and does not require the use of supercells for non-Γ point phonons. Linear response uses the Sternheimer equation to solve directly for the first-order wavefunctions and second order energies which directly give the second order energy derivatives.

The solution method is similar to the ground state method. A trial solution for the first order wavefunctions is taken, and these are used to calculate the first-order density. The Sternheimer equation is used to solve for the next step of wavefunctions and these are used to calculate a new first-order density. This process is repeated until self consistency is achieved to within the required tolerance.

4.6.1 Full Sternheimer Equation in Bloch form

The biggest advantage of DFPT is that the response to different phonon wavevectors are decoupled from each other. The Sternheimer equation (2.52) given in Bloch form for metallic systems[16] is,

$$\left[H_{KS} + Q^{\mathbf{k}+\mathbf{q}} + \epsilon_n\right] \left|\psi^{(1)}_{n,\mathbf{k}+\mathbf{q}}\right\rangle = -\left[f_n^{\mathbf{k}+\mathbf{q}} - P_n^{\mathbf{k}+\mathbf{q}}\right] H^{(1)} \left|\psi^0_{n,\mathbf{k}}\right\rangle \qquad (4.2)$$

where, P and Q are projection operators onto the occupied and unoccupied subspaces as defined in equation 2.53 The first order change in the Hamiltonian is simply the change in external potential. We rewrite this in Fourier components,

$$H^{(1)} = \sum_{\mathbf{q}} v_{\mathbf{q}}^{(1)}(r) e^{i\mathbf{q}.\mathbf{r}} \tag{4.3}$$

The Sternheimer equation can then be written in terms of the Bloch functions as,

$$\left[H_{KS}^{\mathbf{k}+\mathbf{q}} + Q^{\mathbf{k}+\mathbf{q}} + \epsilon_n^{\mathbf{k}}\right] \left|\phi_{n,\mathbf{k}+\mathbf{q}}^{(1)}\right\rangle = -\left[f_n^{\mathbf{k}+\mathbf{q}} - P_n^{\mathbf{k}+\mathbf{q}}\right] v_{\mathbf{q}}^{(1)} \left|\phi_{n,\mathbf{k}}^{(0)}\right\rangle . \tag{4.4}$$

As can be easily seen, this contains only terms at a single phonon wavevector, $\mathbf{q}$. The first order response of the electronic wavefunctions $\mathbf{k+q}$ is dependent on the states at $\mathbf{k}+\mathbf{q}$. All the terms are lattice periodic with the result that supercells are not required for arbitrary phonon wavevectors.

The resulting situation is that we can calculate the response of the system to arbitrary monochromatic phonons at any point in the Brillouin zone with comparable computational effort to calculating the ground state properties.

4.6.2 Brillouin Zone Sampling

The ground state wavefunctions are calculated using the method in the previous chapter at a regular array of points within the Brillouin zone. For the case of an arbitrary phonon with wavevector, $\mathbf{q}$, we may have the situation where k+q does not lie on one of the calculated points. In this case, we use the already calculated ground state density and non-variational solution of the Kohn-Sham equations to calculate the wavefunctions at arbitrary points in the Brillouin Zone.

4.6.3 Solving the Sternheimer Equation

The problem in solving equation 4.4 is that again we do not wish to invert the operator on the LHS directly, as the computational complexity of this task scales as N_{pw}^3. The result will also contain the first order response of unoccupied KS states which are not required and do not affect the total energy to second order.

Instead, the equations are solved using the conjugate gradients algorithm to get only the first-order response of at KS states which are at least partially occupied. Furthermore, no details of unoccupied states from the ground state are required due to equation 2.44 which expresses the projector onto the unoccupied states as a sum over occupied states. The combination of these two factors allow the calculation to proceed with comparative computational effort to the ground state calculation.

4.6.4 Second-Order Energy

With the first-order density for a particular perturbation sufficiently converged, equation 2.36 can be computed to give a row of the dynamical matrix. Using symmetry, further elements of the dynamical matrix can be set based on the values calculated.

4.7 Electron-Phonon Coupling

Calculation of the electron-phonon coupling matrix elements (EPMs) require the first-order potential which consists of two parts.

The first order contribution to the external nuclear potential is calculated from analytic derivatives of the ground state pseudopotentials.

The other is local and variational, and contains the contributions from

the Hartree, exchange and correlation parts of the Hamiltonian. These are due to to the interaction of the ground state and first order electron densities. The local contributions are calculated directly as functionals of the first order density.

The local contributions to the potential are calculated as a side-effect of solving the Sternheimer equation. Once all the required perturbations have been calculated, the matrix elements are calculated from these stored potentials and the diagonalisation of the DM. The non-local parts are calculated as required as analytic modifications of the pseudopotentials which is fast as they are not variational.

4.8 Symmetry

The symmetry of a crystal will be reduced by lattice perturbation as the atoms are moved from their symmetry positions. The remaining symmetries will be a subgroup of the full space group of the crystal which are commensurate with the phonon-wavevector; the symmetries will be those which leave the wavevector invariant. A symmetry operation remains in the presence of a phonon with wavevector $\mathbf{q}$ if

$$\mathbf{q} = S_n\mathbf{q}, \tag{4.5}$$

where S_n is a symmetry operation of the full space group.

The remaining symmetry operations allow us to reduce the total number of perturbative calculations as they must apply to the electronic response in these systems. In the majority of cases we break the ground state time-reversal symmetry, as $2\mathbf{q} \neq \mathbf{G}$ and so $-\mathbf{q} \neq \mathbf{q} \pm \mathbf{G}$. There is an additional symmetry, S_t due to the time reversal symmetry of the phonon itself under

which $\mathbf{q} \to -\mathbf{q}$ and phyiscal properties undergo $f_{\mathbf{q}} \to f^*_{-\mathbf{q}}$. Although neither of these operations independently are commensurate with $\mathbf{q}$, in conjunction they do leave it invariant. This allows an inversion-like symmetry to be used if the system has a ground state inversion symmetry, I.

$$S_{I,t} = S_t S_i \tag{4.6}$$

This time-inversion symmetry is useful either by itself (i.e. with the identity matrix) or in combination with one of the symmetry operations. Finally, if the direction is antiparallel to the one we require, this can be fixed by multiplication of the potential by -1 by the definition of the first order potential,

$$V_q^1(\alpha, i) = \frac{\partial V}{\partial \mu_{\alpha,i}} = \frac{\partial V}{-\partial \mu_{-\alpha,i}} = -V_q^1(-\alpha, i) \tag{4.7}$$

For the actual perturbative calculations, the symmetry is reduced further by the perturbation of a specific ion i in a direction α. The quantities R_i and α are invariant under these symmetry operations as well as the phonon wavevevector.

The symmetry operations are used to transform the first-order local potentials between symmetry related atoms. An example would be the symmetry of a phonon with $\mathbf{q} = (0, 0, 0.2)$ in a crystal with a single atom at the origin. The potential due to a perturbation in the x and y directions is related by the symmetry operation where $x \to y$ and $y \to x$. The result is that we can reduce the number of perturbations that must be performed. A further improvement in using the remaining symmetry operations is that they will improve the accuracy of the result by enforcing physically necessary conditions on the first order density and wavefunctions.

4.8.1 Finding Symmetry Operations

When a q-point is initialised, the symmetry operations that exist, S_{full}, are tested to see whether they leave q invariant. If so, they are added to a list S_q for that q-point. These apply to the dynamical matrix and various first order parameters.

The perturbation further reduces the symmetry for the purposes of calculating the 2nd order energy change but we can use the larger group S_q to relate first order potentials.

When one of the first order potentials $V^1(\alpha, i)$ is found for an atom i in a direction α, a check is performed to find any atoms which match by a symmetry operation.

Every valid symmetry operation in $\mathbf{q}$, $S_{\mathbf{q},n}$, is applied to the original position, R_i, and direction, D_α,

$$R_{test} = S_{q,n}.R_i \tag{4.8}$$

$$D_{test} = S_{q,n}.D_\alpha. \tag{4.9}$$

Every other atom j position, R_j, and direction, D_β, is then selected in turn and compared against these test positions to see where both

$$R_{test} = R_j + m\mathbf{G} \tag{4.10}$$

and

$$D_{test} = D_\beta \tag{4.11}$$

where $\mathbf{G}$ is a lattice translational vector.

If these are true, then $V^{(1)}(\beta, j) = S_q(n).V^{(1)}(\alpha, i)$. The symmetry operations are performed in reciprocal space, to simplfy the effect of any

displacement part of the symmetry operation as these become phase changes. This operation is performed until every symmetry related potential has been found. The potentials have the same symmetries as the diagonal parts of the dynamical matrix as these values have a one to one correspondence through the Kohn-Sham theorem.

4.9 Interpolation

With the dynamical matrix at a point, q, the resulting phonon modes and frequencies can be found quickly by diagonalisation. If we wish to accurately sample phonon frequencies across the Brillouin zone, a large number of DFPT calculations would have to be performed, as one would have to be performed at each point of interest.

The dynamical matrix elements themselves can be interpolated, using Fourier transformations, across the BZ to find an approximation to the DM at arbitrarily positioned **q**-points. A relatively accurate set of reciprocal space force constant matrices(FCMs), at an equally spaced set of q-points is first found. The reverse of the Fourier transform, in equation 2.31, can be used to find the FCMs in real space. These constants are short-ranged due to the screening action of the electrons. This can be Fourier transformed back into reciprocal space to get the FCM at any arbitrary **q**-point.

This is generally used by finding the DM on a regular array of points within the BZ and then applying the interpolation along a path within the BZ to create band-structure diagrams or in the case of electron-phonon coupling to find the phonon frequencies on the Fermi surface.

While interpolation can be used directly on phonon properties, it requires further work to interpolate the EPMs. The general method is given by Giustino[23] and involves projecting the perturbed electronic states onto

Wannier functions in real space and utilizing the localisation of these states. This is not currently implemented. Interpolation is used to improve the shape of the Eliashberg spectral function, by giving the fine detail of the phonon spectral function, $F(\omega)$.

4.10 Acoustic Sum Rule

The position of the origin in a unit cell is completely arbitrary. A shift of the entire crystal in space should not affect the observable properties of that crystal. This symmetry manifests itself in the phonon spectrum as the acoustic branches going to zero frequency at the Γ-point in non-polar materials. The symmetry is expressed as

$$\sum_{s} D_{s,t}(\mathbf{q} = \mathbf{0}) = 0. \tag{4.12}$$

This is partially broken in the calculations by several terms being calculated in real space, such as the XC energies, and insufficient electronic Brillouin zone sampling, which yields DMs which are not converged to large enough ranges in real space. This insufficient sampling can cause the frequencies to go to a constant rather than to zero at the zone centre and thus violate the translational symmetry of real space.

The first method of correction is to increase the sampling of the real space grids by increasing the plane wave basis size or the density grid scale. The density must be on a grid of at least twice the density of the wavefunctions because otherwise aliasing can occur which can easily affect the results of these calculations. Furthermore, with the GGA functionals, higher sampling is required to calculate derivatives of the density accurately and so will affect the exchange correlation[24].

An alternative method of correction is to calculate the dynamical matrix at the Γ-point and subtract this from the dynamical matrix by

$$D_{s,t}(\mathbf{q}) \rightarrow D_{s,t}(\mathbf{q}) - \delta_{s,t} \sum_{r} D_{s,r}(\mathbf{q} = \mathbf{0}). \tag{4.13}$$

This both enforces the correct behaviour at $\mathbf{q} = \mathbf{0}$ as well as when $\mathbf{q} \rightarrow \mathbf{0}$, and so leaves the function continuous. It is commonly used as it reduces the sampling required to get the analytic result, but its use is not rigorously justified and it can lead to other artifacts appearing as seen in figure 4.2 where it causes a discontinuity at M. These problems can be alleviated by increasing the sampling of the real space grid so as to improve the accuracy of the dynamical matrices. This directly leads to smaller values of the correction but generally requires very fine sampling. As the perturbations break most of the symmetries of the BZ, the scaling of cubic systems goes as $O(N_{mp}^3)$ rather than the symmetry reduced $O(N_{mp}^2)$ found in ground state calculations, where N_{mp} is the size of the Monkhurst-Pack grid along one reciprocal lattice direction. This makes increasing the size of the sampling more costly than in the ground state calculations and there is an advantage to using this correction.

4.11 Convergence

As in the case of ground state electronic structure, the calculation of linear response requires that the system be sufficiently converged to get accurate answers. Correct diagonalisation of the DM to get the phonon frequencies and eigenvectors requires that the DM be sufficiently converged. The DM being converged relies on the accurate solution of the Sternheimer equation which again relies on the cutoff energy and the Brillouin zone sampling.

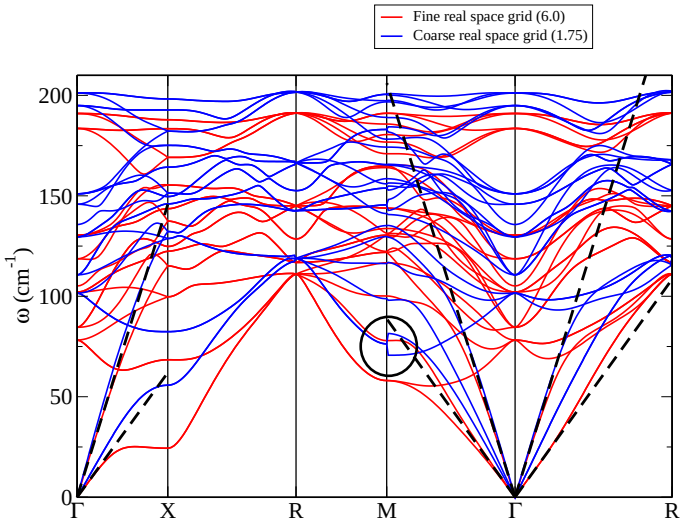

Figure 4.2: An example of the effects of enforcing the acoustic sum rule on an under-converged phonon spectrum in Nb_3Sn. One coarse and fine sampling dispersion curve are shown in blue and red respectively. The linear dispersion at the zone centre as calculated from the ground state is shown in dashed lines. The anomaly is circled at the M point.

The perturbative calculations are performed with the same basis set and Brillouin zone sampling as the ground state calculations so that aliasing and other unphysical interactions are avoided. All of the examples shown in this section were performed with face-centred cubic Au with a lattice parameter of 4.08 Å and using the PBE XC functional. The pseudopotential used considered the electrons in the 5p and 6s shells to be valence.

4.11.1 Basis Set Size

Figures 4.3 and 4.4 shows an example of the convergence of phonon frequencies and electron-phonon coupling constants with cutoff energy at a single phonon wavevector in Au. The frequency converges smoothly with cutoff energy above 300 eV, but that is not necessarily true if the basis set is much too small to be physical. At 200 eV, it is seen that the dynamical matrix fails

to diagonalise the two transverse solutions into non-degenerate modes. The frequencies of branches 2 and 3 are also lower than the converged values.

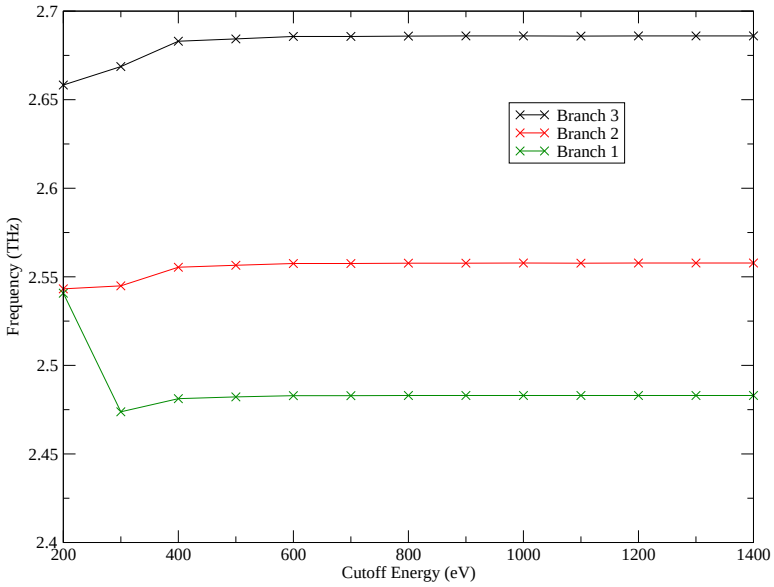

Figure 4.3: Frequency of the 3 phonon branches in Au as a function of cutoff energy used at an arbitrary $\mathbf{q} = (0.1, 0.2, 0.3)$. The Brillouin zone sampling grid was $18 \times 18 \times 18$. to ensure that the calculation was converged with respect to BZ sampling.

An energy cutoff of 600 eV was found to satisfy the convergence criteria for the ground state of $|\Delta E_{tot}| < 0.01\,\text{eV}$ per 100 eV change in E_{cut}. This suggests that the same cut-off energy can be used for perturbative properties as for accurate ground state properties. The electron-phonon matrix elements converge at approximately the same rate as the frequency as they depend linearly on the phonon modes produced by diagonalisation. This suggests that the accuracy of the EPMs can be inferred by the accuracy of the phonon frequencies.

The scaling of computational time with the basis set size is shown in figure 4.5. The lack of smoothness in the line is ascribed to the FFT requirement that the basis set be a multiple of small prime numbers (ie < 7)

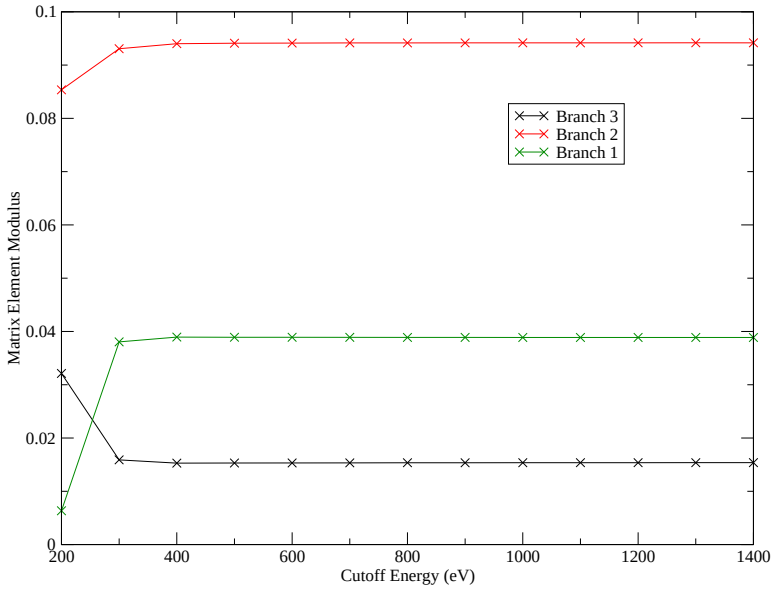

Figure 4.4: Modulus of the electron-phonon matrix element calculated between two arbitrary bands for the phonon branches shown in figure 4.3. The phase information was discarded as only the amplitude is necessary to find transition probabilities for electron-phonon scattering events.

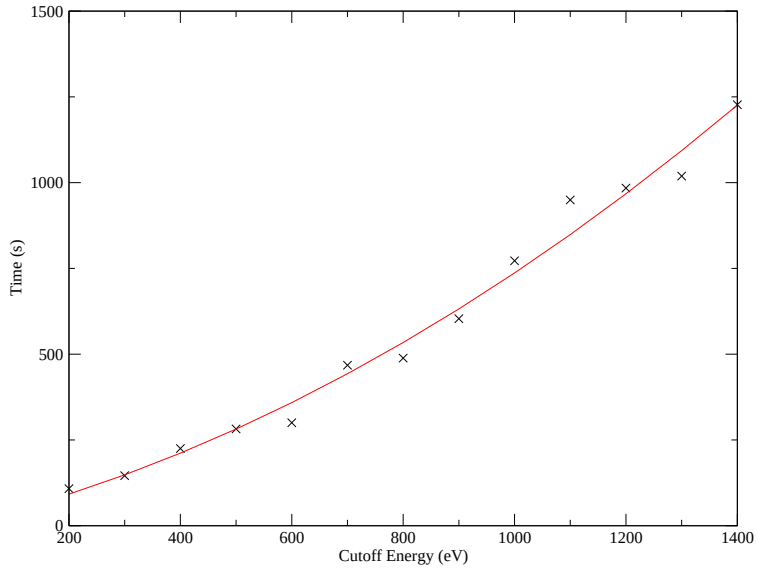

Figure 4.5: Comparison of the computational time with the cutoff energy used in the calculations. Plotted also is an E_{cut}^2 fit to the graph displaying the superlinear scaling of the calculation. The calculation was performed in serial to negate the effects of interprocess communication.

for efficiency. In comparison with figure 4.3 , it is obvious that above a certain point, large increases in computational effort result in only small increases in accuracy. At 600 eV, where the ground state is converged to within 0.01 eV, an increase of 100 eV in the cut-off energy results in a 56% time increase but only a 0.02% increase in accuracy in the EPMs.

4.11.2 Brillouin Zone Sampling

The sampling of the Brillouin zone shows a marked difference from the ground state in figure 4.6. This system was found to have ground state properties converged with a sampling grid of $8 \times 8 \times 8$. The phonon frequencies are found to vary by large margins up to a sampling size of $16 \times 16 \times 16$. This is likely due to the sampling of the Fermi surface being insufficient as these are the only states which can interact with phonons. It is also seen that the error does not necessarily go down with increased sampling sizes. This is due to the exact placement of sampling points within the Brillouin zone as they are evenly spread and centered around the Γ point.

The electron-phonon matrix elements, in figure 4.7, show an even stronger dependence on the Brillouin zone sampling than the frequencies. This is due to their dependence on the exact diagonalisation of the dynamical matrix. At $12 \times 12 \times 12$ sampling, there appears to be unrepresentative sampling of the Fermi surface states and so the dynamical matrix diagonalises in a slightly different way than for the cases of sampling sizes just above and below.

Again the accuracy of the phonon frequency gives us a guide as to whether our electron-phonon matrix elements will be converged. That the phonon frequencies are converged is used as the basic requirement of getting accurate EPMs.

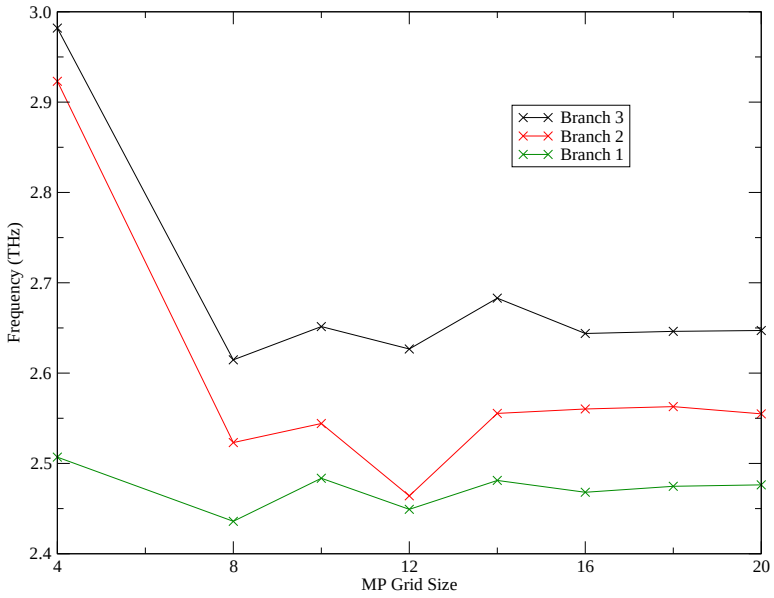

Figure 4.6: Frequency of the 3 phonon branches in Au as a function of Brillouin zone sampling grid ($N \times N \times N$) used at an arbitrary $\mathbf{q} = (0.1, 0.2, 0.3)$. The cutoff energy was set at 600 eV

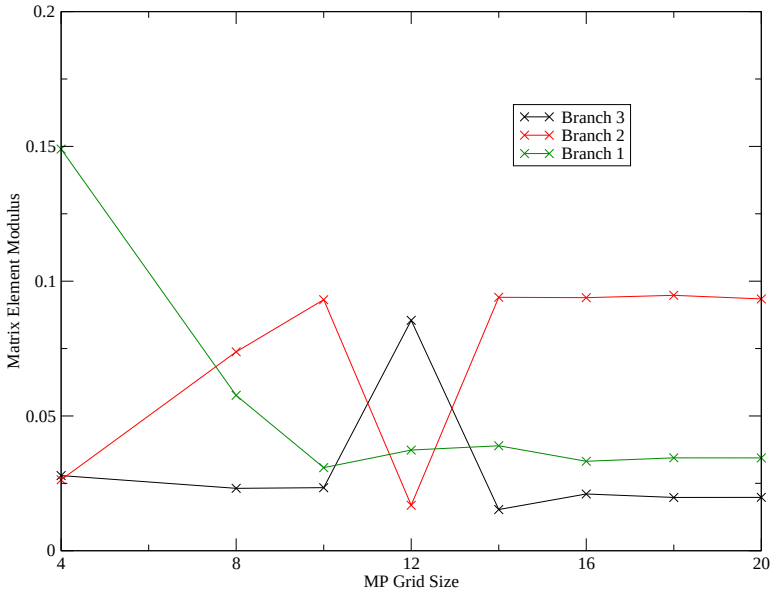

Figure 4.7: Modulus of the electron-phonon matrix element calculated between two arbitrary bands for the phonon branches shown in figure 4.6. The phase information was discarded as only the amplitude is necessary to find transition probabilities for electron-phonon scattering events.

As mentioned, most of the symmetry of the system is broken by arbitrary phonon-wavevectors and the computational-time scaling for an $N \times N \times N$ MP grid goes as N^3. This is the main hindrance in performing these calculations. The ground state calculation for a $20 \times 20 \times 20$ grid in this system has 770 unique k-points in the irreducible wedge. The symmetry in this system maps these points to 32000 points in the full Brillouin zone for which the Sternheimer equation must be solved.

4.11.3 Optimisation

The Sternheimer equations for each k-point are effectively independent of one another and so may be solved in parallel. The results are combined as the first order density by using MPI reduce instructions. This allows scaling of these problems to large supercomputing clusters – much larger than the ground state calculations – due to the huge number of k-points involved. As the calculations do not require the use of larger basis set sizes than the ground state, no further optimization is required there beyond those for the ground state. As we deal almost entirely in local potentials, only a small amount of memory is required for each k-point and memory usage effectively scales linearly with the number of Brillouin zone sampling points.

Symmetry often allows a reduction in the number of phonon-perturbations required. In the case of Nb_3Sn, with 8 atoms in the primitive unit cell, 24 perturbations would be required. This is reduced to 9 or 15 perturbations depending on the exact phonon-wavevector, offering a saving of $\sim 50\%$ computational time.

4.12 Calculation Summary

An overview of the steps for the calculation of the electron-phonon matrix elements are given in figure 4.8. Each self-consistent solution of the Sternheimer equation (the innermost loop) is of the same computational complexity as that of a ground state calculation. This is repeated $3N_{atoms}$ times for each wavevector of interest. To get an accurate sampling of the electron-phonon coupling across all the transitions possible, a large number of q-points must be sampled – at least hundreds for simple metals.

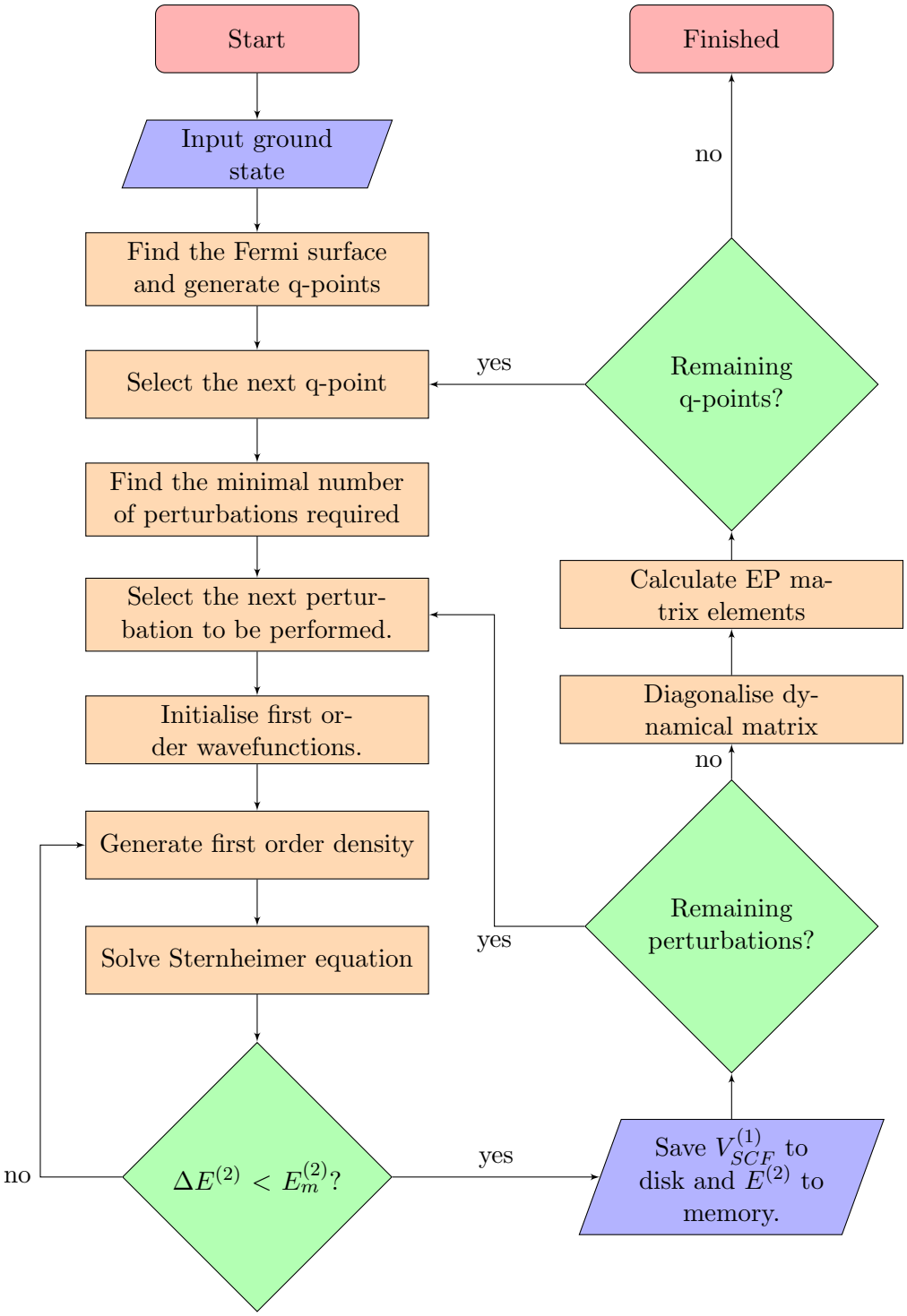

Figure 4.8: The process used to calculate the electron-phonon matrix elements from the ground state wavefunctions.

Chapter 5

Grain Boundaries in Au and Nb_3Sn

5.1 Introduction

Grain boundaries (GBs) control many properties of polycrystalline materials such as mechanical strength[25] and electron transport[26] and thus their manipulation has attracted a lot of interest in many fields including superconductivity[27] and semiconductor devices[28, 29] as they provide a relatively easy way to change the properties of a material.

In superconducting materials it has been found that increasing the disorder in the material can cause a large increase in the upper critical field, B_{C_2}, of materials. This can be controlled by changing the grain size[30] although it is difficult to model on the atomic scale. Empirical models based on BCS theory[2] employ parameters such as the normal state resistivity to calculate B_{C_2} along with several other parameters that are more difficult to measure, like the electron-phonon coupling[31].

In trying to characterise these materials, it is useful to look at the effects of grain boundaries as these defects begin to dominate materials' properties as the surface area to volume ratio increases. In particular, it is informative

to examine how the electronic structure changes as a function of distance from the grain boundary as this will affect both normal state conduction and superconducting properties through the interface. We can also probe the effects of isolated grain boundaries in materials to understand their individual effects rather than the entwined properties of many different defects, as would be observed experimentally.

Experimental study of defects in crystals can be difficult, due in part to the difficulty of isolating and probing defects at the atomic level, both close and far away from the surfaces. If the crystals are cleaved to allow direct surface observation of the grain boundaries, more complicated surface reconstructions may form which are not representative of GBs in the bulk. *Ab-initio* study of these grain boundaries can give insight into the electronic structure deep inside the material without suffering these effects. Due to the complexity of even the simplest grain boundaries, the majority of publications arising from calculations have used the embedded atom method[32] or even simple pair potentials[33] . These methods are very fast in comparison to full electronic structure calculations, but take a simplified view of distortions in the material. Although it is possible that these may give qualitatively correct results in many cases, they are known to perform poorly outside the crystal structure in which they have been parametrised[34].

Unlike point defects where the structural changes can be small and semi-empirical methods sometimes work well[32], grain boundaries tend to consist of large regions of local disorder where the structure is quite unlike that of the perfect crystal. A proper description of these regions requires that the electronic structure be dealt with in a more general way, such as density functional theory (DFT), with no empirical or semi-empirical parameters. Other calculations have tended to use computationally cheap methods, for

example tight binding model and muffin tin models to decrease the computational cost of the calculation, but again these methods are somewhat restricted in not being able to directly calculate local atomic distortions[35] and so will suffer from a loss of accuracy.

Pseudopotential based DFT is a prime candidate for calculating total energies and electronic structure properties of the defect regions as it does not rely on properties of the perfect crystal. Previous calculations which have used DFT[36, 37, 38] have tended to examine twist grain boundaries as they offer a smaller periodic system to look at, but tilt grain boundaries may have unique features not represented in pure twist GBs and so are of interest to study.

The difficulty in studying metallic systems is enhanced by the fact that they are conductors and exhibit no band gap. This gives these systems extra electronic degrees of freedom due to partially occupied bands. Modern linear scaling methods have been developed for large systems and generally require that all electrons be localised to some extent so as to keep the density matrix sparse[39]. This restriction means that the linear scaling of the calculation complexity with electron number does not apply to metallic systems where electrons may be completely delocalised and these methods are generally unsuitable.

Here, we examine the structural and electronic changes in the locality of symmetric tilt grain boundaries of conducting materials, using the ground state theory described in the previous chapters, to determine how different the microscopic environment is in these regions. In particular, we examine the density of states (DOS) at the Fermi energy, $n(\epsilon_f)$. Periodic boundary conditions are naturally fulfilled in a bulk crystal, but are more difficult to provide in defect systems and hence a method of creating periodic tilt

grain boundaries is discussed. Nb_3Sn was chosen as the representative BCS superconductor to study due to the large body of scientific study on this material, its relatively simple unit cell and common commercial use. Au was also studied as a representative conducting but non-superconducting material.

5.2 Periodic Grain Boundaries

Grain boundaries are challenging to study computationally due to the large amount of disorder and consequentially are of lower symmetry. However, grain boundaries with high translational symmetry along the direction of the interface have been found to be more common than those with longer more disordered structure due to the lower energy of systems with frequent common lattice sites[40].

When studying grain boundaries, the main issue is that at any arbitrary orientation, the crystals may not be of commensurate periodicity in directions parallel to the grain boundary. It is usually not possible to find a length that is a multiple of both crystal orientations parallel to the grain boundary due to these lengths being irrational. If periodicity is imposed in these cases, by using an approximately commensurate periodic length, there will be additional forces introduced which are not physical and are purely artefacts of the calculation[41]. In this study, we examine an idealised grain boundary which has a sharp divide between the two crystal orientations using the commensurate site lattice model to form periodic grain boundaries.

5.3 Commensurate Site Lattice

Highly symmetric tilt grain boundaries can be described by the commensurate site lattice (CSL) model[42]. These boundaries generally have atoms on or near the boundary which lie on a site which would be part of both lattices. At certain angles between grains, there are periodic common lattice sites between the two orientations of crystal and these are termed coincidence lattice sites. These individual atoms are at high symmetry positions and greatly decrease the extent of the disorder in the system by giving an atomic structure closer to that of the bulk material with only small regions of disorder.

In a cubic crystal, the CSL model assigns a value to a grain boundary based on the spacing between these periodic atoms (along the boundary line between the two crystal orientations) in terms of the lattice constant **a**. A $\Sigma 5$ GB would thus have a commensurate site with a periodicity of $\sqrt{5}\mathbf{a}$. This is shown in figure 5.1 for a simple crystal.

The angles giving these high symmetry situations are constructed by defining a vector which is a multiple of the real space lattice vectors. Both materials chosen are cubic which simplifies this calculation. We can define a generating vector which is a multiple of the real space lattice vectors which will be orientated along the a-axis. Another orthogonal axis must be chosen to keep fixed to fully describe the grain boundary. In this case, we have chosen the c-axis as it simplifies the rotations. If the crystal is cubic, as in the ones we have chosen, this will lead to a larger but still orthorhombic repeating unit. If this is reflected across the plane formed by the two vectors already chosen, we will create a grain boundary at the interface.

If the generating vector chosen is given by (a,b,c), the corresponding Σ value will be given by $\Sigma = a^2 + b^2 + c^2$. In our case, we have fixed the c axis

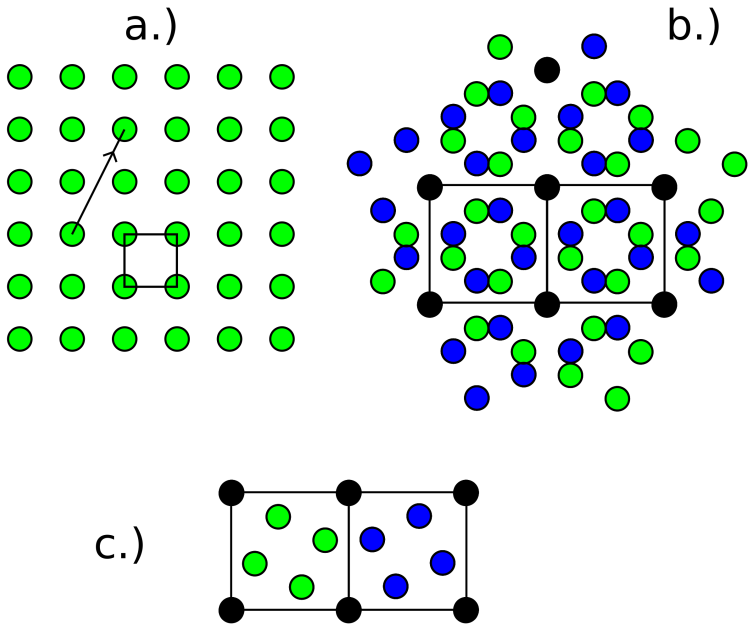

Figure 5.1: The simplest Σ5 grain boundary in a simple cubic material with rotations about the c-axis (into the plane). It involves a mismatch angle of 53.13°. Figure a.) shows the original unit cell and the generating vector (1 2 0). Figure b.) shows two crystals rotated in opposite directions by half of this amount overlapped. Shown in black are the overlaps of atoms. Finally, Figure c.) shows the resulting periodic grain boundary in its simplest form.

so the vector cannot have any component in this direction. If the Σ value would be even, there is always a more primitive commensurate unit cell that can be picked, although this is not necessarily periodic when attached to its mirror image as seen in figure 5.2. In these cases, the simulation cell is larger than indicated by the CSL Σ value.

5.3.1 Materials Studied

Metals can very loosely be split into two categories – those with a slowly changing density of states, with respect to energy, at the Fermi energy and

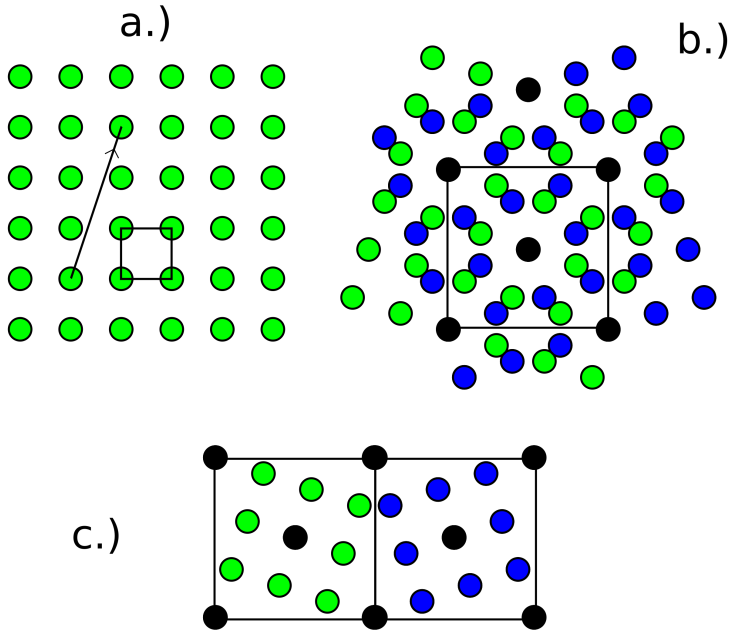

Figure 5.2: The second Σ5 grain boundary in a simple cubic material with rotations about the c-axis (into the plane). It involves a mismatch angle of 36.87° . Figure a.) shows the original unit cell and the generating vector (1 3 0). Figure b.) shows two crystals rotated in opposite directions by half of this amount overlapped. Shown in black are the overlaps of atoms. Finally, Figure c.) shows the resulting periodic grain boundary in its simplest form including the extra commensurate lattice site in the centre of the unit cells.

those with a quickly changing density of states. To representatively capture the essence of these situations, a material was chosen which fall into each of these groups. Pure face-centred cubic (fcc) gold was chosen as it has effectively a constant density of states close to the Fermi energy which is due to orbitals with sp-type character. There are d-like orbitals which give more complicated structure but these lie more than 3 eV below the Fermi energy.

Nb_3Sn was chosen as a material with a quickly changing DOS as the Fermi energy lies just on a peak in the density of states. It has a cubic

A15 crystal structure[43] with a body-centred cubic (bcc) Sn lattice with Nb ribbons arranged along the sides of the unit cell as shown in figure 5.3. Grain boundaries in this material are of special interest due to their ability to increase superconducting parameters like B_{C_2}[44] by increasing the normal-state resistivity in these materials.

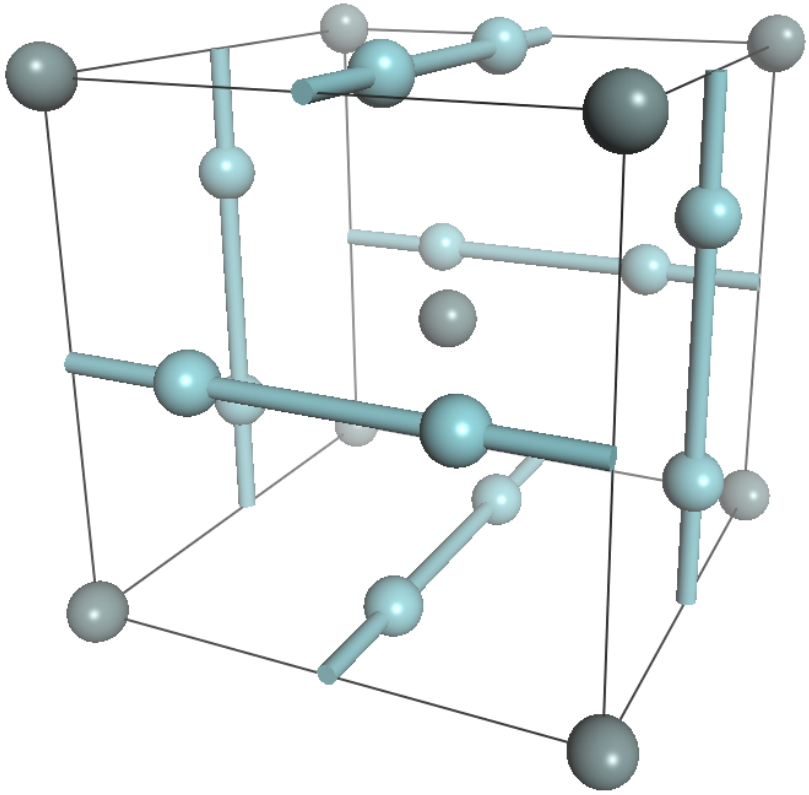

Figure 5.3: The unit cell of Nb_3Sn with Sn atoms at the corners and the centre and Nb atoms arranged on the sides as ribbons.

A range of simple GBs were created for Au and Nb_3Sn using the CSL method and are shown in Table 5.1. Atom pairs which were too close together (< 1 Å) were removed and replaced by a single atom in the average position of the pair as these closely compressed positions were unlikely to be energetically favourable. A single asymmetric $\Sigma 5$ GB of Au was created for

comparison by taking a 5×5×1 supercell of Au. This was the minimum size of supercell that could produce a Σ5 GB. This was rotated by 53.13°, which was calculated to be commensurate with the unrotated crystal as shown in figure 5.4 .

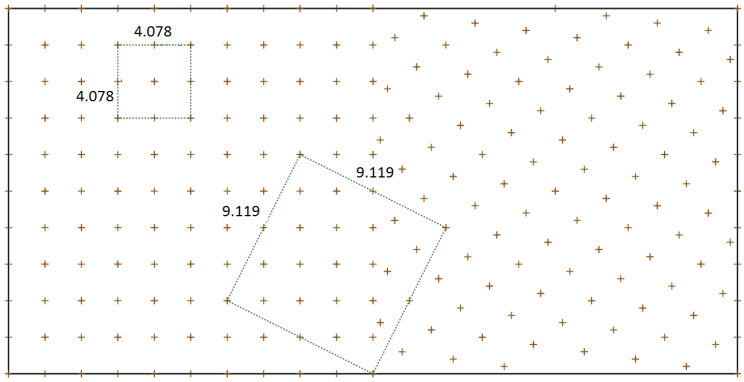

Figure 5.4: The periodic unit cell for an asymmetric Σ5 grain boundary in Au. The cubic unit cell is shown in the top left with a lattice parameter of 4.078 ÅAn example of the commensurate site lattice is shown as the larger square in the centre. As expected, the CSL cell has a volume of 5 times that of the simple unit cell.

The effect of two common impurities in Au was tested by repeating the calculation with a defect atom inserted into the grain boundary. These were chosen by the most commonly found impurities in highly refined Au and were selected to be Ag and Ne. These were placed in the central region of the grain boundary and relaxed to their local energy minimum.

The defect formation energy, ΔH_D as calculated by the formula of Lany and Zunger[45]:

$$\Delta H_D = [E_D - E_H] + \sum_{\alpha} n_\alpha \mu_\alpha, \tag{5.1}$$

where E_D is the total energy of the supercell containing the defect, E_H is the supercell without the defect and n_α describes whether atoms of species α are removed (+1) or added (-1) . The chemical potential μ_α is calculated

as the normally occuring state of the species. For Ne this is an isolated atom and the bcc structure for Sn.

Material	Generating Vector	Σ	Mismatch Angle	Atoms in Calculation
Au	(1 2 0)	5	53.13°	38
	(1 3 0)	5	36.87°	40
	(2 3 0)	13	22.62°	52
Nb_3Sn	(1 2 0)	5	36.87°	40

Table 5.1: The range of symmetric grain boundaries studied along with the angles and vectors to create them. Also shown is the minimum number of atoms required to create the cell and achieve convergence with respect to GB separation.

In Nb_3Sn there were multiple atoms which could be linked by the same vector using our simple grain boundary generation: The Sn or the Nb atoms which are symmetrically equivalent to all atoms of their own species. This means that multiple grain boundaries could be generated from the same generating vector. To observe if this had an effect, we performed the calculation using both orientations. This was not the case in Au, as the atoms were all symmetrically equivalent.

5.4 Results

5.4.1 Grain Boundaries in Gold

The PBE lattice parameter of Au was found to be 4.16 Å , which compares well with an experimental value of 4.08 Å[46]. The density of states at the Fermi energy was calculated to be $0.14\,\mathrm{eV^{-1}Å^{-3}}$, which corresponds to the carrier concentration of a good metal. The high DOS between $-7\,\mathrm{eV}$ and $-3\,\mathrm{eV}$ is due mainly to d-like orbitals and has a sharp density of states corresponding to localised orbitals as can be seen in figure 5.5. The density of states at the Fermi energy on the other hand has more of a sp-hybrid

character and is effectively constant in the region within kT of the Fermi energy where dynamical scattering effects can occur.

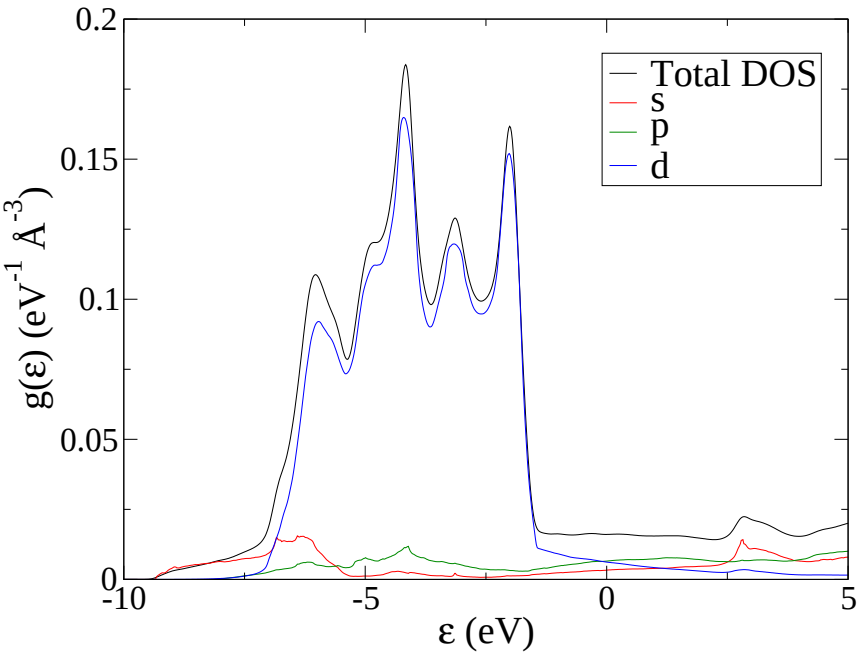

Figure 5.5: The density of states in fcc Au decomposed into angular momentum channels around atomic sites.

The formation energies for the Au grain boundaries are shown in Table 5.2 as calculated as

$$E_f = \frac{E_{gb} - N_{gb}E_{fcc}}{A_{gb}}, \tag{5.2}$$

where E_{gb} and N_{gb} are the total energy and number of atoms of the grain boundary cell, E_{fcc} is the total energy of the fcc unit cell, and A_{gb} is the area of the faces of the unit cell acting as a grain boundary region. The general trend is that as the interfacial area between CSL sites increases, the formation energy decreases.

The DOS of Au showed very little change for both the $\Sigma 5$ GBs to within the accuracy of the calculation. This is shown in Figure 5.6. In both cases, the detailed peaks in the 5d region was broadened and the peak heights

Grain Boundary	Interfacial Area per Cell ($Å^2$)	Formation Energy (meV/$Å^2$)
Σ5 (1 2 0)	14.2	47±1.0
Σ5 (1 3 0)	36.5	33.6±0.2
Σ13 (2 3 0)	36.9	25.7±0.3
Asymmetric Σ5	43.3	23.4±0.2

Table 5.2: The calculated formation energies for each of the grain boundaries in Au. Also shown for comparison are the interfacial areas in the smallest unit cell that can represent these boundaries. The error quoted is obtained from the numerical convergence criteria of 10 meV in the total energy of the relaxed systems.

reduced but these still remained more than 1 eV below the Fermi energy. In the region of the Fermi energy, the bands are s-like and very flat. There was little effect from the grain boundaries in these regions.

In the more disordered Σ13 grain boundary, shown in Figure 5.7, a drop of approximately 14% is seen in the DOS in the region around the Fermi energy. There is also a more substantial broadening of the d band region and it has been pushed 0.2 eV upwards in energy.

The asymmetric grain boundary density of states, seen in Figure 5.8, shows similar results to the Σ13 grain boundary with a more significant drop around the Fermi level. Compared with the symmetric grain boundary, it can be seen to have similar peaks that do not exist in the bulk material, but there are important differences. The energy eigenvalues associated with the d-band electrons have shifted to higher energies and a more significant drop is seen in the DOS at the Fermi energy.

5.4.2 Impurities in Au Grain Boundaries

The calculated defect formation energy for a Ne impurity is 1.98 eV which suggests that this defect is not energetically favourable and is not likely to be observed in the GB. The defect formation energy for the Sn impurity is

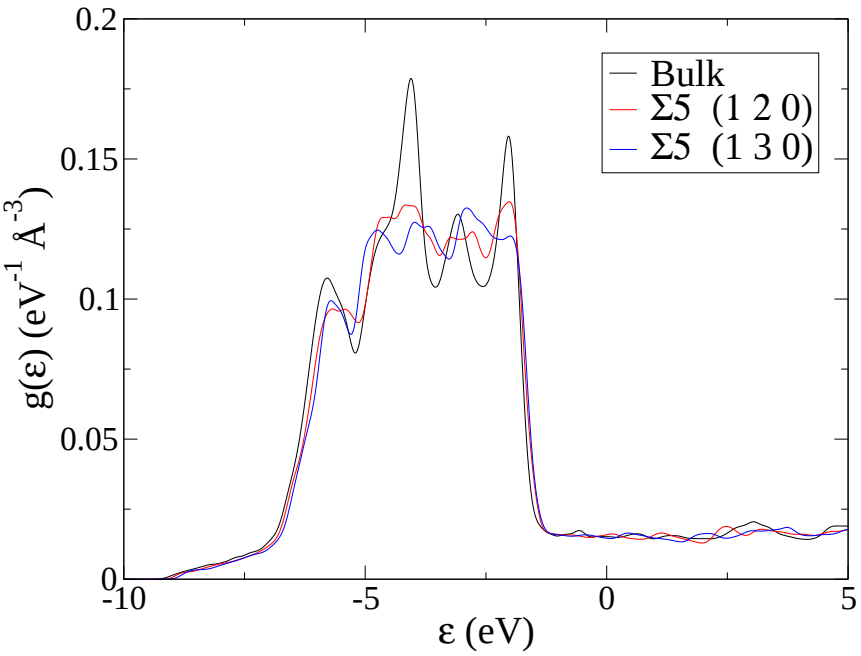

Figure 5.6: The density of states of the two Σ5 symmetric tilt grain boundaries plotted against the bulk density of states for pure fcc Au. The energy is given relative to the Fermi energy(0 eV). The DOS has been normalised per unit volume to allow comparison between different GB volumes.

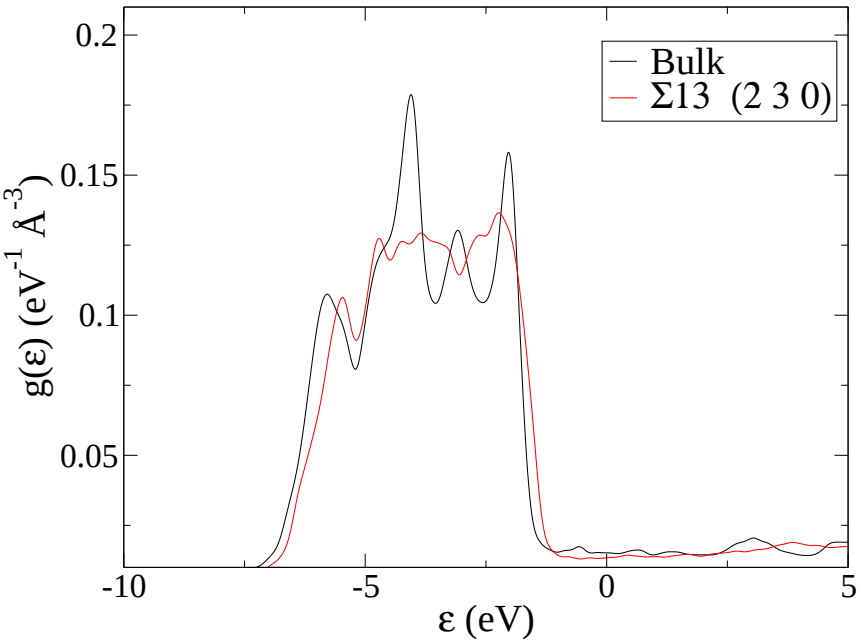

Figure 5.7: The density of states of the larger symmetric Σ13 tilt grain boundary compared with that of the perfect bulk Au crystal. The energies are relative to the Fermi energy.

−0.94 eV which suggests that this is a favorable position for Sn defects to form. This is likely because the Sn atom is smaller and more easily fits into the voids in the GB region.

The density of states for the GBs of Au containing Ne and Ag are shown in Figure 5.9 compared with the pure GB with no interstitial atoms. In the case of a Ag impurity, there is very little change from the pure Σ5 grain boundary and no observable effect in the region of the Fermi energy. Placing a Ne impurity into the grain boundary on the other hand does have a noticeable effect on the DOS, although at an energy much lower than the Fermi level. When a partial density of states is calculated for the Ne atom, it is seen that it only contributes to the total DOS in this region at −8 eV, and these localised states can be seen in the Kohn-Sham orbitals in Figure 5.10. In neither impurity is any change detected in the DOS at the Fermi

energy larger than 1%.

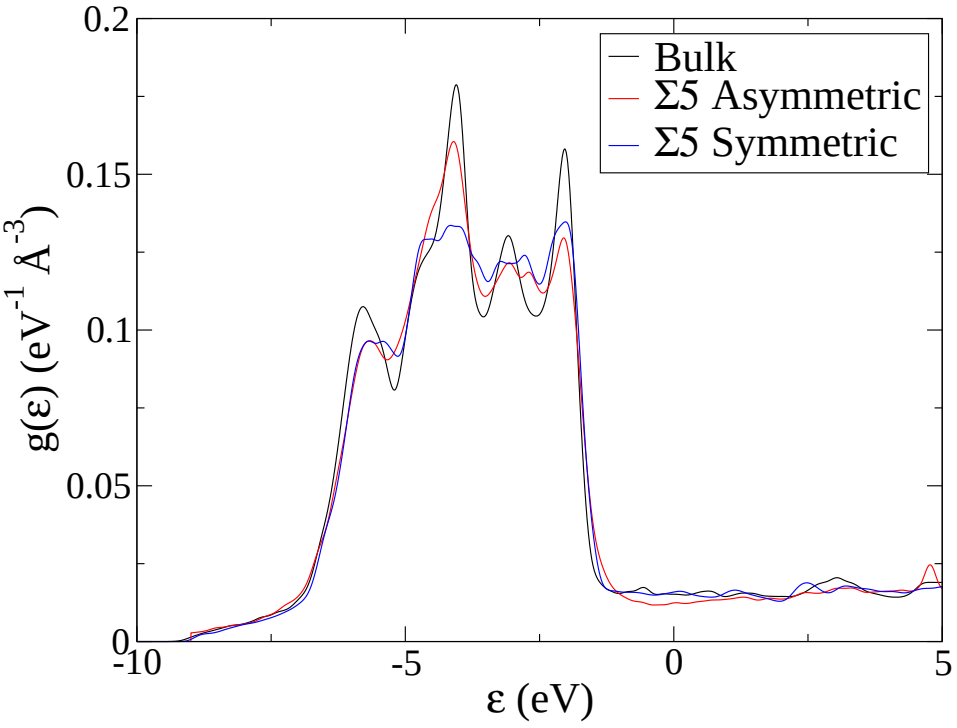

Figure 5.8: A comparison of the volume normalised density of states in the symmetric and asymmetric Σ5 grain boundaries in Au.

5.4.3 Grain Boundaries in Nb_3Sn

In the bulk A15 structure of Nb_3Sn, the lattice parameter was found to be 5.32 Å. This is close to the experimentally measured value of 5.29 Å[47]. The DOS for the perfect A15 structure is shown in Figure 5.11 combined with the partial density of states from each of the constituent atoms. As can be seen, the Fermi energy coincides almost perfectly with a peak in the DOS which is concentrated almost entirely around the Nb atoms.

The atomic relaxations were found to only be significant for the atoms immediately on the boundary, and even 2nd neighbours were very close to their bulk positions but the total energy required further separation of

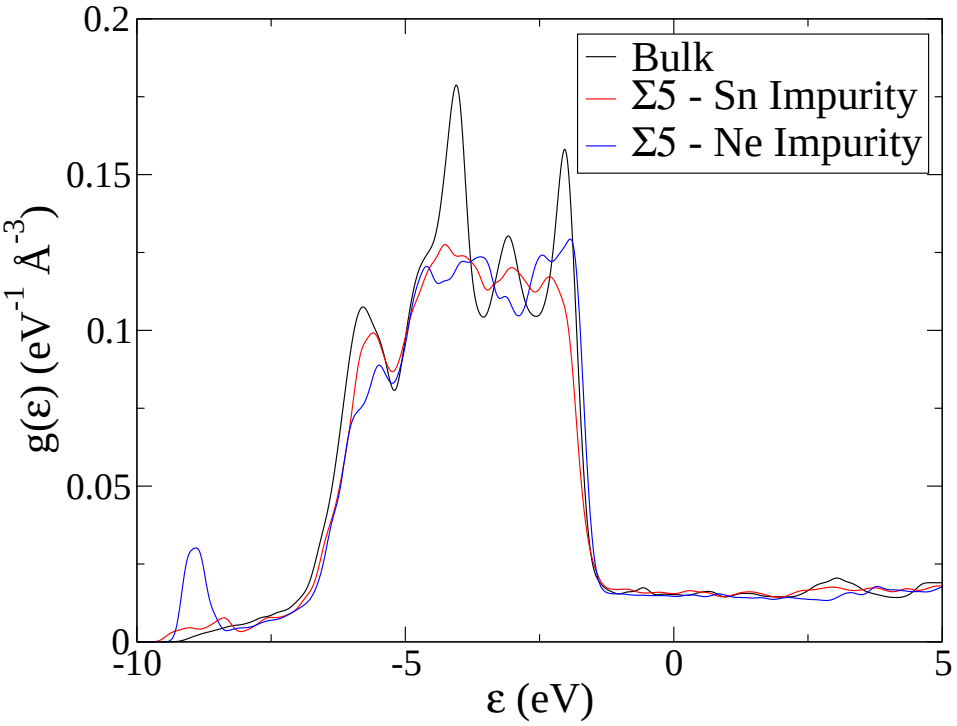

Figure 5.9: The density of states of a symmetric Σ5 with Ag and Ne impurities introduced in the grain boundary region. The energy scale is given relative to the Fermi energy.

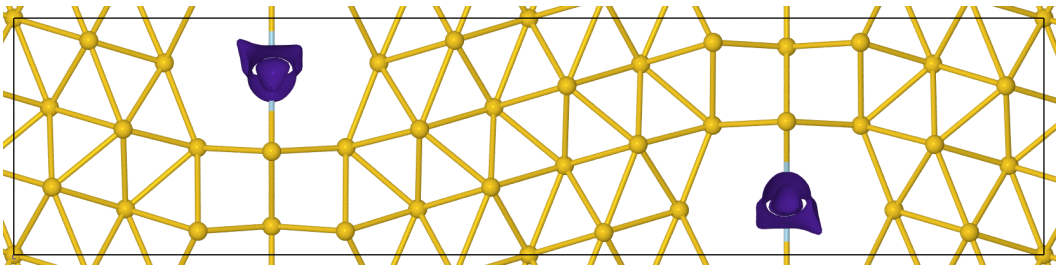

Figure 5.10: The localised states corresponding to the Ne atoms placed in the GB are shown in blue. The Au atoms are shown in gold and the Ne atoms in blue.

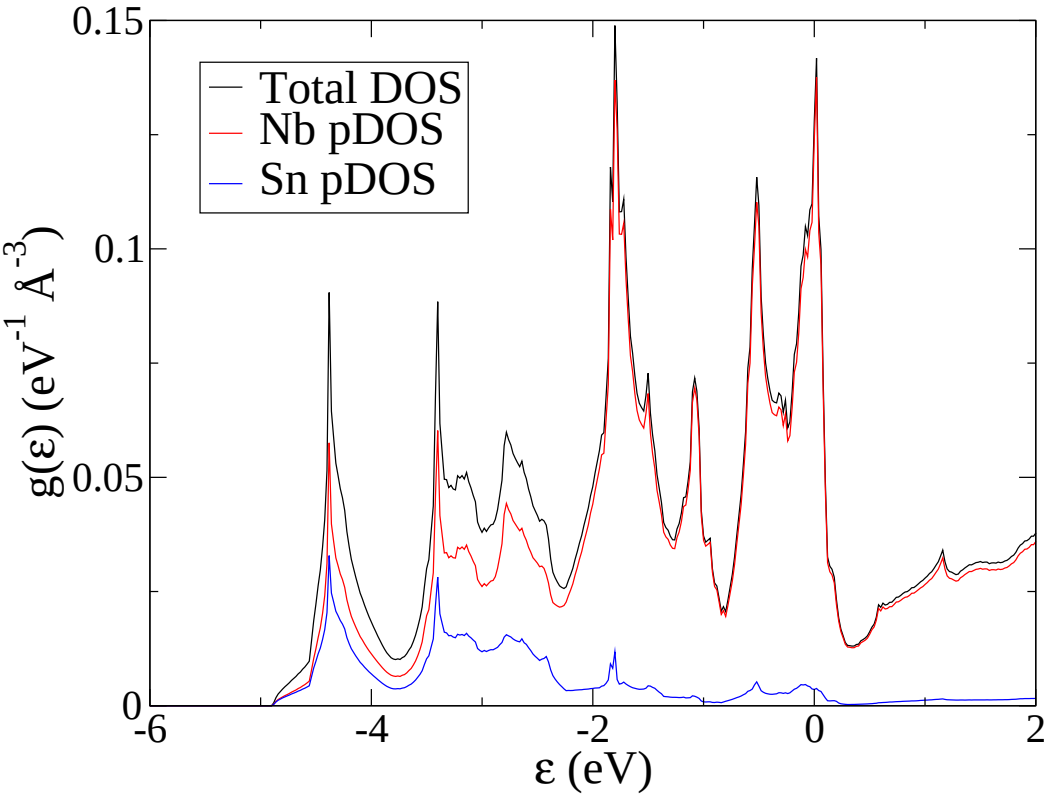

Figure 5.11: The total density states of Nb_3Sn compared with the partial density of states for each of the Sn and Nb atoms in the pure A15 structure. Every atom of each species is symmetry equivalent in the structure and has the same pDOS.

the GBs to achieve convergence. For this case, it is observed that there is a large drop in the density of states at the Fermi energy. The peaks are broadened from their bulk values and the density of states at the Fermi level has dropped from $0.132\,\mathrm{eV^{-1}\AA^{-3}}$ to $0.082\,\mathrm{eV^{-1}\AA^{-3}}$.

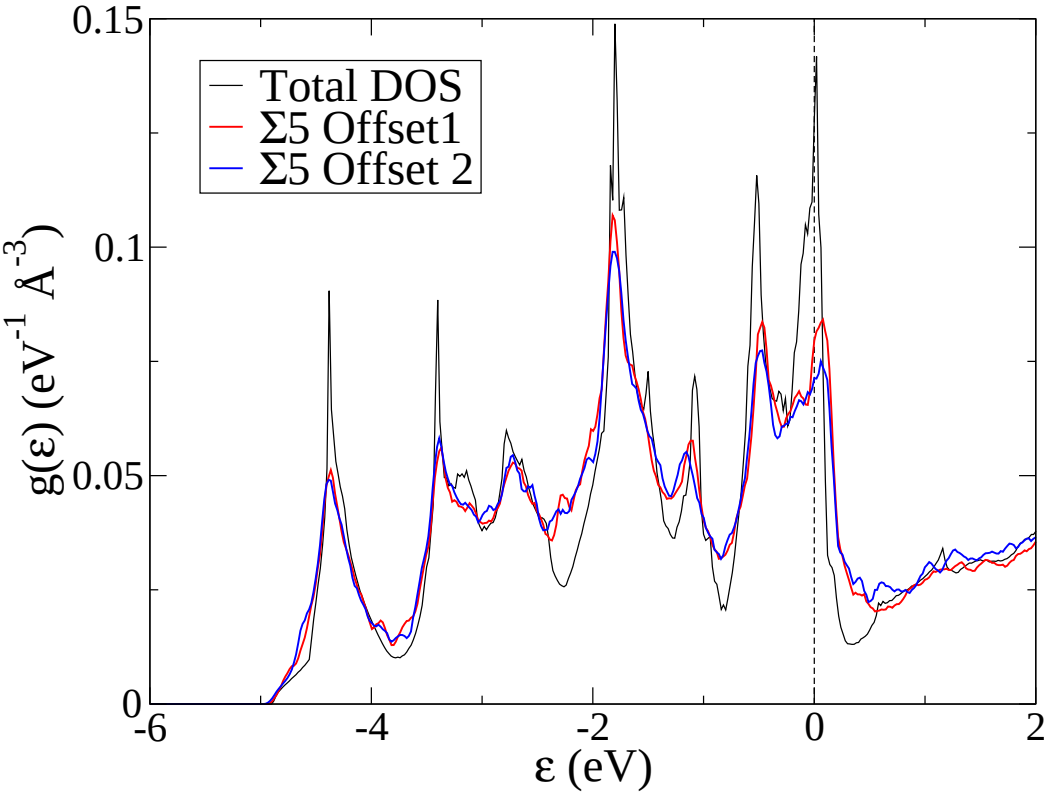

Figure 5.12: The density of states of bulk Nb_3Sn compared with that from the two main types of $\Sigma 5$ grain boundary which could be created. The Fermi energy is marked at 0 eV.

A comparison between the different repeating cell units that could be chosen for Nb_3Sn are shown in Figure 5.12. Although both are of similar character, there are differences observed, especially in the height and broadening of the peaks. Most importantly, the peak closest to the Fermi level differs noticeably and this leads to a difference of $7.2 \times 10^{-3}\,\mathrm{eV^{-1}\AA^{-3}}$ which is approximately 12% of the total decrease from the bulk value. In either

case, the density of states at the Fermi energy is observed to have a ∼40% decrease due to the presence of this simple grain boundary.

The formation energy for the grain boundary with Sn on the CSL site was calculated to be $0.167\,\mathrm{eV/\AA^2}$ compared with the formation energy calculated with the Nb atom on the interface, $0.243\,\mathrm{eV/\AA^2}$ and thus we would expect the Sn atom CSL site to be the dominant form of these two boundaries found in the material.

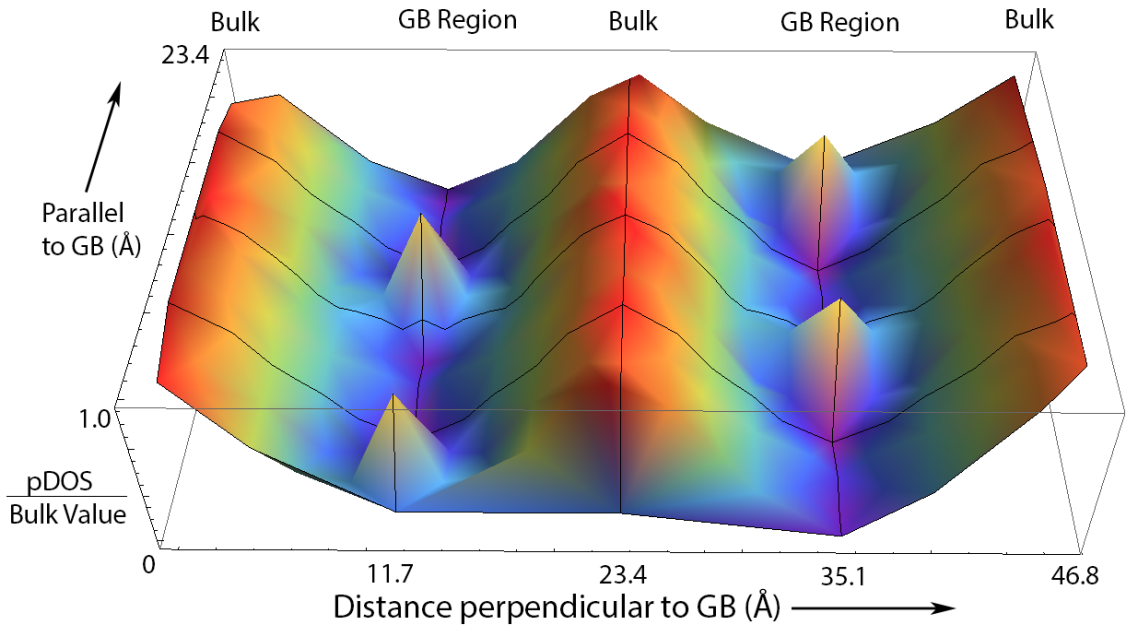

Figure 5.13: The partial density of states at the Fermi energy associated with each atom in the grain boundary relative to the bulk value. The origin has been shifted so that the grain boundaries are at $\frac{1}{4}$ and $\frac{3}{4}$ of the horizontal axis. The local DOS was found by projecting the total DOS onto atomic orbitals centred around each atom.

In Figure 5.13, it is seen that the grain boundary causes an effect on the electronic structure that penetrates much further into the material than the atomic relaxation shown in figure 5.14. Although there are several peaks in the grain boundary region, the density of states at the Fermi level in this region is much lower and only approaches its bulk value a considerable

distance into the material, on the order of 5 Å . The atoms within a few Ångstrom of the grain boundary have their density of states much reduced from the bulk value, and even at 11.7 Å from the boundary, $n(\epsilon_f)$ is still about 5% percent less than the bulk value, showing the large length scales for the relaxation of the electronic structure to the bulk result. This calculation was only performed for Nb_3Sn as Au did not show any major change in the DOS at the Fermi energy. There is a single atom in the centre of the the GB region which has a much higher $n(\epsilon_f)$ than the surrounding environment. This atom corresponds to the commensurate lattice sites in the CSL model.

Further insight can be gained by visualising the Kohn-Sham orbitals at and above the Fermi energy, as in Figure 5.15. The changes in density in the GB region are very similar to the atomic reconstruction and the density is actually bulk-like right up to the interface between grains. The KS orbitals at the Fermi energy are almost entirely in the bulk regions with an isolated state being found to form around the Nb atom which corresponds to the peak in Figure 5.13. The states which would correspond to the same kind of orbitals but in the grain boundary regions are found to have been shifted higher in energy to above the Fermi energy and so are unable to contribute to current flow in the material.

5.5 Discussion

5.5.1 Gold

The formation energy of these grain boundaries is relatively small. Thus we would expect to, and do, see many of them in experiment[40]. The values calculated are about twice of those calculated using the embedded atom method on a twist grain boundary[48], and this is likely to be an example

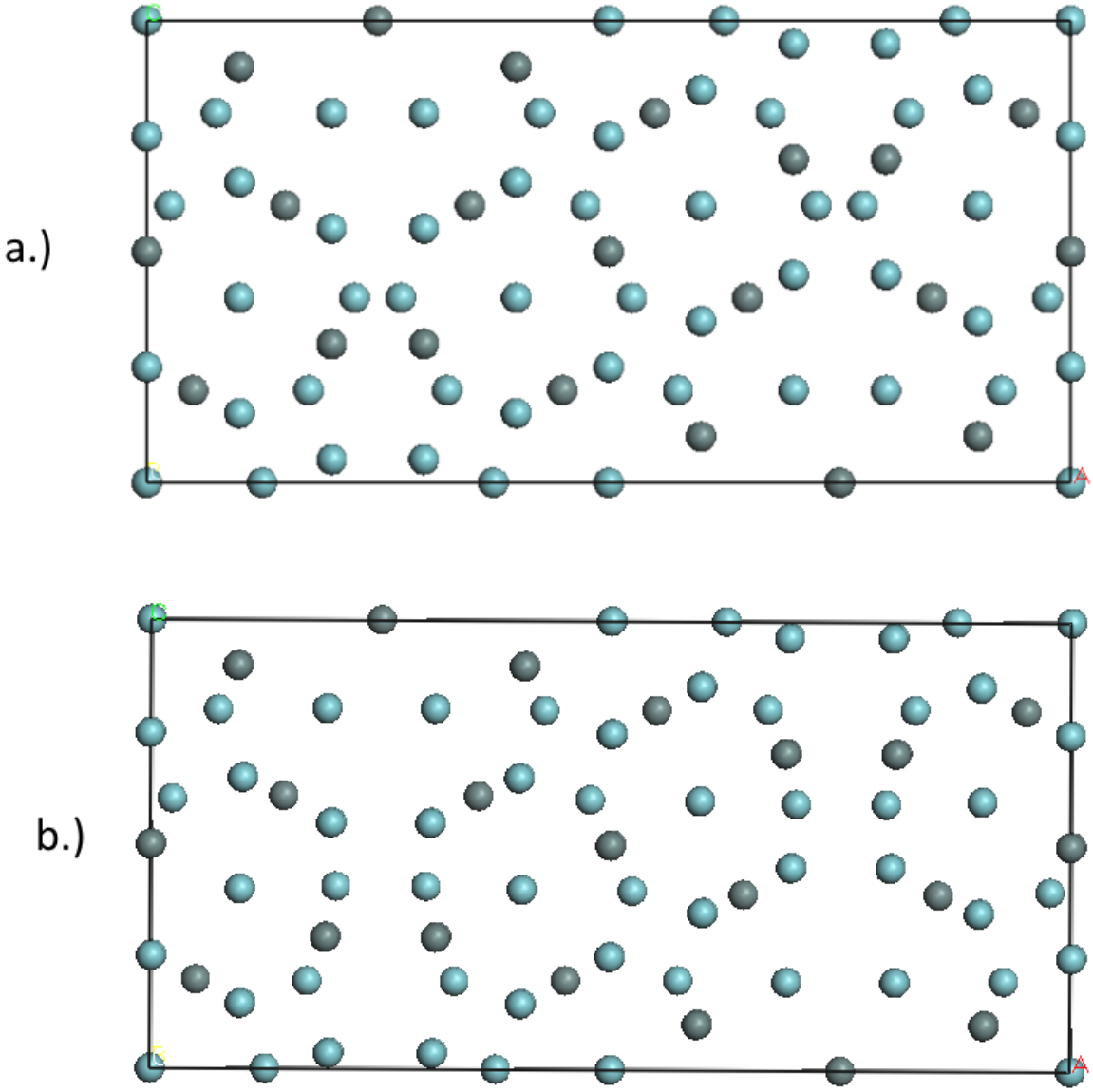

Figure 5.14: Example of atomic relaxation in Nb_3Sn for the GB with Sn on the CSL lattice site. a.) Unrelaxed unit cell, which is effectively two bulk regions with different orientations. b.) Relaxed unit cell where atoms were free to move to the local minimum. Only the atoms very close to the grain boundary show any noticable change.

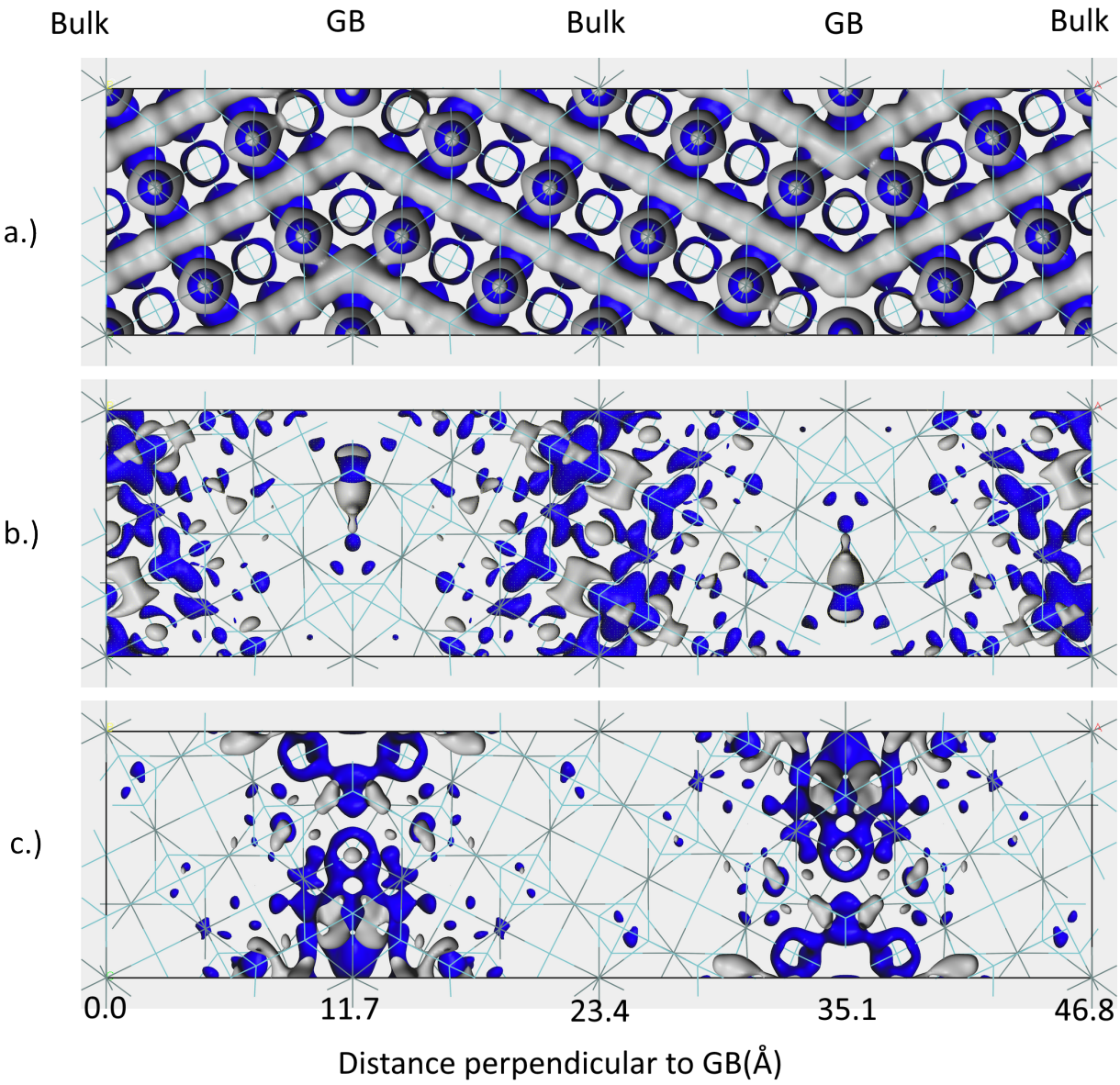

Figure 5.15: a.) The total ground state density of the Σ5 grain boundary in Nb_3Sn. b.) An example of the electron density of orbitals whose eigenvalues cross the Fermi energy. c.) The electron density from the KS orbitals whose eigenvalues lie just above the Fermi energy.

of material in these regions being very different from the bulk.

The simplest grain boundary structures do not appear to show changes in the DOS around the Fermi level. This is likely because it is highly periodic along directions parallel to the grain boundary. In the CSL model, this would indicate that a large number of the atoms along the GB lie on coincidence, energetically-favourable sites for both orientations of crystals. The fact that the formation energy is slightly higher for these structures is because the very low order Σ grain boundaries repeat often and that there is an interaction energy involved in having these defects close to each other as the different orientations have less space along the GB to allow relaxation. In the larger Σ values, the defects are spaced further apart and this interaction energy is reduced. The high symmetry in this case also prevents much relaxation around the boundary and so there is little broadening of the energy levels.

For the more complicated structure of the $\Sigma 13$ boundary, there are more atoms which are not on CSL sites and become further perturbed from their positions in the perfect crystal. There is more disordered structure in the grain boundary region and this leads to further broadening of the DOS.

Overall, for Au grain boundaries, almost no change is seen in the density of states around the Fermi level. This is because even though bands are broadened in energy, the density of states for Au is constant within 0.2 eV of the Fermi energy as it is made entirely of sp-like states which produce a flat density of states due to the quite delocalised electronic states. These states are effectively unchanged by broadening until the distortions are large enough to push the 5d electrons into this region. When this occurs, it actually induces a drop in the DOS as more states gain d-like character.

The negligible change in $n(\epsilon_f)$ indicates that, as far as the electronic structure is concerned, the entire region retains the same number of charge

carriers available for conduction as the bulk. There are also the same number of states available at the energies around the Fermi energy and so we would not expect to see large reflections of electrons at this interface.

Important to note is that these symmetric tilt grain boundaries studied here are special low energy cases as predicted by the CSL model and may not be representative of every grain boundary in the material. The large asymmetric grain boundary has a large amount of mismatch along the interface, and so may be more similar to general grain boundaries. Even in this case, only a small change is observed in the DOS at the Fermi energy and so it can be concluded that these tilt grain boundaries do not have much effect on $n(\epsilon_f)$.

5.5.2 Nb_3Sn

In Nb_3Sn, it is observed that even the simplest repeating grain boundary shows a significant drop in the density of states at the Fermi energy. This is because this material has a much more rapidly varying DOS, with numerous peaks of small widths, in the region near the Fermi level .

The formation energies for the GBs in Nb_3Sn are much higher than that in Au, implying that they will be more rarely observed. This may be offset by the common preparations of Nb_3Sn strands where they are normally sintered at high temperatures for many days. Non-stoichiometric Sn content is used to avoid formation of the cubic phase[49] and this may also encourage formation of the GBs as Sn atoms preferentially occupy the GB interface. Further study would be required to examine this effect including calculating the formation energies of alternative structures of the grain boundary with varying numbers of Nb and Sn atoms in the region of the GB.

The calculations presented here show that grain boundaries with the

same Σ value can have a substantial, 12%, difference in their effect on the density of states at the Fermi energy as the relaxation of the atoms in the GB region will depend on the coordination numbers of the atoms at the CSL site. This magnitude of variance is also seen in experimental work in bicrystals in resistivity measurements[42]. The $\Sigma 5$ grain boundary is also seen to affect the electronic structure on much larger scales than those over which the electronic structure relaxations occur. The large length scale that $n(\epsilon_f)$ is seen to vary over may be related to the sharp peak in the DOS that the Fermi energy lies on in the bulk, as even a small variation in energy will cause a large drop in the density of states.

In terms of the electronic contribution to the resistivity, the grain boundary will have the effect of scattering electrons which would otherwise conduct through the region as there are fewer states at the Fermi energy in the grain boundary region. This will lead to an increase in resistivity across the grain boundary. A rudimentary calculation using the Drude model, assuming the electron mobility remains constant in the grain boundary region, gives an increase of 81% in the resistivity over the bulk value in a region extending 11.7 Å on either side of the grain boundary. As the upper critical field, B_{C2}, is proportional to the normal state resistivity, the changes observed in these materials by the artific/ial introduction of GBs can be explained by this increase in resistivity.

The conducting bands in the region of the grain boundary are pushed to higher energies by the disorder in the atomic positions. This pushes them higher than the Fermi energy and so they cannot take part in electronic conduction through the GB. In practical terms, any conduction through the GB will be due to tunnelling through the region to the defect state centred around the Nb atom from the bulk regions. This region is approximately

10 Å wide where the DOS is lower than half of its bulk value. Due to the exponential dependence of tunnelling on distance, the relatively large region between the bulk and the hopping site will lead to a highly resistive region.

The electron-phonon coupling is, to first order, equation 2.57, proportional to the number of states at the Fermi energy[50]. The severe decrease, of 81% in $n(\epsilon_f)$ in the GB regions will effectively leave them as normal-state regions when the bulk is superconducting unless the temperature is much lower than the critical temperature, T_c of the material. For Nb_3Sn, T_c is 18.3 K[51], and the material would require that the temperature be brought down to the order of 8 K for the GB region to be superconducting. The Josephson junction model[52] is thus a good description of the conduction through the region in most experiments above this temperature as it can be thought of as superconducting bulk with sandwich layers of GB-regions between.

5.6 Conclusion

The GB interaction distance of 25 Å in both Au and Nb_3Sn gives a lower bound to the size of nanocrystals before they no longer contain any bulk-like material due to the overlap of GBs. Below this size, the grains will be entirely made of amorphous regions with material that is quite unlike the bulk.

The grain boundaries in gold are observed to have relatively little effect on the density of states at the Fermi energy. In this respect, it is not likely that these boundaries contribute much to resistivity in the material. The simplest grain boundaries are high angle and are of high formation energy. As the mismatch angle decreases for the CSL grain boundaries, the energy decreases as they are further separated. There is negligible change in this

material as the density of states is effectively constant in a large region around the Fermi energy. This is likely to be the case with grain boundaries in any material with a featureless DOS in this region. These GBs may be plentiful, but are of little interest in the dynamics of the material.

Nb_3Sn displays a much richer structure in the density of states around the Fermi level, with the Fermi energy actually lying on a peak. As it is much easier for a change to occur in the DOS by shifting some of the states in energy, $n(\epsilon_f)$ is more sensitive to changes in the atomic structure. The decrease observed in the DOS is thus large even with the simple grain boundaries studied and will lead to a large drop in carrier concentrations in GB regions. These regions were found to actually extend much further into the material than would be suggested by the atomic relaxations, which were only significant in the atoms close to the interface. The electronic structure perturbations are much longer in range and can extend multiple unit cells into the crystal. The drop in the density of states means that this region may be in the normal state when the bulk is superconducting at liquid He temperatures.

Considerable differences are seen for grain boundaries which would fall into the same classification in the CSL model and this obviously raises issues with the use of this model to group the electronic structure effects of grain boundaries. In this material, grain boundaries are found to create large resistive regions, and can thus be used to increase the upper critical field. Due to the large drop in $n(\epsilon_f)$ in the disordered regions, they are a prime candidate to be modelled as Josephson junctions.

Chapter 6

Nb Low Temperature Phase

6.1 Introduction

Niobium metal is a common superconductor, having the highest critical temperature of any elemental material at standard pressure. It is easy to work with, being malleable and ductile. It is also a component in many of the high field magnetic compounds used commercially, Nb_3Sn and Nb_3Ge.

The structure of the ground state atomic positions in the pure metal Nb have been measured multiple times[53][54][55], and found to be body-centred cubic (bcc) at and above room temperature.

Recent experimental work by Bollinger et al.[56] has observed a structural distortion forming between the different crystal axes in single crystal Nb upon cooling from 300 K. Their work shows the linear thermal expansion is different along all 3 crystallographic axes and that this is incommensurate with the material being cubic. Knowledge of the actual crystal structure is important to our understanding of superconductivity as Nb is the element with the highest superconducting transition temperature at room pressure and thought to be a standard BCS superconductor and thus should be a

good theoretical test of calculating electron-phonon coupling.

This work examines the 'ideal' bcc Nb structure for instabilities through the use of both ground state density function theory(DFT) and density functional perturbation theory(DFPT) to examine whether there is a lower energy structure and if the bcc structure is dynamically unstable at low temperatures.

6.2 Method

The primitive unit cell of Nb was created with lattice parameters taken from experimental values in the literature[54]. This was then allowed to relax to the lowest energy state with symmetry imposed, restricting the lattice angles to that of the bcc primitive unit cell, and only the length $a = b = c$ allowed to change. This was performed with a $40 \times 40 \times 40$ MP grid across the Brillouin zone and a 700 eV cut-off energy to observe small energy changes of the order of 10 meV.

A DFPT calculation was performed using the Baroni method[57] to examine if this structure should be stable. This was performed at a sampling of $12 \times 12 \times 12$ points across the Brillouin zone which should take into account interactions between atoms up to 34 Å apart. The dynamical matrices were Fourier interpolated to produce dispersion curves for the structure along high symmetry directions and also a phonon density of states was produced.

The geometry of a primitive cell was then relaxed from a symmetry broken initial position with no symmetry enforced with the same sampling and cut-off energies. This was analysed to find the symmetry group of the resulting structure.

A DFPT calculation was performed on this new structure to test for stability with the same Brillouin zone sampling as the unit cell had not changed

drastically in any dimension. A phonon dispersion curve was produced along the same directions as with the bcc unit cell.

6.3 Results

The lattice parameters and total energies for both structures are shown in table 6.1. The structures are very similar, with very small adjustments to the individual lattice parameters between them. The total energy is lowered by 73.86 meV/atom by this phase change which is of the order of the thermal energy KT at the transition temperature of 25.85 meV.

	bcc	Rh
a=b(Å)	2.85	2.79
c(Å)		3.04
$\alpha = \beta$	109.47°	111.30°
γ		107.58°
Energy (eV/atom)	-142.34337	-142.41724
Volume(Å^3)	17.80	17.73

Table 6.1: Comparison of the body-centered cubic and rhombohedral structures of Nb. Duplicate values are omitted for the cubic structure where the lattice parameters are equivalent.

The phonon dispersion curve for the body-centred cubic form of Nb is shown in figure 6.1. It can be seen that there is an imaginary phonon mode between Γ and H$(\frac{1}{2}, -\frac{1}{2}, \frac{1}{2})$. This indicates that the structure is dynamically unstable with respect to atomic motion commensurate with this wavevector. The fact that the frequency goes to zero at the gamma point is an artefact of the imposed symmetries and the enforcement of the accoustic sum rule which is unavoidable without extremely high BZ sampling.

The phonon dispersion for the fully relaxed rhombohedral structure (space group $R\bar{3}M$) is shown in figure 6.2. The general shape of the dispersion is similar with a few notable differences. The unstable phonon mode

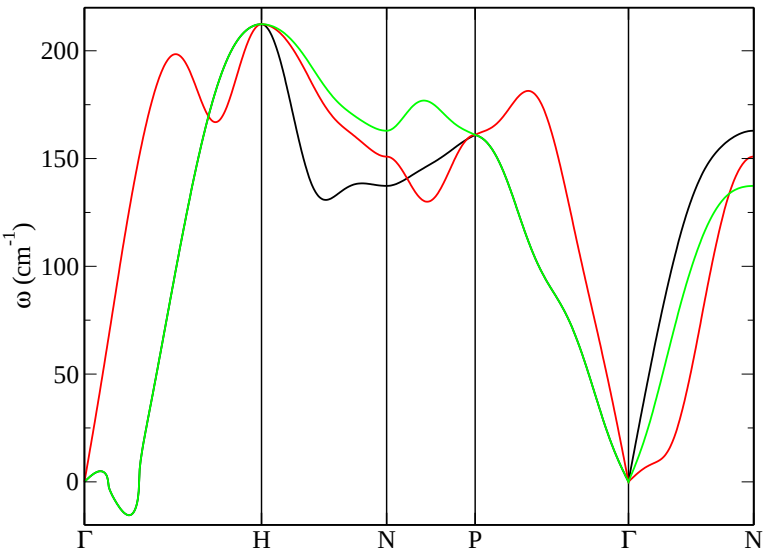

Figure 6.1: Phonon dispersion curves for the bcc-form of Nb. It was calculated with an energy cut-off of 700 eV and a Brillouin zone sampling grid of $40 \times 40 \times 40$. Negative phonon frequencies are used to indicate imaginary phonon modes.

does not occur in the rhombohedral structure which indicates that it is dynamically stable within the harmonic approximation.

Several of the bands which crossed in the bcc phase, have now become avoided crossings due to the reduction in the symmetry. Finally, the frequency of the highest phonon mode is approximately 10% higher in the rhombohedral phase than in the bcc phase.

The density of states for both structures is shown in figure 6.3. It can be seen that the frequencies of most of the modes are higher in the rhombohedral structure. The large peaks have been broken into broader sub peaks of much smaller amplitude.

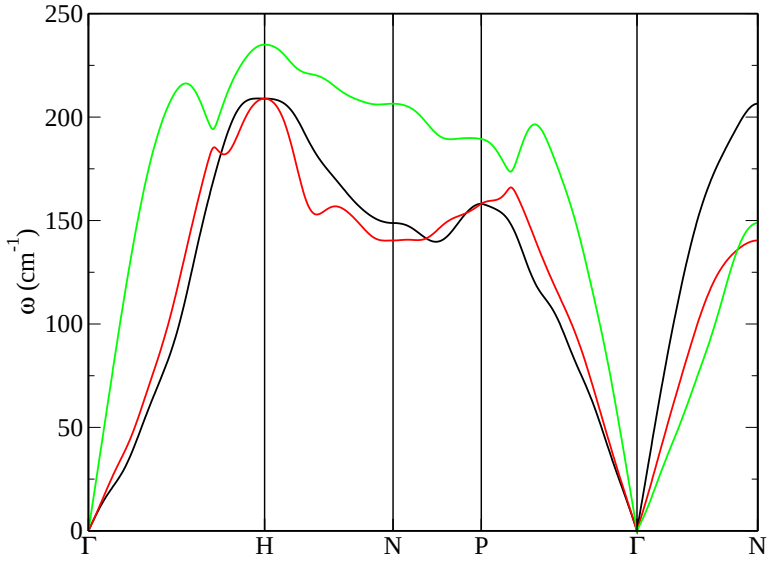

Figure 6.2: Phonon dispersion curves for the relaxed low temperature structure of Nb. The special points used the same points from the bcc structure. It was calculated with an energy cut-off of 700 eV and a Brillouin zone sampling grid of $40 \times 40 \times 40$.

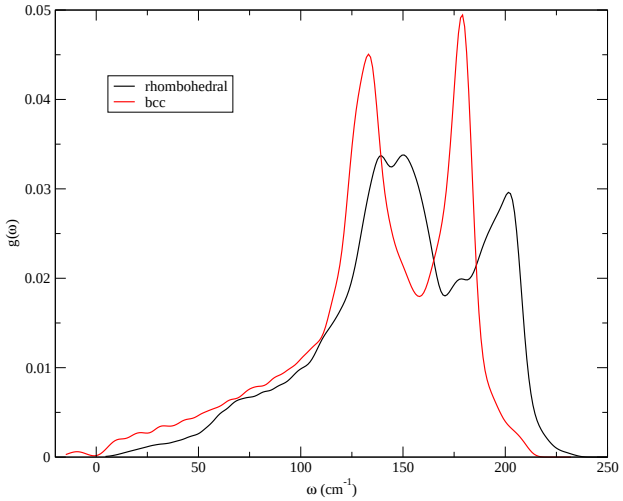

Figure 6.3: The phonon density of states of both bcc and rhombohedral($R\bar{3}M$) structures of Nb. These were sampled at wavevectors on a $40 \times 40 \times 40$ grid in the Brillouin zone. Negative phonon frequencies indicate modes which are unstable.

6.4 Discussion

The imaginary phonon mode for the bcc structure shows that it must be unstable at 0 K. That it is only unstable in a few small symmetry-related regions of the Brillouin zone shows that there is a preferred low energy structure that any small perturbation will cause it to fall into.

The resulting rhombohedral structure is reached by only a slight change in lattice parameters, and this is commensurate with a martensitic or diffusionless transition as the number of atoms in each unit cell remains constant.

As the degeneracy of the bcc structure is broken, it is natural for the peaks in the phonon DOS to broaden and thus some are pushed to higher energies. In particular the highest phonon branch is now broken away from the other phonon modes by broken degeneracies at the symmetry points and avoided crossings elsewhere.

The rhombohedral structure is very slightly more dense than the bcc structure and this may account for the higher phonon frequencies as the atoms repel each other more strongly.

Ignoring the imaginary modes, the phononic contribution to the electron-phonon coupling in the bcc structure appears to be much higher as the phonon density of states is higher at low frequency. This change would almost certainly lead to an incorrect calculation of superconducting parameters from the bcc phase.

6.5 Conclusion

Nb metal appears to undergo a phase change at low temperatures to a rhombohedral phase. The transition is found to be martensitic and only involves very slight changes to the bcc primitive cell. The phase change would be

spontaneous as the structure is not stable with respect to perturbations along the (1,-1,1) direction. This rhombohedral phase is calculated to be stable to 2^{nd} order in energy as there are no imaginary phonon frequencies and the unconstrained forces are zero.

Further work is needed to understand why the structure becomes bcc at higher temperatures as simple entropic arguments would suggest that the state with lower symmetry would be thermodynamically favourable.

Chapter 7

Electron-Phonon Coupling in Simple Metals

The ability to calculate the electron-phonon coupling for a material can tell us a lot about macroscopic properties. Some of the most easily observable macroscopic properties, thermal and electrical conductivity, can be extracted from the interaction of the electrons and phonons. We can also link the interaction to superconducting theories through the Eliashberg spectral function[17].

The aim of this chapter is to calculate the electron-phonon interaction for the case of simple materials. For materials to be BCS superconductors, there must be the possibility of electron scattering occurring. This means that there must be some partially filled bands as the energy change in scattering is very small, on the order of KT. The only materials at 0 K that this can occur in are, by definition, metals. It would be possible to look at semiconductors where the transitions can only occur between maxima or minima in the valence and conduction bands using the methods set out earlier but here we will restrict ourselves to the superconducting properties

of materials, and so we will study metallic elements.

The simple materials also provide a useful test of the electron-phonon calculations as they have a small number of valence electrons in the unit cell. The main aim of this chapter is to calculate the superconducting transition temperatures of some simple metallic elements: Au, Nb, Mo and Zr.

7.1 Calculation of the Eliashberg Spectral Function

The Eliashberg spectral function is the central quantity which quantifies the strength of the electron-phonon coupling as a function of phonon frequency. It is defined as

$$\alpha^2F(\omega) = \frac{1}{N_f}\sum_{\mathbf{q},j}\sum_{\mathbf{k},i,i'}|g^{\mathbf{g},j}_{\mathbf{k},i,\mathbf{k+q},i'}|^2\delta(\epsilon_f-\epsilon_{\mathbf{k},i})\delta(\epsilon_f-\epsilon_{\mathbf{k+q},i'})\delta(\hbar\omega-\hbar\omega_{\mathbf{q},j}), \tag{7.1}$$

where $g^{\mathbf{g},j}_{\mathbf{k},i,\mathbf{k+q},i'}$ is the electron-phonon matrix element for scattering from a state $\mathbf{k}$ to a state $\mathbf{k+q}$, ϵ_f and N_f are the Fermi energy and DOS, $\epsilon_{\mathbf{k},i}$ is the energy of a KS state at $\mathbf{k}$ with index i, and $\omega_{\mathbf{q},j}$ is the frequency of a phonon of wavevector $\mathbf{q}$ and branch index j. It is a weighted sum of the matrix elements which includes only those whose initial and final states which lie on the Fermi surface.

It is linked to several macroscopic quantities through the Boltzmann transport equation, namely the thermal and electrical conductivity. It also governs the superconducting transition temperature through either the McMillan equation[58] for strong coupling or the full Eliashberg superconductivity equations[17]. It is therefore a very useful quantity to be able to calculate and is given directly from the matrix elements and the phonon modes. The electron-phonon coupling constant is defined in terms of the Eliashberg

spectral function as

$$\lambda = 2 \int \frac{\alpha^2 F(\omega)}{\omega} d\omega. \tag{7.2}$$

To construct the spectral function, we can use a similar method to that used for producing density of states from the electronic eigenvalues at discrete points. In the case of the DOS, we require a continuous function that is built from discrete samples (energy eigenvalues in the Brillouin zone) that should represent the continuous nature of the real Brillouin zone. We represent each discrete sample by a normalized Gaussian function which should represent both the point but also those in the locality of the point.

The Eliashberg spectral function is built in almost exactly the same way, except that the delta functions(and so Gaussian) should have an integral equal to the norm of the electron-phonon matrix element, given in equation 2.55, at the corresponding frequency for that phonon wavevector.

Now doing this directly for phonon calculations leads to anomalous results. Some phonon modes at low frequencies are under represented, and the factor of $\frac{1}{\omega}$ in equation 7.2 exacerbates the situation. For any material, as the frequency goes to zero, the spectral function should also go to zero at least as quickly as linearly. If this is not the case, the integrals for the coupling constants go to infinity as they are weighted with a further factor of $\frac{1}{\omega}$. Thus any problems in the low frequency regions will make the calculation more inaccurate than in the higher frequencies.

7.1.1 Splitting the Eliashberg Spectral Function

The solution to this is to separate the spectral function into two parts – the phononic part, $F(\omega)$ which is the density of states of phonons linking points on the Fermi surface, and coupling strength part, $\alpha^2(\omega)$ which is the squared modulus of the EP matrix elements as a function of frequency.

The electron-phonon coupling, α^2F can be written as the product of two parts,

$$\alpha^2F(\omega) = \alpha^2(\omega)F(\omega) \tag{7.3}$$

where the phononic spectral part, $F(\omega)$ is defined as,

$$F(\omega) = \frac{1}{N_0}\sum_{\mathbf{k},\mathbf{q}} \delta(\epsilon_{\mathbf{k}} - \epsilon_f)\delta(\epsilon_{\mathbf{k}+\mathbf{q}} - \epsilon_f)\delta(\hbar\omega - \hbar\omega_{\mathbf{q}}) \tag{7.4}$$

The electron-phonon coupling part, $\alpha^2(\omega)$, can be approximated from the electron-phonon coupling elements. The number of phonon wavevectors linking points on the Fermi surface is proportional to the number of pairs of elements that can be made, which is proportional to N_0^2, the density of states on the Fermi surface. The density of states on the Fermi surface, N_0 is proportional to $F(\omega)$, so we can define a normalised spectral function $\tilde{F}(\omega)$ by,

$$F(\omega) = N_0\tilde{F}(\omega). \tag{7.5}$$

The phononic part, $F(\omega)$, is found using interpolation of a very fine sampling of the Fermi surface to get the correct low frequency behaviour with a large number of phonon wavevectors across the frequency range. This produces the correct low frequency behaviour that the DOS should be quadratic at low energies.

To find the coupling strength part, we cannot use interpolation so we must do a limited number of samples across the frequency range. These values are assigned into bins of 50 samples and the average of the samples in the region is taken as the value of $\alpha^2(\omega)$ at the centre of the region. This is shown in figure 7.1 for Nb along with a piecewise cubic spline used as an interpolation function to avoid discontinuities. Frequencies above or below

the measured range are assumed to have the same coupling strength as the lowest and highest frequency bins.

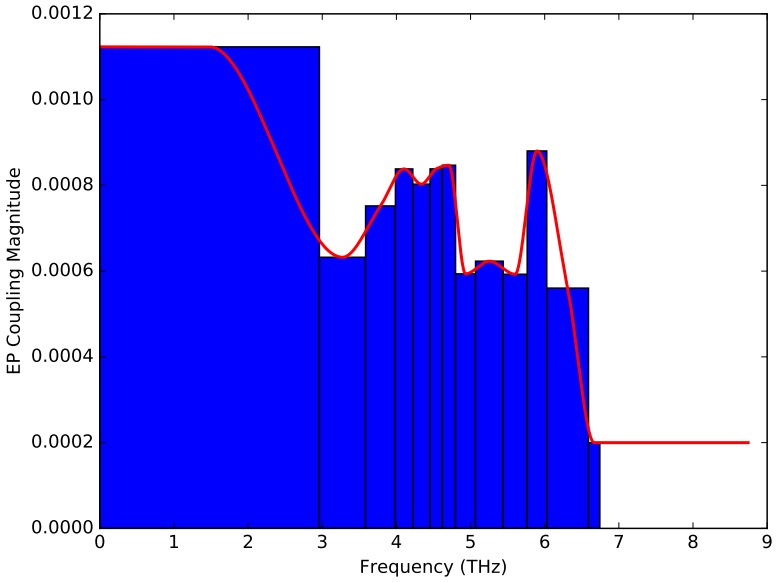

Figure 7.1: Demonstration of the interpolation of the EP coupling strength as a function of frequency. The bins show the average EP matrix element magnitude across 200 sample points.

These quantities are then simply multiplied at each value of ω. Piecewise-cubic interpolation is used between the values for $\alpha^2(\omega)$ so as to avoid discontinuities in the spectral function. An example of the final result for Nb is given in figure 7.11. As can be seen, there are no spurious peaks at low frequencies and the low frequency behaviour has the correct quadratic form and so a finite value for the electron-phonon coupling constant.

7.2 Modified McMillan Transition Temperature

With knowledge of the Eliashberg spectral function, we can find the electron-phonon coupling constant, λ, from equation 7.2. This is related to the super-

conducting transition temperature by the McMillan transition temperature formula[58], modified by Allen and Dynes[59],

$$k_B T_c = \frac{\hbar\omega_0}{1.20} \exp\left[-\frac{1.04(1+\lambda)}{\lambda - \mu^*(1+0.62\lambda)}\right], \tag{7.6}$$

where ω_0 is a measure of the average phonon energy given by

$$\omega_0 = \omega_{\text{ref}} \exp\left[\frac{2}{\lambda}\int \frac{d\omega}{\omega}\alpha^2 F(\omega)\ln(\frac{\omega}{\omega_{\text{ref}}})\right], \tag{7.7}$$

and μ^* is the effect of Coulomb repulsion on this interaction, referred to as the "Coulomb pseudopotential," and ω_{ref} is a reference frequency. The phonon frequency measure, ω_0, is calculated directly using equation 7.7 and then substituted into equation 7.6. The reference frequency, ω_{ref}, is an arbitrary value that determines a unit frequency. For example, if the reference frequency is chosen to be 1 Hz, the resulting ω_0 will also be in hertz and this is the simplest choice as the resulting transition temperature will be in kelvin. Alternatively, the equations may be solved in atomic units, and ω_{ref} and ω_0 would be in units of $E_H/\hbar$ where E_H is the Hartree energy. The constants $\hbar$ and k_B in equation 7.6 must be in the same units as this reference frequency for the equations to be consistent. For this work, we have used a reference frequency of $\omega_{\text{ref}} = 1$ Hz for the simplicity of working in SI units on these macroscopic properties.

The μ^* term effectively wraps up the entirety of the screened long-range electron-electron repulsion in superconductivity, which tends to depress the transition temperature. Experimentally, this term is found by inverting the McMillan equation using experimental values of the transition temperature and EP coupling parameter. It can be shown to be small (and with a value in the region 0.10-0.14) as long as the effective expansion parameter in

Eliashberg theory, $\frac{\lambda\omega_p h}{E_e l}$ is smal[60]. In theory, it can be found by performing an average cross the Fermi surface of the GW[61] corrections to the single particle Kohn-Sham equations and rescaling this to the the length scales of phonon interactions[61], but the evaluation of this is very computationally expensive and beyond the scope of this project.

The numeric factors in the McMillan equation come from the numerical solution of the Eliashberg equations which are a set of coupled equations that can be solved self-consistently to obtain information about the superconducting state in a material. These are complicated and require many iterations to achieve convergence[59], and so it is much more convenient to use this approximation.

Thus with knowledge of the Eliashberg spectral function, we have all the tools needed to compute the superconducting transition temperature.

7.3 Materials Studied

Au forms a face-centred cubic solid at room temperatures and below. It does not become superconducting at any temperature which it is currently possible to attain. Nb is conventionally thought to be body-centred cubic solid which becomes superconducting at 9.25 K but as shown in the previous chapter, is found to convert to a rhombohedral form at low temperatures in agreement with recent experimental measurements[56]. Mo and Zr are elemental superconductors with similar numbers of electrons to Nb but with much lower transition temperatures. This is shown in table 7.1

Material	T_c (K)
Au	0
Nb	9.25
Mo	0.92
Zr	0.61

Table 7.1: Experimental[62] superconducting transition temperatures for the materials studied.

7.4 Method

The unit cell of each material was created using experimental data as a starting point. They were then tested for ground state convergence by increasing the cut-off energy and the Brillouin zone sampling so that the relative change was less than 0.01eV. The exchange-correlation functional used was PBE.

Next, each had its unit cell and atomic positions relaxed, using the atomic forces, to find the lowest energy configuration. The convergence criteria was that the stresses on the unit cell had to be below 0.01 GPa so that the atoms were very close to their equilibrium positions.

A band structure and density of states calculation was performed across the Brillouin zone to measure the density of states at the Fermi energy, and to give insight into the location of bands involved in scattering at the Fermi energy. OptaDOS[63] was used to improve the accuracy of the DOS plots by including information about the KS band energy gradients into the width of the Gaussian functions which form the DOS.

A linear response calculation was performed to calculate the phonon spectrum at a regular array of points across the Brillouin zone, as well as to find the Γ point dynamical matrix for the acoustic sum rule to be enforced. These perturbative calculations were performed at q-points on a MP grid that had been shifted to include the Γ-point as this has been found to improve the quality of interpolation as it necessarily includes the

static forces. The phonon frequencies were then combined with the list of Fermi surface points to interpolate an accurate approximation of the phonon spectral function $F(\omega)$.

An electron-phonon calculation was then performed using the algorithm explained in the previous chapters. This was performed for 500 possible q-vectors which linked points on the Fermi surface. This value was chosen as it converged the spectral function for Au to within 5%.

The results from this were then interpolated to find the strength of the electron-phonon coupling strength, $\alpha^2(\omega)$ across the range of frequencies. This was then multiplied by the phonon spectral function to get the Eliashberg spectral function, $\alpha^2 F(\omega)$.

7.5 Results

7.5.1 Structure

The relaxed geometry structures along with experimental data from the ICSD are shown in table 7.2 where possible. The cubic structures are all slightly larger than the experimental values but by less than 0.1 Å.

Material	Structure	Calculated (Å)		Experimental (Å)	
		a	c	a	c
Au	fcc	4.132		4.09[64]	
Nb	rhom	3.350		–	
Mo	bcc	3.176		3.1472[65]	
Zr	hexagonal	3.142	5.202	3.23[66]	5.14[66]

Table 7.2: The relaxed structures of the simple metals studied compared with experimental results taken from the ICSD. The lattice constant b is equal to a in all of these structures and c is omitted for cubic structures where it is fixed by symmetry.

Zr has a hexagonal unit cell with a lower symmetry than the other materials and thus has two degrees of freedom. For this material, the relaxed unit

cell was slightly taller and thinner than the experimental result, although both are within 0.1 Å.

7.5.2 Electronic Properties

The band structure for Au shows localized d-type bands lying just below the Fermi energy. The only bands present at the Fermi energy are of an s-type and so the corresponding density of states is relatively flat as these bands tend to be relatively delocalised. It is also quite low as there is only a single band crossing the Fermi energy, leading to only one Fermi surface band.

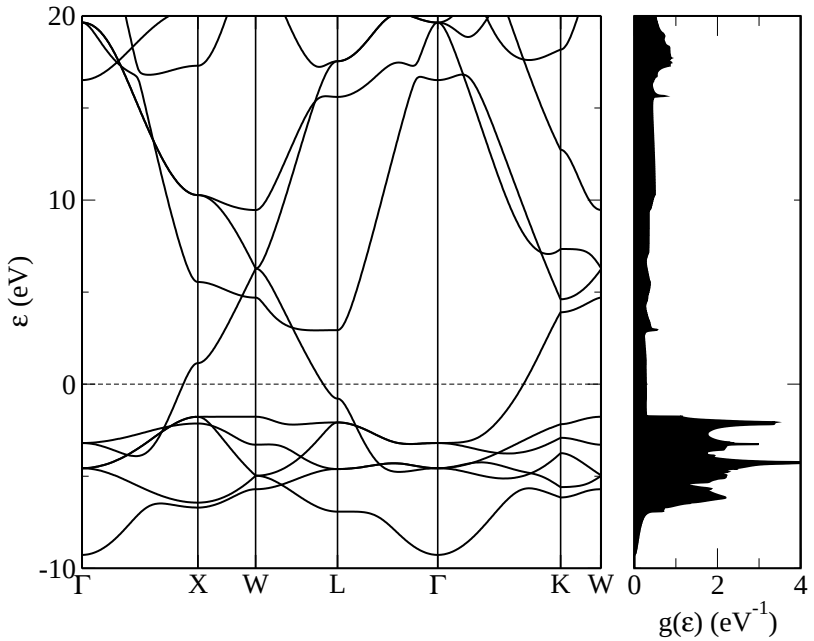

Figure 7.2: The electronic band structure and density of states for Au. The DOS was sampled on a grid of $50 \times 50 \times 50$. The band structure was sampled on points that were a maximum of 0.01 Å apart.

In contrast to Au, the other elements (Zr, Nb and Mo) all have a Fermi energy that lies within the flat localized bands of the d-subshell. This gives a higher $n(\epsilon_f)$ for these materials.

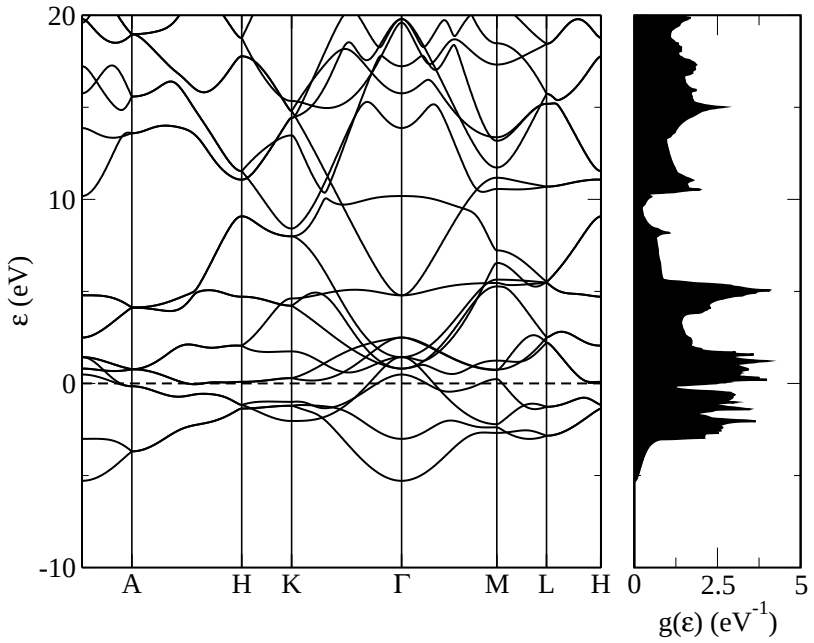

Figure 7.3: The electronic band structure and density of states for Zr. The density of states was sampled on a grid of $50 \times 50 \times 50$. The band structure was sampled on points that were a maximum of 0.01 Å apart.

Zr has a Fermi energy that lies almost exactly on a peak in the DOS. There are also a large number of bands which cross the Fermi energy which will give rise to a large number of scattering areas in the Brillouin zone.

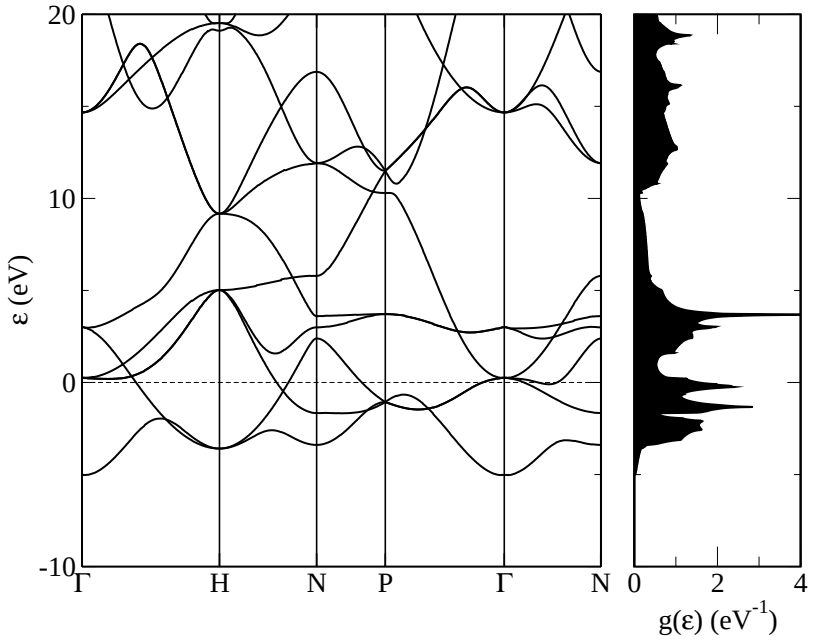

Figure 7.4: The electronic band structure and density of states for Nb. The density of states was sampled on a grid of $50 \times 50 \times 50$. The band structure was sampled on points that were a maximum of 0.01 Å apart.

The Fermi energy in Nb again lies almost exactly on a peak. There are multiple bands crossing the Fermi energy in the region from H to N which correspond to two nearby sheets of Fermi surface. Furthermore, the bands are much more dense around the Fermi energy and this leads to a higher density of states here.

The electronic structure and density of states in Mo are very similar to that of Nb but the states are pushed slightly down in energy relative to the Fermi energy and it now lies between two regions of high DOS. However, the density of states is still much larger than in the s-band regions of the

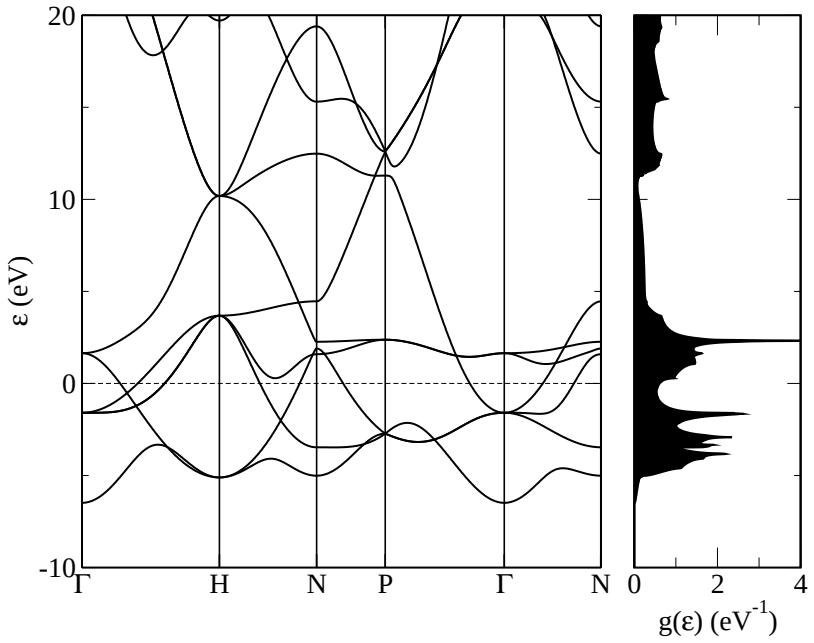

Figure 7.5: The electronic band structure and density of states for Mo. The density of states was sampled on a grid of $50 \times 50 \times 50$. The band structure was sample on points that were a maximum of 0.01 Å apart.

DOS.

The Fermi energy density of states values are given in table 7.3, showing the DOS at the Fermi energy in Au, and to some extent Mo, being much lower than the other materials.

Material	$n(\epsilon_f)(\mathrm{eV}^{-1})$
Au	0.2797
Zr	2.3893
Nb	2.234
Mo	0.6113

Table 7.3: The density of states at the Fermi energy for the materials studied. The values were measured from the density of states graphs.

7.5.3 Phonon DOS

The phonon density of states for Au is shown in figure 7.6. The band frequencies are linear with respect to distance from the zone centre across a large region of the Brillouin zone which gives a quadratically increasing phonon DOS.

In figure 7.7, the phonon branches of Nb are shown to peak at a slightly higher frequency than in Au, although the overall phonon DOS is similar. The degeneracy of the phonon branches is broken by the rhombohedral distortion and there are some avoided crossings along the high symmetry directions. The bulk of the phonon DOS is above 100 $^{-1}$, but the contribution at low frequencies is not insignificant. There is a slight bending of the phonon branches along the Γ to H symmetry line which leads to the DOS being linear in this region.

The phonon branches in Mo, figure 7.8 vary rapidly with the distance to the Γ point. This indicates a high speed of sound in the material. These branches lead again to an approximately quadratic variation in the phonon

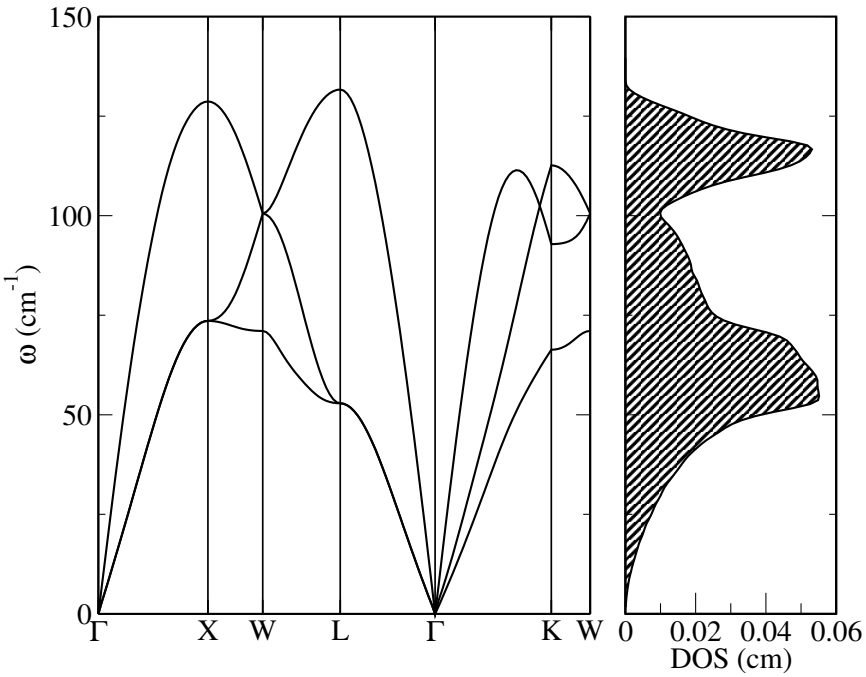

Figure 7.6: The phonon dispersion and density of states for Au. DFPT calculations were computed for phonon wavevectors on a $9 \times 9 \times 9$ grid across the Brillouin zone and interpolated to find the dispersion and DOS.

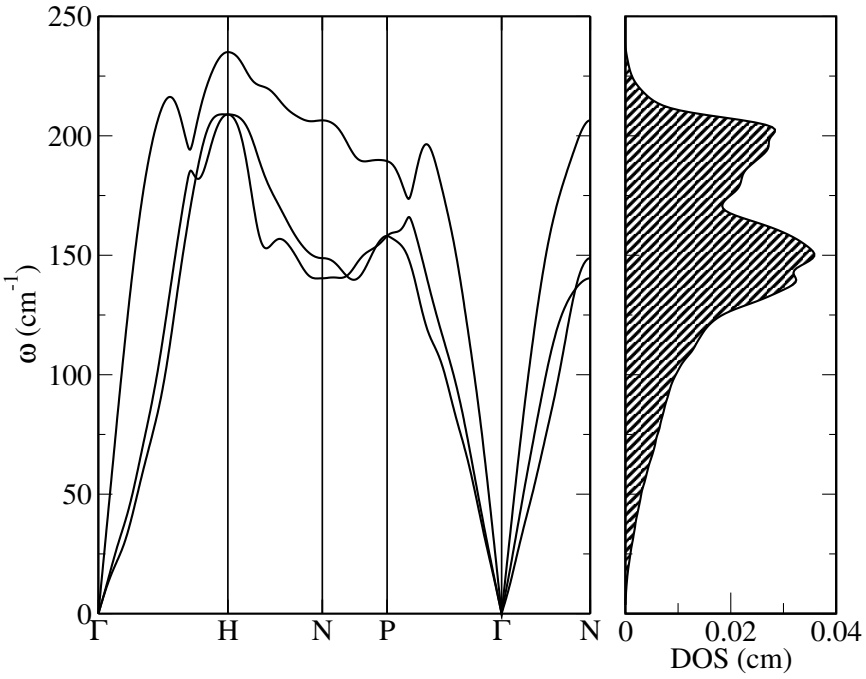

Figure 7.7: The phonon dispersion and density of states for Nb. DFPT calculations were computed for phonon wavevectors on a $12 \times 12 \times 12$ origin-shifted grid across the Brillouin zone and interpolated to find the dispersion and DOS.

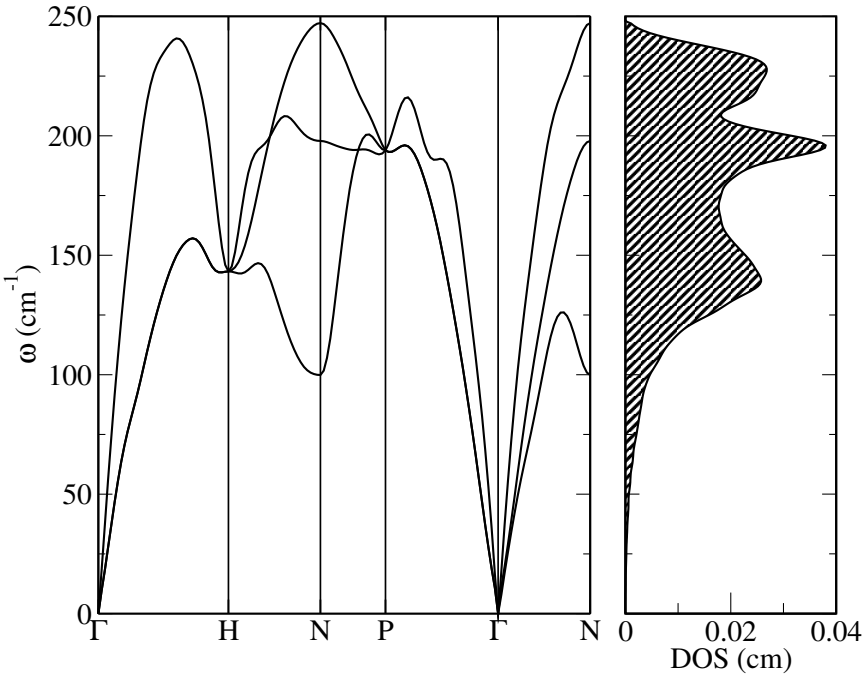

Figure 7.8: The phonon dispersion and density of states for Mo. DFPT calculations were computed for phonon wavevectors on a $10 \times 10 \times 10$ origin-shifted grid across the Brillouin zone and interpolated to find the dispersion and DOS.

density of states at low energy, but the density of states is much smaller than in comparison with Au. The majority of the DOS is between 100 cm^{-1} and 250 cm^{-1}.

Figure 7.9 shows the phonon spectrum for α-Zr which has two atoms per unit cell and hence 6 phonon branches which give a higher phonon DOS than in the other materials. The branches also have a more complicated structure with more low frequency modes. but half of these do not go below 25 cm^{-1}. These are in agreement with previous experimental and theoretical results[67]. The minimum at 30 cm^{-1} is caused by sheets of Zr sliding in opposite directions, and this has a lower energy when the whole sheet is in phase. The highest energy mode is when the sheets vibrate towards each other.

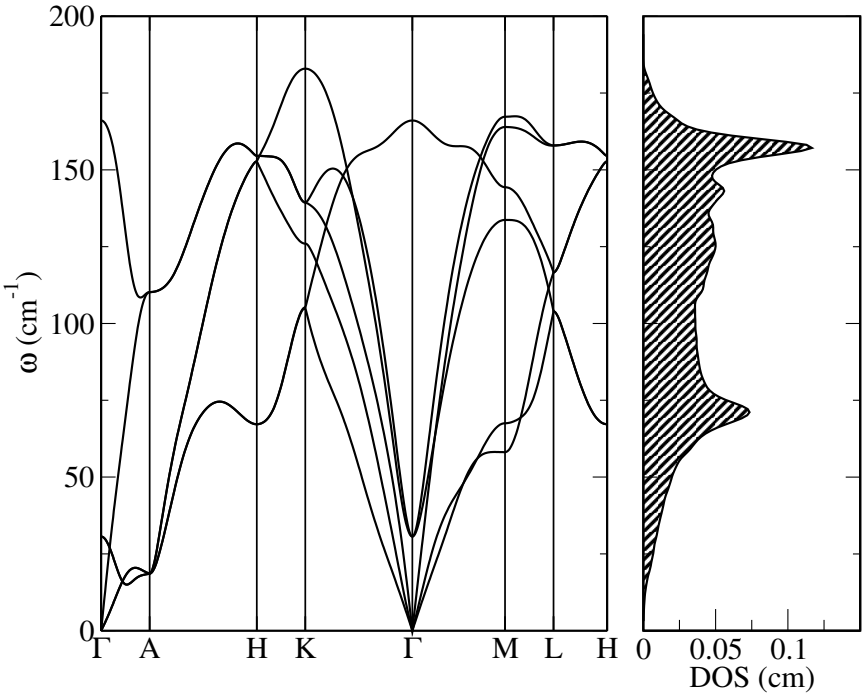

Figure 7.9: The phonon dispersion and density of states for Zr. DFPT calculations were computed for phonon wavevectors on a $24 \times 24 \times 20$ origin-shifted grid across the Brillouin zone and interpolated to find the dispersion and DOS.

7.5.4 Spectral Function and Superconducting Transition Temperature

The spectral function in Au, figure 7.10 shows a marked difference to the phonon DOS. The peak at lower frequency is enhanced by the electron-phonon coupling. The electron-phonon coupling is weak across the entire frequency range, due to the low number of partially occupied states. This leads to the Eliashberg spectral function being low.

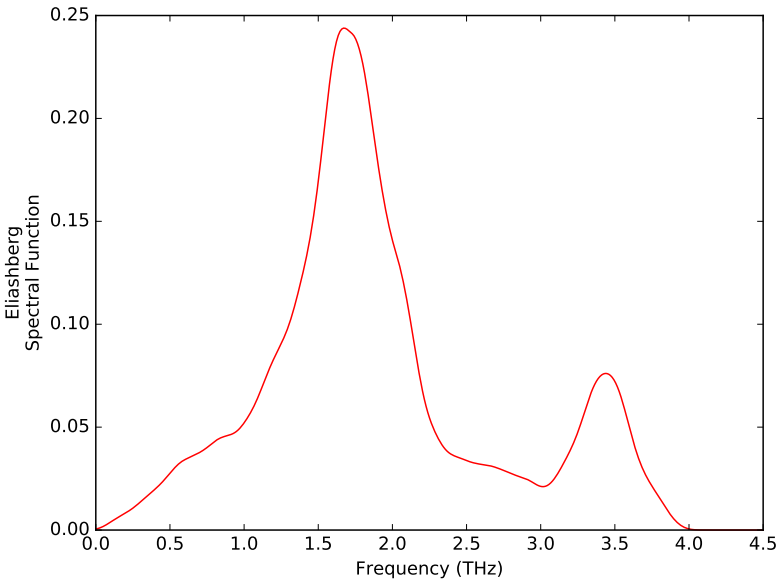

Figure 7.10: The Eliashberg spectral function for Au.

The Eliashberg spectral function for Nb, figure 7.11, again shows a large difference between the phonon DOS and the spectral function. The function rises more quickly to a plateau at 2 THz which is causes by the EP coupling being stronger at low frequencies. The coupling strength is found to be higher than the other materials at low frequency which are of greater importance in calculating λ.

The Eliashberg spectral function for Mo, figure 7.12 is similar to the DOS in all but magnitude. This indicates that the strength of the coupling

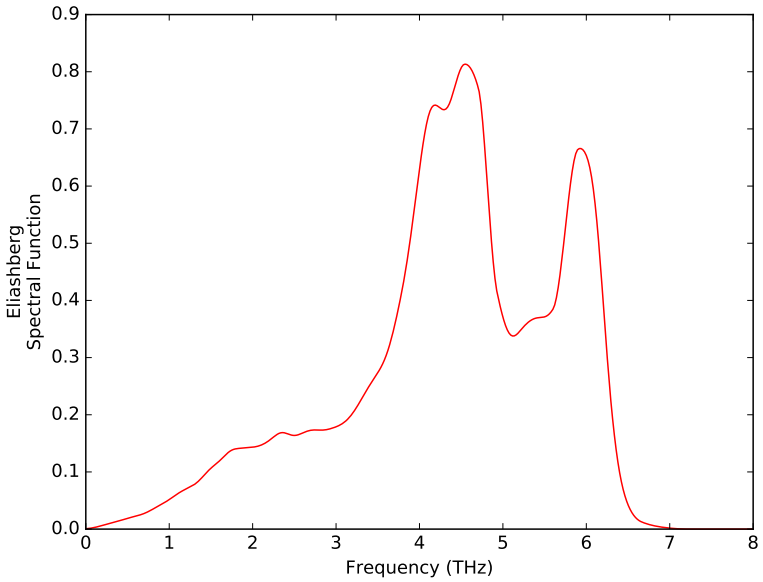

Figure 7.11: The Eliashberg spectral function for Nb.

(α^2) is almost constant across the frequency range. The same triple peaked structure is obtained and the strength of the coupling tends rapidly to 0 below 1 THz.

Finally, the spectral function for Zr is shown in figure 7.13. Although the spectral function is of lower magnitude than both Nb and Mo, the low frequency peak at 2 THz is enhanced by the EP coupling and the higher frequency peak is diminished. As in Nb, a plateau is formed at approximately 1 THz.

The calculated values for λ using equation 2.57 are shown in table 7.4 along with the estimated superconducting transition temperatures calculated using the modified McMillan formula (equation 7.6) and these are compared with experimental values.

Au, which is not found experimentally to be superconducting, has a low EP coupling constant. This is consistent with its high temperature

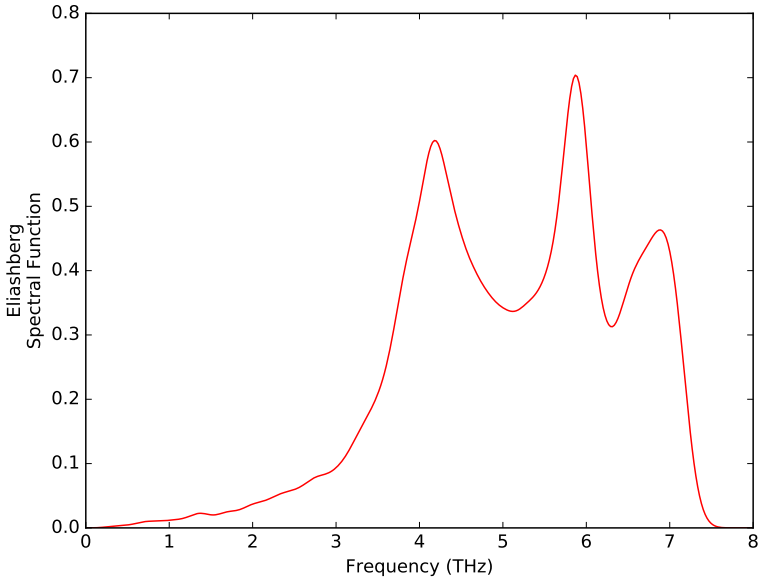

Figure 7.12: The Eliashberg spectral function for Mo.

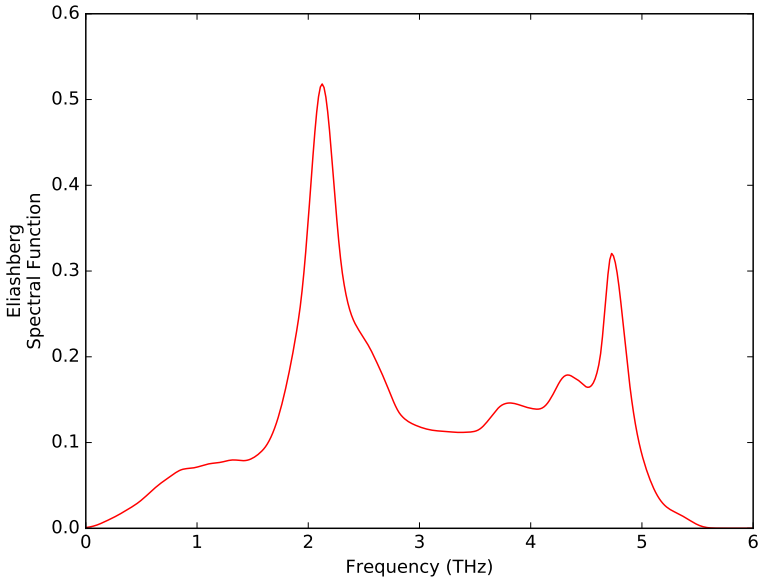

Figure 7.13: The Eliashberg spectral function for Zr.

Material	Calculated λ	Experimental λ	Calculated T_c (K)	Experimental T_c (K)
Au	0.18	0.15	0.00	0
Nb	1.05	0.82	16.4	9.25
Mo	0.38	0.41	0.80	0.92
Zr	0.34	0.41	0.11	0.61

Table 7.4: Calculated values of the electron-phonon coupling constant. Calculated values of the superconducting transition temperatures from the McMillan weak coupling equation are also shown. These T_c values were calculated with a coulomb repulsion constant, μ^*, of 0.11. Experimental values are also shown for comparison[62].

coefficient of resistance compared with the other materials studied. The low coupling causes the superconducting transition temperature to be found to be extremely low, although the McMillan coupling formula is parameterised for strong coupling and so it is not accurate here. Nonetheless, the very small coupling strength will cause superconductivity to be very weak in this material.

The EP coupling constants for the superconducting materials (Nb, Mo, Zr) are found to be 7-28% different from the experimental values which were found by inverting the McMillan equation. The result for Nb is close to the experimental λ from electron tunnelling measurements[68] (1.05), but this data is not available for the other elements. Calculations using the LDA exchange-correlation functional have shown values as high as 1.23[69] for the electron-phonon coupling in Nb.

The superconducting temperatures were derived from the modified McMillan equation. The values are close to the experimental values but due to the exponential, small errors are magnified. The estimates for the low coupling T_c values can also be shifted by changing the value for the Coulomb pseudopotential, μ^*, which is effectively a free parameter in these calculations and higher values of this parameter decrease the transition temperature. The chosen value of 0.11 is consistent with the range estimated in the liter-

ature for these materials (0.10 to 0.15), but the transition temperature can vary in this range; ie for Nb, T_c dropped by 50% with a μ^* of 0.15.

7.6 Discussion

7.6.1 Structure

The structures of Au, Nb and Mo show the classic GGA effect of underbonding and the lattice constants are all larger than the experimental values. As these structures have only one free parameter and the atoms are equivalent, this is the only effect that can be observed.

The hexagonal structure of Zr shows a bigger deviation from the experimental values, although they do attempt to preserve the volume of the unit cell. It is known that local XC functionals are not particularly good at describing highly localized electrons and so these states may be more dispersed within the unit cell and will affect the bonding, especially when it is in an efficient packing state such as these.

7.6.2 Electronic Properties

The flat s-band energy levels in Au and similar metals are parabolic and so give a flat DOS over a large region. Although this means that the Fermi energy DOS does not vary much due to the presence of sparse defects (as shifts in the Fermi energy do not change the carrier concentrations), they tend to have low carrier concentrations and do not make particularly good superconductors.

The fact that the Fermi energy in Zr, Nb and Mo happens to lie on a region of high DOS is not completely surprising. If the Fermi energy were to lie anywhere in the d-subshell region, one would expect it to lie in a region

of high density of states. In a metal, the Fermi energy has to be on a state, and as these energy regions have a high number of states, this is where we expect to find the Fermi energy. One would expect these materials to be good superconductors due to the large number of partially filled states, which increase the number of electrons that can be scattered by phonons and ultimately increases the electron-phonon coupling in the material, but the coupling strength also depends on their crystal structure as this generates the phonon modes.

7.6.3 Phonon Properties

The phonon spectra are calculated to be of lower frequency than experimentally observed. This is likely due to the slightly longer GGA bond lengths which will affect the curvature of the nuclear energy wells. With the atoms spaced further apart, there is likely a more shallow energy basin around the ground state position which decreases the energy of the phonon modes. It is currently unclear on the best way to solve this issue as artificially using the experimental lattice parameters would introduce empirical parameters and would rely on the material being synthesized.

It was observed that the pseudopotential that was used could affect the frequencies obtained by up to 10% for Au. This is because the pseudopotential fixes the number of electrons that can react to a change in environment. This can be improved by using the most transferable pseudopotentials but this can be computationally expensive.

In general, the other features of the phonon dispersions are in agreement with those found for the various crystal structures in the literature with the exception of Nb, which was shown to have a previously unknown low temperature structure in the previous chapter.

7.6.4 Electron-Phonon Coupling

The electron-phonon coupling is found to be within 28% of the experimental values, which themselves have a large uncertainty[59]. This is a reasonable error considering the approximations that were made in computing these values.

The reduced phonon frequencies from the slightly longer bond lengths will directly lead to higher values of the electron-phonon coupling as both the matrix elements and the electron phonon coupling are both weighted by a factor of $\frac{1}{\omega}$. Any downward shift in the frequencies will cause a corresponding increase in the Eliashberg spectral function and an even larger effect in the electron-phonon coupling constant, λ.

The superconducting transition temperatures are very sensitive to the exact value of λ due to the exponential in the McMillan formula and small changes in the coupling constant could change the transition temperature by an order of magnitude for the more weakly coupling elements.

There will also be higher order anharmonic effects in real crystals which will act as to disperse phonon modes and so will decrease the strength of the coupling and cannot be considered properly within the harmonic approximation. It would be possible to calculate higher order terms for the electron-phonon coupling but these would be very computationally expensive.

There is also a reasonable amount of vagueness in the literature over values for the coulomb constant μ^*[70]. It is often used as a fitting parameter or inferred from the transition temperatures. Computational power is approaching the point where we are able to calculate these directly from first principles which should give a more self-consistent calculation of the transition temperatures[71].

7.7 Conclusion

Density functional perturbation theory can be used as a guide as to the strength of electron-phonon coupling in a material. A large difference may be observed between calculated and experimental estimates which may be due to several effects. Overall, these results indicate that it is possible to use this method to determine whether a material is a good candidate for BCS superconductivity.

Anharmonic phonon effects may dampen interactions between electrons thus reducing the effective electron-phonon coupling in the McMillan formula. This is in agreement with the observation that for Nb, the electron-phonon coupling as measured by tunnelling experiments is in much better agreement with the calculated values.

It is found that for Au which is not observed to be superconducting, the transition temperature is found to be extremely small. The superconducting elements Nb, Mo and Zr are calculated to have electron-phonon coupling constants that are within a factor of 2 from the experimental estimates.

Further experimental tunnelling spectroscopy data for these elements would be useful as to compare with the theoretical predictions as these allow the electron-phonon coupling to be measured directly.

Chapter 8

Nb_3Sn under Uni-Axial Strain

The two most commonly used research and commercial superconductors are NbTi and Nb_3Sn[72]. The most common, NbTi, is a ductile alloy that is easy to manufacture and draw into wires with an upper critical field of 15 T[73]. Nb_3Sn on the other hand is an crystalline ceramic material and so is brittle and more difficult to manufacture with. The main advantage is that it has an upper critical field of 30 T which allows the production of much stronger magnetic fields than NbTi. As research and commercial applications demand higher magnetic fields, there is a trend towards the use of Nb_3Sn magnets. Indeed, Nb_3Sn is the material of choice for the toroidal field magnets in the ITER fusion tokamak[74]. In this chapter, we will examine the structure of Nb_3Sn and perform DFPT calculations to study the effects of strain on the material in these situations.

8.1 Background

Due to the brittle nature of Nb_3Sn, it is normally encased as a powder in a metallic matrix which is normally made of Cu with a Cr barrier[72][75]. This matrix, shown in figure 8.1 provides support for the material itself, and

also offer a route for current to flow if there is a quench of the magnet that could otherwise damage the superconducting strands.

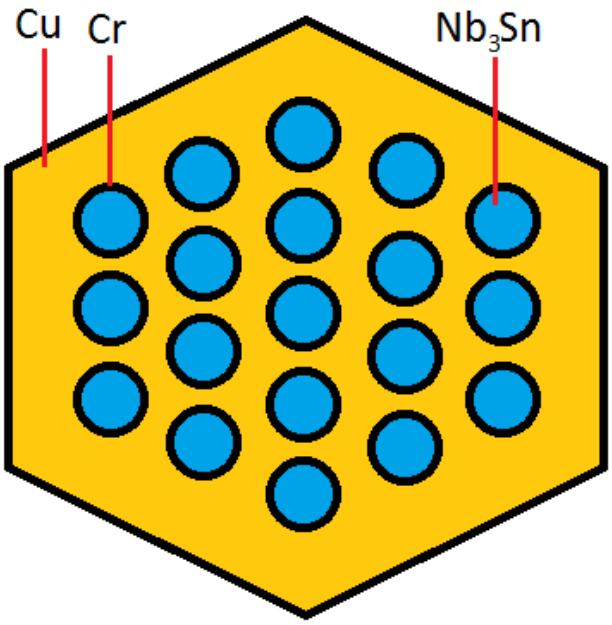

Figure 8.1: Schematic of one of the common structures for Nb_3Sn wires.

In producing a magnet, wires made from this matrix are wound around a core and then heat treated to cause the Nb_3Sn powder to form a polycrystalline superconductor[74]. As discussed in chapter 5, there is a resistive effect due to grain boundaries in the material and so large crystals are preferable as they prevent current decay and ohmic heating but this is offset by the need to sustain high magnetic fields[76].

Due to this heating process, various sections of the material including the Cu sheath expand at different rates. When the material is cooled to room temperature, and further to the superconducting transition, the Nb_3Sn is strained within the wire[47]. This means that even when no external stress is present, the strain on the superconducting material is not zero.

One area of interest is the response of the material to stresses caused by

the magnetic field acting upon the wires when they are used in a magnet[75]. These stresses cause the material to stretch or compress and the induced effects on the superconducting parameters are not fully understood.

8.2 Strain

8.3 Literature Review

The experimental relationship between strain and superconducting properties has been studied by many groups[77][75]. In particular, D.M.J. Taylor et al.[78] performed external strain measurements on single strands of Nb_3Sn. They found a decrease in T_c of approximately $20 \pm 5\%$ at 1.2% strain, but their wires contained additional strains from manufacturing that were not taken into account. Higher than this, the deformation was found to be non-reversible and the superconducting properties of the unstressed material were not recovered as the material was damaged, for example, the polycrystalline layer physically being torn apart.

A. Nijhuis et al[75] have estimated the thermal pre-strain on commercially available Nb_3Sn wires to be in the range -0.014% to -0.58% depending on the exact configuration of the containing wire and the heat treatment. These present experimental difficulties in understanding which effects are due to the Nb_3Sn itself, which are due to the polycrystalline nature of the Nb_3Sn and which are due to mechanical interactions with the Cu cladding.

Previous calculations have been performed by De Marzi et al[79], show the general features that are seen experimentally, namely the drop in superconducting properties away from the unstrained unit cell, but there are several issues with this paper. The electronic properties appear underconverged and the Fermi energy is not correctly positioned on a peak. The

decrease in superconducting properties is only about half of what is seen experimentally which may be due to these issues, as it is not possible for the DOS at the Fermi energy to decrease by as much as if it were higher.

As the experimental work is so problematic, we must turn to theory to separate the effects of the material itself and the way it was produced. We will investigate the superconducting crystal itself so as to test the intrinsic strain function of Nb_3Sn, which will allow experimentalists a deeper understanding of which properties come from bulk properties and which are due to grain effects.

8.3.1 Method

Density functional theory calculations were performed initially on ground state unit cells of Nb_3Sn(figure 8.2) with strains between -1.0% and $+0.5\%$

It was found that a 500 eV cutoff was sufficient to converge the total energy to less than 10 meV. A Brillouin zone sampling grid of $8 \times 8 \times 8$ was similarly sufficient to achieve this level of accuracy.

Initially, a unit cell of Nb_3Sn was relaxed to find the ground state geometry with no strain. This was to allow us to observe the unstrained state of the material and to gain some insights to basic physical properties. Phonon convergence tests were performed on this unit cell to get appropriate values to use for the strained materials. This was done by increasing the basis set size, the Brillouin zone sampling and the real-space grid size until there was little change in the phonon spectrum. A series of finite displacement calculations were also performed to get the elastic constants for the material. This allowed the speed of sound along various phonon branches to be compared.

A range of 10 unit cells with strain values from -1% to +0.5% were created using this perfect unit cell by setting the c-axis to appropriate values

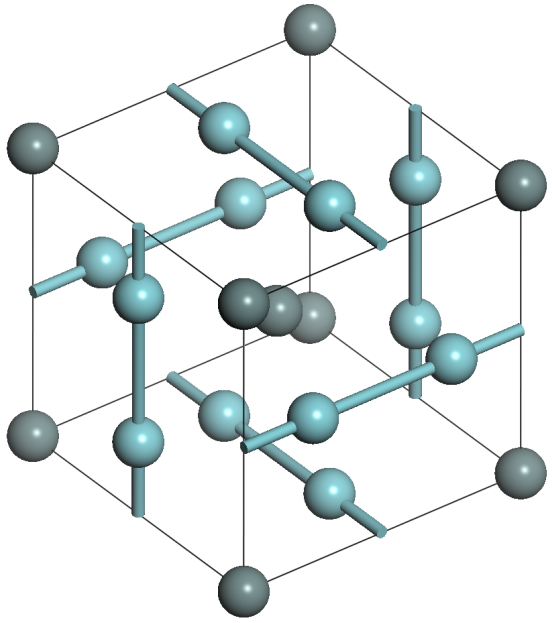

Figure 8.2: Crystal structure of Nb_3Sn which consists of a bcc Sn cell with Nb ribbons running along the edges.

to give strains relative to the unstrained cell. These cells were then allowed to relax with this axis fixed to find the lowest energy atomic configuration for each strain state.

Using the separation of the Eliashberg spectral function that was discussed in the previous chapter, the DOS and phononic contributions were then calculated. A density of states calculation was performed at a fine grid of $40 \times 40 \times 40$ points in the Brillouin zone to find the density of states at the Fermi energy, N_0.

The phonon spectrum was calculated at a $4 \times 4 \times 4$, grid of wavevectors across the Brillouin zone. These were then interpolated to get an accurate sampling of the phonon spectrum, $\tilde{F}(\omega)$. It was found for these calculations that the reciprocal-space grid had to be increased to $12 \times 12 \times 12$ and the real-

space density grid had to be increased to 4 times that of the wavefunctions to avoid unphysical symmetry breaking in the dynamical matrix and to improve the accuracy of the Γ-point IFCs so that the sum rules could be applied.

Due to the large number of possible scattering events in this material, it is infeasible to calculate the EP matrix elements themselves. For simple metals, coupling is strong between most of the low energy phonons, but due to the vast number of modes available in Nb_3Sn (figure 8.4) and the necessity of calculating matrix elements for every one, the calculation is computationally prohibitive. This is primarily due to the computational time to perform even a single perturbative calculation, and that up to 24 perturbations may be required to produce the matrix elements for a single phonon wavevector. Additionally, we are interested in the fully converged spectral functions, and we would need a huge number of these matrix-elements to achieve that, and unlike the direct phonon case interpolation is not possible, and so these matrix elements are assumed to remain constant across the perturbations.

8.3.2 Results

Unstrained cell

The lowest energy unstrained unit cell was found to be cubic with a lattice constant of 5.359 Å which is compared with the experimentally measured value of 5.25±0.3 Å. Further attempts to improve the accuracy by increasing the basis size to 800 eV, increasing the Brillouin zone sampling to $14\times14\times14$ and decreasing the electronic smearing to a tiny value did not affect this.

The band structure and density of states for Nb_3Sn is shown in figure 8.3. There are a collection of 6 bands which cross the Fermi level at different points in the Brillouin zone. The Fermi surface for these is shown

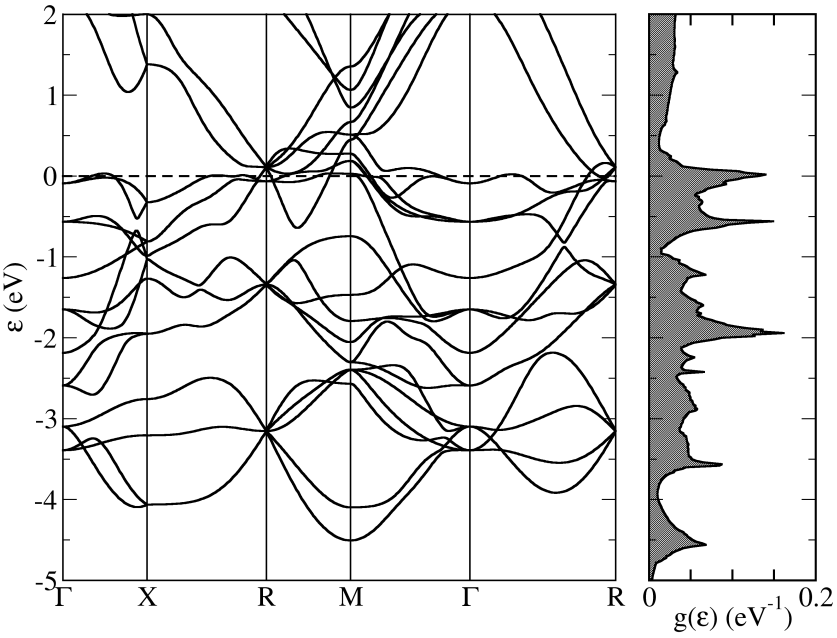

Figure 8.3: The band structure and density of states for cubic Nb_3Sn for a path across the Brillouin zone.

in figure 8.4. Nb_3Sn is interesting because of the large amount of nesting that is possible by the large regions of the Brillouin zone that lie on the Fermi surface. These sheets are close together and so low energy accoustic phonons can cause scattering events between them. These low energy scattering modes are the most important as they are the most common at low energies.

The large number of bands around the Fermi energy give rise to a large density of states at the Fermi energy as shown in figure 8.3. The Fermi energy is shown to lie just on a peak in the density of states and this gives rise to an anomalously large value for N_0 of $0.14\,\mathrm{eV}^{-1}\mathrm{Å}^{-3}$

The phonon spectrum for the unstrained unit cell is shown in figure 8.5. There are 24 separate phonon branches for this material with the majority lying above 50 cm^{-1} and so there are many possible electron-phonon interac-

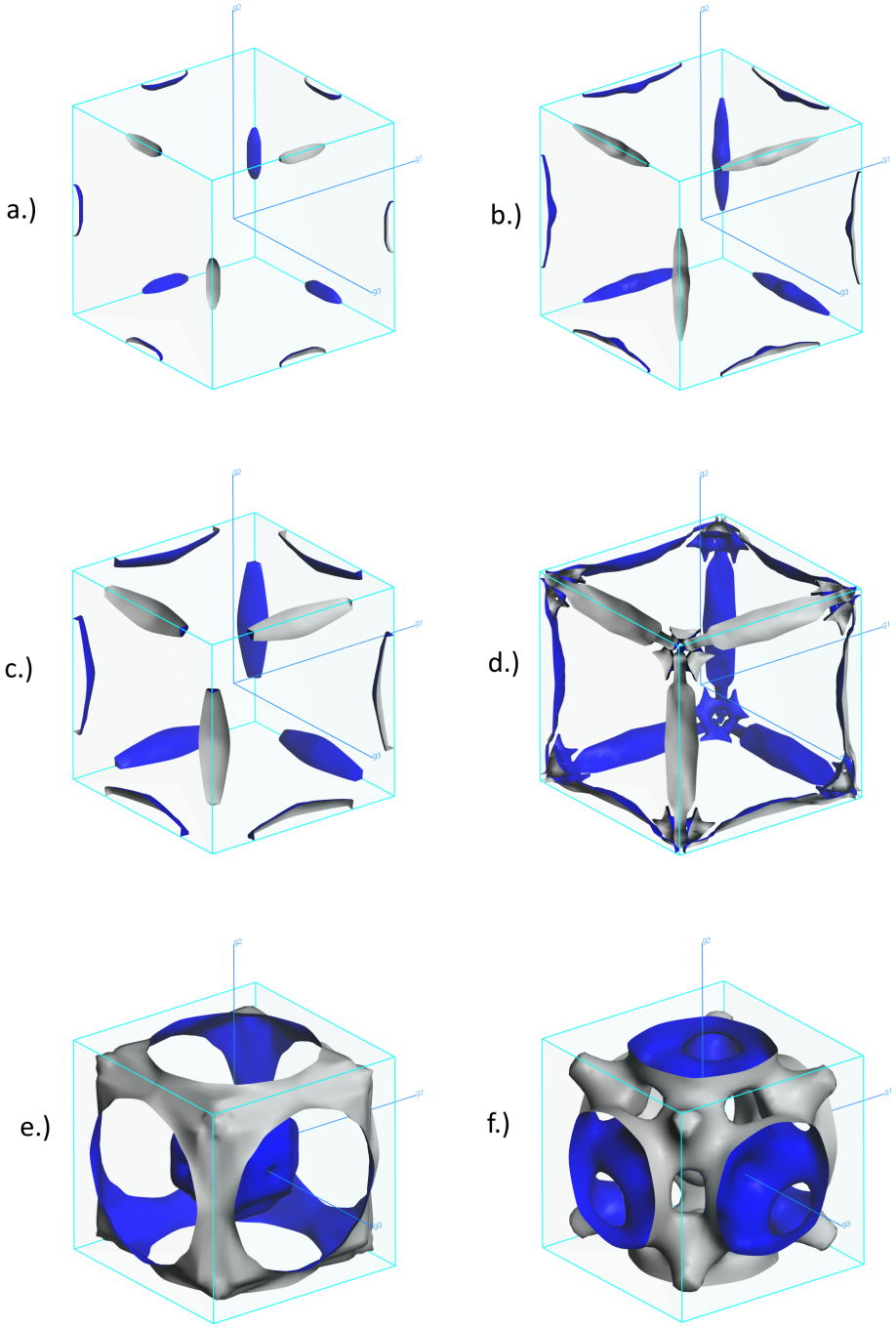

Figure 8.4: The Fermi surface for Nb_3Sn with bands going from a.) lowest to f.) highest Kohn-Sham index. Of note are the similar bands around the edges of the BZ which are almost parallel and close together which allow additional low energy scattering interactions. This calculation was performed with a $40 \times 40 \times 40$ MP grid across the BZ.

tions for each pair of points on the Fermi surface. The modes of the bands in the central cluster between 50 cm^{-1} and 150 cm^{-1} involve excitations along the Nb chains. Only the lowest and highest phonon modes involve the Sn atoms moving to any large extent. The phonon modes calculated agree with the finite displacement calculation of the accoustic modes around the Γ-point.

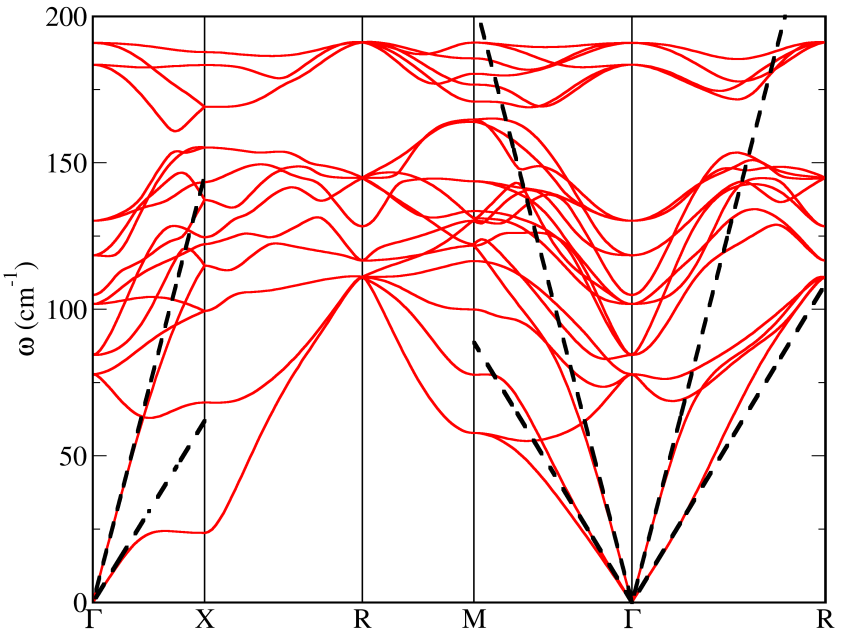

Figure 8.5: The phonon dispersion spectrum for cubic Nb_3Sn is shown in red for a path across the Brillouin zone. The dashed lines indicate accoustic modes around the Γ-point that were calculated by the linear displacement method. The lower of these modes is the transverse accoustic mode and the higher mode is the longitudinal mode (speed of sound).

Examining the phonon modes at the Γ point, we find that the lowest modes which tend to zero are the acoustic branches as would be expected. The next branches contains optical modes where the sheets of the material are out of phase and slide past each other. The next collection of modes involve mainly the Nb ribbon bands which run along the edges of the unit

cell which can vibrate in various ways with no motion of the Sn atoms. Finally the top phonon modes are similar to the lowest optical branch but the wave travels longitudinally.

8.3.3 Strain

Geometry

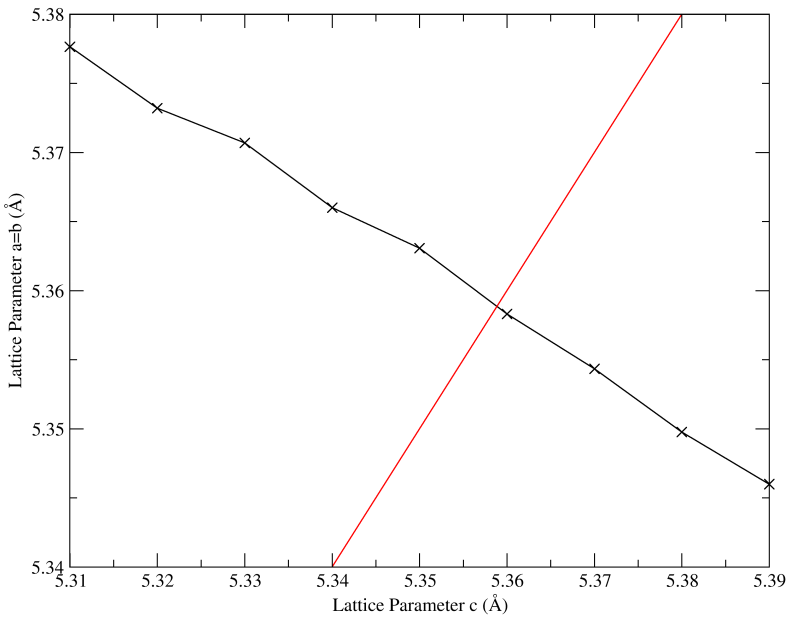

Figure 8.6: The unrestricted lattice parameter compared with the fixed (strained) lattice parameter. Shown in red is the line where the lattice parameters are equal.

The dependence of the a and b axes compared with the strain on the c-axis are shown in figure 8.6. The unit cell volume increased gradually across the region of strain but the change was only 0.3% between the smallest and largest unit cell volumes. The Poisson ratio was calculated to be 0.38 ± 0.02 which is close to the experimental value of 0.36[80]. For the discussion here, we will refer to the point where all the axes are equal at the cubic point.

Internally, the effect of the strain is to break the symmetry between the three sets of Nb ribbons that are parallel to the Cartesian axes. The atoms along the x-axis, which are located at $(\pm 0.25, 0.5, 0)$, are shifted to $(\pm(0.25-\delta), 0.5, 0)$ and those along the y-axis $(0, \pm 0.25, 0.5)$ move to $(0, \pm(0.25+\delta), 0.5)$ as shown in figure 8.7. A comparison of δ and the strain can be seen in figure 8.7. At zero strain, as expected, the value of δ is 0. As the magnitude of the strain increases, so does the value of delta. The only exception is at the strain of -0.541% and this corresponds to a slight deviation from the straight line in the lattice parameters at 5.34Å.

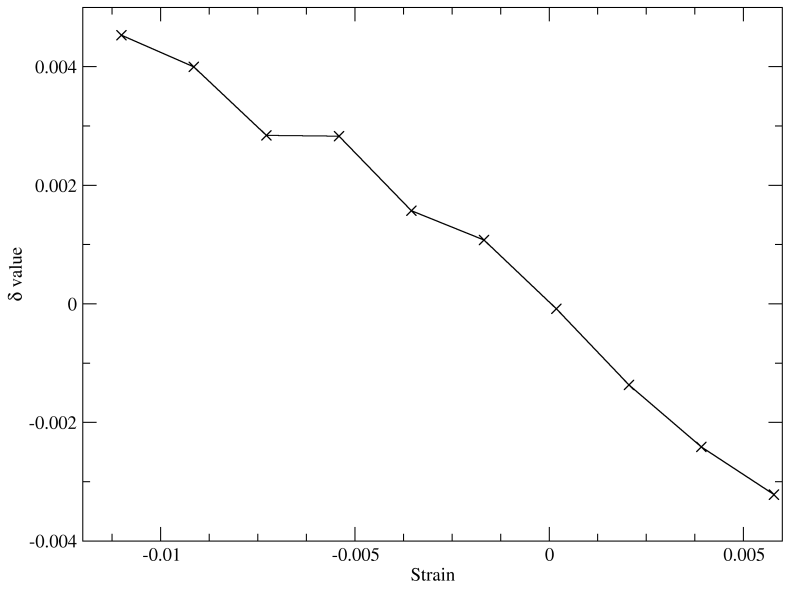

Figure 8.7: Comparison of the δ value (a measure of the distortion of the Nb ribbons) with the strain for the full range of pressures.

Density of states

The density of states for the near zero strain case is shown in comparison to the compression and tension strains in figures 8.8 and 8.9. For both

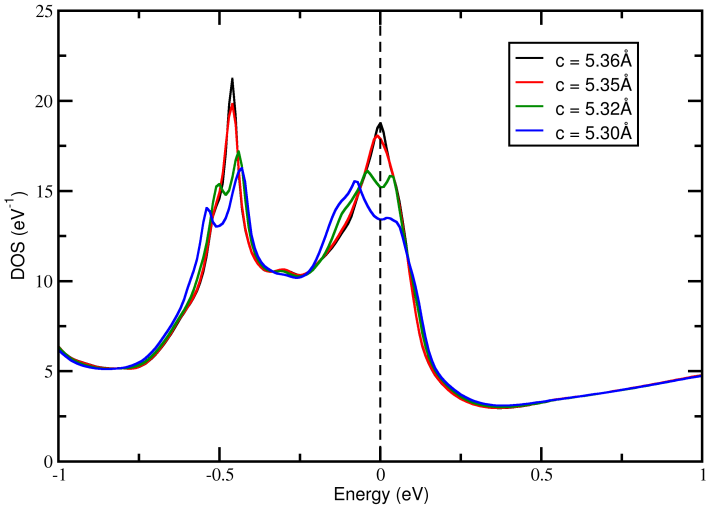

Figure 8.8: A sample of the DOS around the Fermi energy with decreasing strain values from the cubic point, calculated by sampling the Brillouin zone on a grid of $40 \times 40 \times 40$

increasing and decreasing strain, the effect is to break the symmetry between orbitals in different directions. This causes the states about the Fermi energy to begin to separate in energy and so reduces the single high peak into two separate peaks, each either side of the Fermi energy. The effect is fairly symmetric around the cubic lattice values. To first order, the electron-phonon coupling constant is proportional to the density of states at the Fermi energy and this quantity in shown in figure 8.10

8.3.4 Phonon Spectral Function

The phonon density of states between points on the Fermi surface is shown in figures 8.11 and 8.13 for a subset of the stresses calculated moving away from the cubic lattice point.

Looking in detail as Nb_3Sn moves into compression, the phonon frequen-

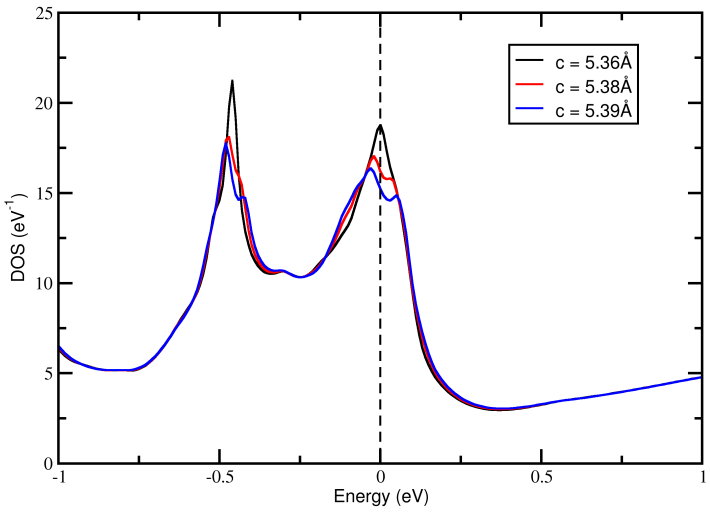

Figure 8.9: A sample of the DOS around the Fermi energy with increasing strain values from the cubic point calculated by sampling the Brillouin zone on a grid of $40 \times 40 \times 40$

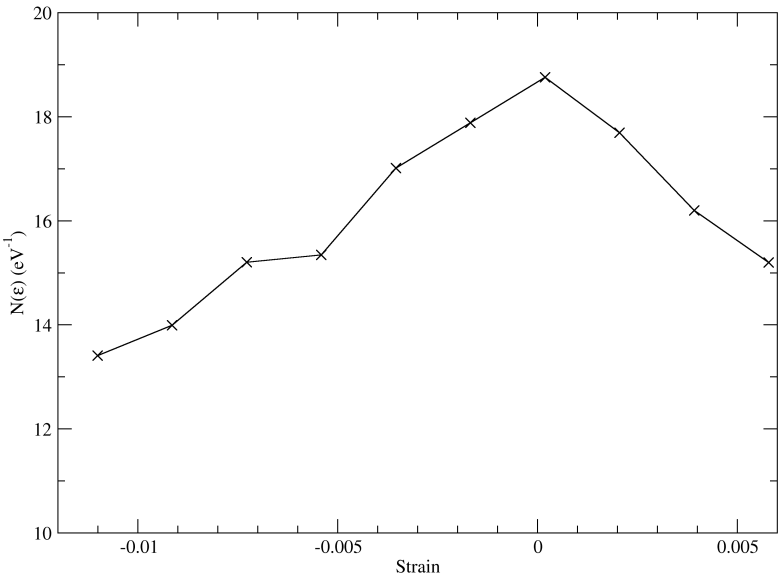

Figure 8.10: The overall effect of strain on the DOS at the Fermi energy in Nb_3Sn for the range of strain values from -1% to $+0.5\%$

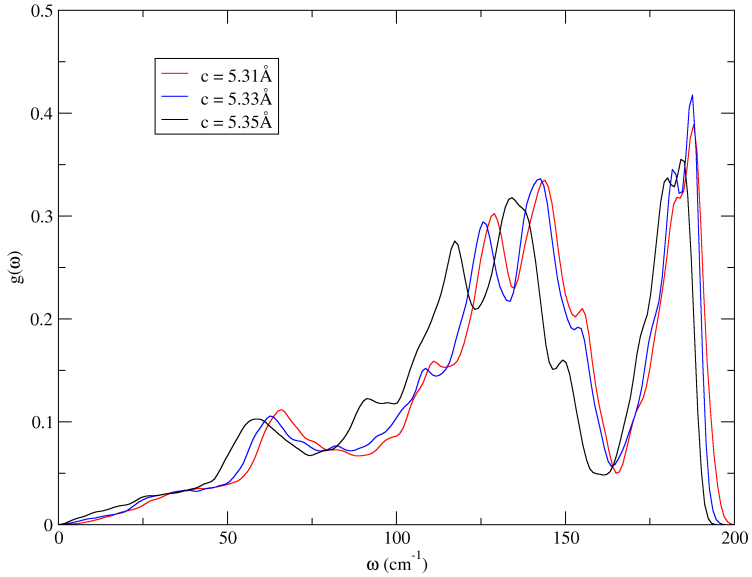

Figure 8.11: The phonon spectral function, $F(\omega)$ for decreasing values of the strain from just below the cubic point. These values were interpolated from a grid of $4 \times 4 \times 4$ samples of the 2nd order energy across the Brillouin zone.

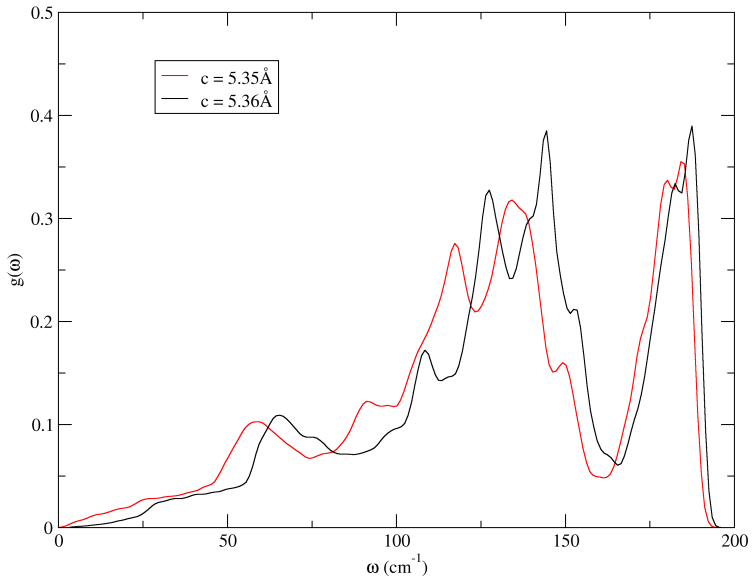

Figure 8.12: The phonon spectral function, $F(\omega)$ for values approaching the cubic point from compression. These values were interpolated from a grid of $4 \times 4 \times 4$ samples of the 2^{nd} order energy across the Brillouin zone.

cies are pushed higher, but the general structure remains fairly unchanged other than a broadening of the peaks. The effect is fairly smooth which should lead to a steady decrease in the EP coupling due to the weighting in the Eliashberg spectral function of $\frac{1}{\omega}$

There is a rapid change that occurs at strains close to the cubic point which is shown in figure 8.12. There is a large increase in frequency of all the modes which leads to a decrease in the coupling strength.

With the exception of the anomaly near the cubic point, the increase in strain pushes the frequency gradually higher as the anisotropy increases at approximately the same rate than in the compression regime. Again the peaks begin to split and separate as the degeneracy is further broken.

Finally we show the value of our integrated spectral function $\int \tilde{F}(\omega) d\omega$ in figure 8.14. The integral increases approaching the cubic point, but has

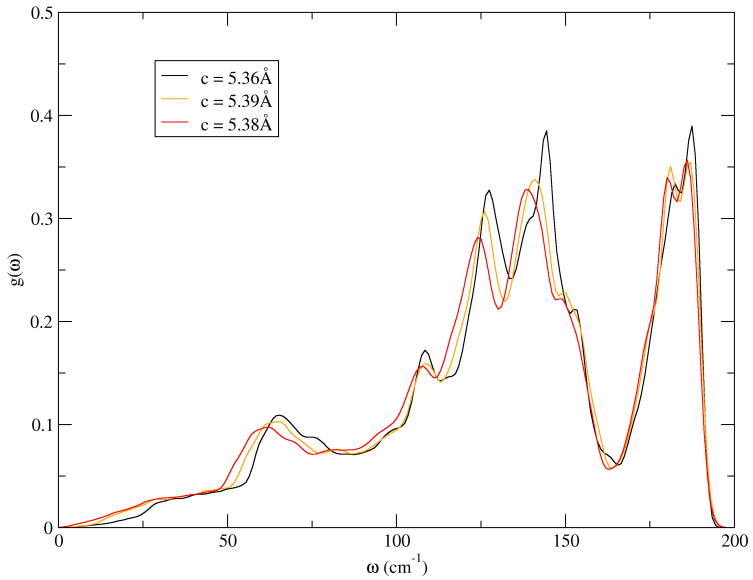

Figure 8.13: The phonon spectral function, $F(\omega)$ for increasing values of the strain from the cubic point. These values were interpolated from a grid of $4 \times 4 \times 4$ samples of the 2nd order energy across the Brillouin zone.

a large drop at the cubic point and has decreased values above that. This was repeated for several values of strains close to that of the drop which all confirmed this sudden change around the cubic point.

Overall Effect of Strain

Combining the effects on the density of states and the phonon spectral function on the electron-phonon coupling constant we arrive at figure 8.15. It is calculated for slight uniaxial compression, the coupling should increase by 10% after which it decreases rapidly. Under tension, the EP coupling gradually decreases from the cubic point.

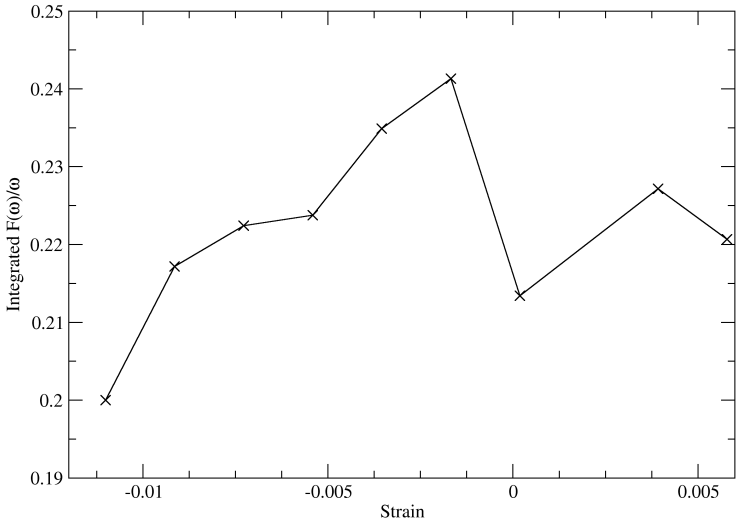

Figure 8.14: The value of $\int \frac{F(\omega)}{\omega} d\omega$ plotted against the strain.

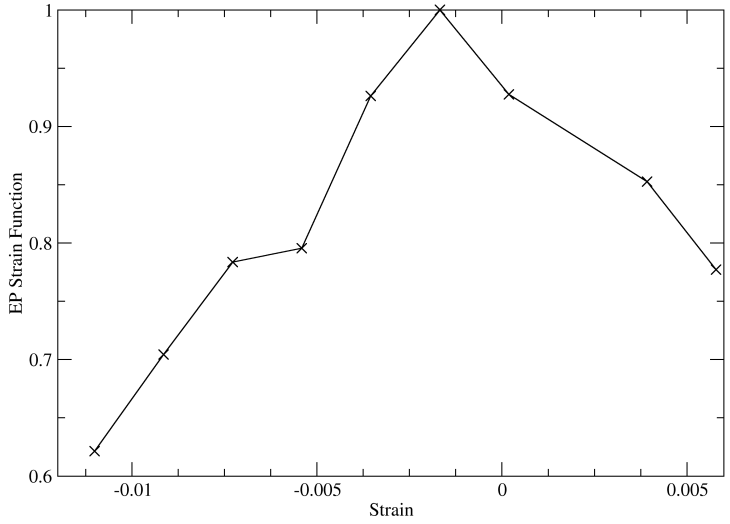

Figure 8.15: The electron-phonon strain function for Nb_3Sn around the cubic point. These values have been normalised to the highest value as that is commonly used as the zero strain point in experimental work.

8.3.5 Discussion

Unstrained cell

The exchange-correlation functional, PBE, is known[6] to underestimate bond energies and so overestimate bond lengths in many materials compared with the all-electron results. The deviation from the experimental value is not very large and so it can be reasonably expected that the electronic structure is a good approximation to the full interacting electronic states. The lack of any structural changes with respect to the basis set size and the Brillouin zone sampling indicate the ground state is converged with respect to these parameters.

The position of the Fermi energy on a peak is in agreement with the band structure which shows a collection of bands which are flat at this energy.

The large number of bands crossing the Fermi energy create a complicated structure for the Fermi surface with 6 separate sheets. There is a fair amount of nesting possible due to parallel regions of different bands. The fact that the Fermi energy lies directly on a peak, means that any translation of the Fermi energy or increase in disorder in the material which causes a smearing of these energy levels, can drastically affect the density of states at the Fermi energy. It also suggests an easy mechanism for the superconducting properties to be affected by the strain.

The large number of phonon modes offer a wide variety of different scattering potentials to contribute to the electron-phonon coupling. However, most of these will be optical modes and so contribute less due to the inverse frequency weighting of the Eliashberg spectral function. The positioning of the lowest peak has the biggest effect on the coupling strength.

8.3.6 Strain

Geometry

The increasing value of δ with increasing lattice asymmetry is in agreement with previous studies[51] on the tetragonal transition in Nb_3Sn where the tetragonal transition was shown to cause this kind of distortion in the atomic structure. This allows the atoms to pack together better in clusters and keeps the electrons forming bonds in the regions of lower nuclear potential.

Density of States

The changes in the density of states can be almost entirely ascribed to symmetry breaking. As the atoms are pushed further from the symmetry positions, the previously degenerate energy levels are pushed further apart. The fact that the Fermi energy lies on a peak amplifies this change.

The shape of the Fermi surface is not changed significantly as the bands are only slightly shifted in energy by a small amount which generally only changes the points in the BZ by a distance inversely proportional to the gradient of the band. As the bands change very rapidly in energy above and below the Fermi energy, these changes in position of the Fermi surface are small and so visually there is no significant change.

Phonon Spectral Function

As the magnitude of the strain is increased in compression, the phonon frequencies are shifted to higher values. This indicates that the screened interatomic potentials are higher order than quadratic in this region, as otherwise the phonon frequencies would not change, and as such the atoms are experiencing different environments. In compression, we see the bonds

along the z-direction being compressed and so the potential well is more sharply defined as the atom has a smaller region in this direction in which to move. Due to the Pauli exclusion and Coulomb repulsion as we attempt to push electrons closer together in a bond, the energy will increase. This leads to higher interatomic force constants and thus phonon frequencies. Conversely, the atoms that have been pulled apart will lie in more flat wells as they have a larger region of space to move in. This will decrease the energy of these modes. The more strain that is applied, the bigger the difference between these compressed and decompressed directions will be.

The phonon frequencies show a large increase in energy and a corresponding drop in the electron-phonon coupling constant as the material is brought through the cubic point from compression into tension. The gradual decreasing of the non-strained lattice parameters causes the atoms to move slightly closer together parallel to the strain and further apart in the directions perpendicular to the strain.

This gradual change will not change the shape of the dynamical matrix eigenvectors significantly until there is a change in the symmetry of the dynamical matrix. Once the lattice constants move through the cubic point, there is a change in form of the eigenvectors as the system goes from having one axis shorter than two others to having one axis longer than the others as well as δ switching signs from negative to positive. The interatomic potentials in the longer directions will have less curvature as the atoms are physically further apart and so modes can be of lower energy than in the cubic form.

As the most important phonon modes for superconductivity are the lowest modes which are those of sheets sliding over one another, we consider the effect of strain upon them. As the strain is increased, the magnitude of

δ increases, disturbing the sheet-like structure of the material. Small values of δ may decrease the strength of linking between sheets but not bring the atoms so far out of the plane as to repel against others from neighbouring sheets in this motion. This would decrease the phonon frequency by lowering the interatomic forces between these sheets. It would also give the Nb atom more degrees of freedom in the direction of motion as it is no longer trapped by symmetry. When δ becomes larger, the overlap between neighbouring atomic shells in the sheets becomes high and causes the layers to not slide past one another easily thus increasing the energy of these modes.

Strain Function

The overall effects on the strain function are to cause a gradual decrease in electron-phonon coupling away from a maximum. This in turn decreases the strength of any superconducting effect. This maximum lies not at the cubic point, but instead at a slight compression. There is also a slight asymmetry between positive and negative strains from this maximum. The coupling strength decreases much more rapidly with strain in compression than in tension. At a strain of -1%, the coupling constant falls to approximately 66% of the maximum. For strong coupling, T_c is, to first order, proportional to the square root of the electron phonon coupling[59], and this would give an 18.7% drop in the superconducting transition temperature. Experimentally, for a -1% strain, it has been found that the drop in superconducting properties is on the order of 20%[30] and so these are in fairly good agreement.

Comparing these results with experiment is fairly difficult as single crystal Nb_3Sn is very brittle. Experimentally, the Nb_3Sn is created in situ within a matrix of bronze and copper under heating to 1000 K[49]. This often leads

to pre-straining on the crystals due to the differential thermal expansion of the superconducting crystal and the metal matrix which supports it. Furthermore by the polycrystalline nature of the material, the strain may not be applied directly to the superconducting crystal structure itself, but rather to the grain boundaries between them. Both of these make it hard to find experimental data on tension in these materials, as it is not reproducible. Finally, as the material is polycrystalline, it is difficult to compare the effects of a uniaxial strain with a combination of random strains on different grains.

Even ignoring these issues, the consistent drop from a maximum under tension and compression is observed in both experimental data and this computational study. The strain function calculated drops slightly less than the experimental would has found and that difference can be ascribed to polycrystalline effects.

8.4 Conclusions

The lattice constants and ground state values for Nb_3Sn agree with experimental values and those from previous studies. The material has a large number of Fermi surface sheets which cause a large amount of nesting such that almost any lattice vector will link two points on the Fermi surface. The large number of atoms in the unit cell give rise to 24 phonon modes but most of these lie at too high energies to give a strong electron-phonon coupling.

The mode that most strongly adds to the electron-phonon coupling strength is that of the acoustic modes and of the first optical mode which lies at a relatively low wavenumber in the range of 50cm^{-1} to 100cm^{-1} across the Brillouin zone. Furthermore, the phonon frequencies agree with those calculated using a finite displacement method which suggests that for low

phonon amplitudes, the harmonic approximation is valid.

In terms of strain, we find that the the main effect of strain on the unit cell is to create a deformation in the unit cell among the Nb atom ribbons. Those in the directions perpendicular to the strain axis move by $\pm\delta$ from the symmetry positions. The atomic orbitals at the Fermi energy are localised around these atoms meaning that any changes in the environment of these atoms will directly affect the density of states at the Fermi energy. These changes are found to be symmetric around the cubic point (zero strain).

The strain also causes a change in the phonon frequencies by affecting the phonon modes in subtle ways. The lowest phonon modes are due to sheets in the material sliding over each other. Increases in tension lead to a large decrease in the phonon frequencies as more degrees of freedom are introduced and the interactions between neighbouring sheets can be decreased and thus the phonon frequencies decrease. As δ continues to increase, these atoms start to interfere with the sliding of the sheets and the phonon frequencies increase again. There is a more subtle interaction with the phonon modes which causes an asymmetry in the strain function, the exact cause of which is unknown.

Although in many materials, high hydrostatic pressure is used to tweak superconductivity, the effects are not necessarily comparable with uniaxial strain. This is because the material is free to relax in the perpendicular directions to the strain. In the case of Nb_3Sn, it maintains an almost constant volume and so the effects are different enough to not be directly comparable to hydrostatic pressure measurements.

Overall, the strain function shows a maximum at a slight compression on the order of 0.3%. This is on the order of the tetragonal distortion in Nb_3Sn that is often encouraged experimentally using non-stoichiometric ratios to

improve superconducting properties[6]. The strain function calculated decreases slightly slower than that observed experimentally but this may be explained by only part of the strain being applied to the Nb_3Sn bulk, as the polycrystalline structure itself will allow alternative strain relief mechanisms.

Finally, it is hard to determine whether the strong coupling in this material may lead to a physical distortion other than those calculated in the Born-Oppenheimer approximation. The electron-phonon interaction is assumed to be small but in this material it is quite large. Further studies should be performed to attempt to calculate this interaction energy using the electron-phonon spectral function itself but this would require a larger self-consistent cycle combining geometry optimisation and perturbative calculations.

Chapter 9

Conclusion

The aim of this work was to develop and test methods for calculating superconducting parameters from first principles calculations. The theoretical basis for the work was given in chapter 2, reducing the many body Schrödinger equation into several separately solvable parts. Methods to solve the equations for ground state electronic and nuclear properties were given in chapter 3.

Grain boundaries are important in determining the critical current and upper critical field in crystalline superconductors such as Nb_3Sn. Chapter 5 examined the changes to the density of states for idealised symmetric tilt grain boundaries. For Au, which has a slowly varying electronic density of states; the presence of even large amorphous grain boundary regions did not greatly affect the density of states. However, Nb_3Sn showed a drastic reduction in the DOS at the Fermi energy due to the smearing effects of the region of disorder. In terms of local density of states, the grain boundary regions showed a greatly depressed density of electrons at the Fermi energy. In materials like this, the grain boundaries act as barriers to electrons moving across them and this explains the change in superconducting properties

obtained by decreasing the grain size experimentally. This also gives experimentalists a measure of the smallest grain size in Nb_3Sn that will still have a bulk-like region as the effects extended much further into the crystal than was apparently from the atomic positions, and was on the order of 11 Å.

Methods for dealing with the more complicated perturbation equations were developed in chapter 4 and give a practical way to calculate the electron-phonon coupling taking advantage of symmetry to reduce the number of perturbations required. Convergence was also examined and it was shown that the electron-phonon coupling matrix elements converge at approximately the same rate as the phonon frequencies, although large errors can be caused by incorrect diagonalisation of the dynamical matrix. In general, the phonon frequencies need to be well converged in order to perform accurate electron-phonon coupling calculations. On top of this, a large number of samples of EP matrix elements are needed to achieve convergence in terms of the electron-phonon coupling constant.

One of the standard test cases for electron-phonon coupling (Nb) is examined in chapter 6. It is shown that the commonly accepted literature structure – bcc – is actually unstable at 0 K. Allowing a relaxation of the structure without symmetry constraints, it is seen to convert through a martensitic transition to a rhombohedral structure. The resulting structure is commensurate with experimental measurements of the lattice expansion upon cooling. This indicates that the majority of the theoretical work in the literature which overestimates the electron-phonon coupling constant in the material may be because the incorrect phase was being studied.

The application of these methods to simple metals in chapter 7 showed a large difference in calculated and experimental values of the electron-phonon coupling constant. These values are closer to the experimentally derived

values than the literature values which use LDA. This is most likely due to more accurate lattice parameters given by the use of the GGA in metals. The method is seen to give a good approximation of the strength of the superconducting effect in the material and offers a method to test novel materials for BCS superconductivity.

Finally the effects of strain on the superconducting properties of Nb_3Sn was examined in chapter 8. It is seen that the ground state and electronic properties agree well with experimental values. Uni-axial strain is shown to cause a deformation in the pairs of Nb atoms which run perpendicular to the strain direction. The density of states is reduced for either positive or negative strain from the cubic unit cell. It was found that this deformation in the Nb ribbons would cause an asymmetry in the strain-T_c curve. This suggests that the maximum electron-phonon coupling is actually found at a small compressive strain of 0.15% . This is in contrast to the literature where it is assumed that the peak occurs at zero strain and that any deviation is due to internal strain caused by the manufacturing process. This shows the difficulty experimentally in measuring Nb_3Sn in the complex way that it is formed into wires. The decrease in the superconducting transition temperatures at a strain of -1% was found to be 18.7% which is in good agreement with experimental measurements of approximately 20%.

One clear direction to improve the calculation of electron-phonon coupling would be to implement the interpolation suggested by Guistino et al[23]. This would allow the same style of interpolation that is currently used for the phonon dispersion curves to be used for the electron-phonon matrix elements which would vastly reduce the complexity of the calculations. This would be ideal for further calculations on the strain of Nb_3Sn as the electron-phonon spectrum needs to be well converged in order to make

comparisons between the strain states.

Bibliography

[1] Adam Mann. High-temperature superconductivity at 25: Still in suspense. *Nature*, 475(7356):280–282, jul 2011.

[2] J. Bardeen, L. N. Cooper, and J. R. Schrieffer. Theory of Superconductivity. *Physical Review*, 108(5):1175–1204, dec 1957.

[3] Leon Cooper. Bound Electron Pairs in a Degenerate Fermi Gas. *Physical Review*, 104(4):1189–1190, nov 1956.

[4] J. G. Bednorz and K. A. Muller. Possible high Tc superconductivity in the BaLaCuO system. *Zeitschrift fur Physik B Condensed Matter*, 64(2):189–193, jun 1986.

[5] J. C. Tully. Dynamics of Molecular Collisions. In W. H. Miller, editor, *Dynamics of Molecular Collisions*, pages 217–267. Plenum, New York, 1976.

[6] M. Payne, M. Teter, D. Allan, T. Arias, and J. Joannopoulos. Iterative minimization techniques for ab initio total-energy calculations: molecular dynamics and conjugate gradients. *Reviews of Modern Physics*, 64(4):1045–1097, oct 1992.

[7] P. Hohenberg and W. Kohn. Inhomogeneous Electron Gas. *Physical Review*, 136(3B):B864–B871, nov 1964.

[8] W. Kohn and L. Sham. Self-Consistent Equations Including Exchange and Correlation Effects. *Physical Review*, 140(4A):A1133–A1138, nov 1965.

[9] M. C. Gibson. *Implementation and Application of Advanced Density Functionals*. PhD thesis, University of Durham, 2006.

[10] David Langreth and M. Mehl. Beyond the local-density approximation in calculations of ground-state electronic properties. *Physical Review B*, 28(4):1809–1834, aug 1983.

[11] A. Becke. Density-functional exchange-energy approximation with correct asymptotic behavior. *Physical Review A*, 38(6):3098–3100, sep 1988.

[12] C. Filippi, D. Singh, and C. Umrigar. All-electron local-density and generalized-gradient calculations of the structural properties of semiconductors. *Physical Review B*, 50(20):14947–14951, nov 1994.

[13] Philip Peter Rushton. *Towards a Non-Local Density Functional Description of Exchange and Correlation.* PhD thesis, University of Durham, 2002.

[14] John P. Perdew, Kieron Burke, and Matthias Ernzerhof. Generalized Gradient Approximation Made Simple. *Physical Review Letters*, 77(18):3865–3868, oct 1996.

[15] RP P. Feynman. Forces in Molecules. *Physical Review*, 56(4):340–343, aug 1939.

[16] Stefano Baroni, Stefano de Gironcoli, and Andrea Dal Corso. Phonons and related crystal properties from density-functional perturbation theory. *Reviews of Modern Physics*, 73(2):515–562, jul 2001.

[17] Philip Allen. Fermi-surface harmonics: A general method for nonspherical problems. Application to Boltzmann and Eliashberg equations. *Physical Review B*, 13(4):1416–1427, feb 1976.

[18] C.E. Shannon. Communication in the presence of noise. *Proceedings of the IEEE*, 72(9):1192, 1984.

[19] Hendrik J Monkhorst and James D Pack. Special points for Brillouin-zone integrations. *Physical Review B*, 13(12):5188–5192, jun 1976.

[20] G. P. Kerker. Efficient iteration scheme for self-consistent pseudopotential calculations. *Physical Review B*, 23(6):3082–3084, 1981.

[21] G Kresse and J. Furthmüller. Efficient iterative schemes for ab initio total-energy calculations using a plane-wave basis set. *Physical Review B*, 54(16):11169–11186, 1996.

[22] H. A. Kramers. Théorie générale de la rotation paramagnétique dans les cristaux. *Proceedings Koninklijke Akademie van Wetenschappen*, 33:959–972, 1930.

[23] Feliciano Giustino, J.R. Yates, Ivo Souza, M.L. Cohen, and S.G. Louie. Electron-phonon interaction via electronic and lattice wannier functions: Superconductivity in boron-doped diamond reexamined. *Physical review letters*, 98(4):47005, jan 2007.

[24] Xavier Gonze. First-principles responses of solids to atomic displacements and homogeneous electric fields: Implementation of a conjugate-gradient algorithm. *Physical Review B*, 55(16):10337–10354, 1997.

[25] M. I. Gol'dshtein, B M Bronfin, A. Z. Shifman, and V. V. Osipov. Mechanism of grain boundary strengthening of steels. *Metal Science and Heat Treatment*, 21(2):104–109, feb 1979.

[26] R. Gross and B. Mayer. Transport processes and noise in YBa2Cu3O7−δ grain boundary junctions. *Physica C: Superconductivity*, 180(1-4):235–242, sep 1991.

[27] H Hilgenkamp. Grain boundaries in high-T_ {c} superconductors. *Reviews of Modern Physics*, 74(April):485–549, 2002.

[28] G. Blatter and F. Greuter. Electrical breakdown at semiconductor grain boundaries. *Physical Review B*, 34(12):8555–8572, dec 1986.

[29] C R M Grovenor. Grain boundaries in semiconductors. *Journal of Physics C: Solid State Physics*, 18(21):4079–4119, jul 1985.

[30] David M J Taylor, Maisoon Al-Jawad, and Damian P Hampshire. A new paradigm for fabricating bulk high-field superconductors. *Superconductor Science and Technology*, 21(12):125006, dec 2008.

[31] E. Langmann. Fermi-surface harmonics in the theory of the upper critical field. *Physical Review B*, 46(14):9104–9115, oct 1992.

[32] Murray S. Daw and M. I. Baskes. Embedded-atom method: Derivation and application to impurities, surfaces, and other defects in metals. *Physical Review B*, 29(12):6443–6453, jun 1984.

[33] U. Dahmen, C. J. D. Hetheringtont, M. A. O'Keefe, K. H. Westmacottt, M. J. Mills, M. S. Daw, and V. Vitek. Atomic structure of a Σ99 grain boundary in aluminium: A comparison between atomic-resolution observation and pair-potential and embedded-atom simulations. *Philosophical Magazine Letters*, 62(5):327–335, nov 1990.

[34] Y. Mishin, M. J. Mehl, D. A. Papaconstantopoulos, A. F. Voter, and J. D. Kress. Structural stability and lattice defects in copper: Ab initio, tight-binding, and embedded-atom calculations. *Physical Review B*, 63(22):224106, may 2001.

[35] Ben-hu Zhou, Y. Xu, S. Wang, Guanghui Zhou, and K. Xia. An ab initio investigation on boundary resistance for metallic grains. *Solid State Communications*, 150(29-30):1422–1424, aug 2010.

[36] Alan F. Wright and Susan R. Atlas. Density-functional calculations for grain boundaries in aluminum. *Physical Review B*, 50(20):15248–15260, nov 1994.

[37] Peter Zapol, Michael Sternberg, Larry A. Curtiss, Thomas Frauenheim, and Dieter M. Gruen. Tight-binding molecular-dynamics simulation of impurities in ultrananocrystalline diamond grain boundaries. *Physical Review B*, 65(4):045403, dec 2001.

[38] S. von Alfthan, P. D. Haynes, K. Kaski, and A. P. Sutton. Are the Structures of Twist Grain Boundaries in Silicon Ordered at 0 K? *Physical Review Letters*, 96(5):055505, feb 2006.

[39] Chris-Kriton Skylaris, Peter D Haynes, Arash A Mostofi, and Mike C Payne. Introducing ONETEP: linear-scaling density functional simulations on parallel computers. *The Journal of chemical physics*, 122(8):84119, feb 2005.

[40] P. Chaudhari. Coincidence Twist Boundaries between Crystalline Smoke Particles. *Journal of Applied Physics*, 42(8):3063, 1971.

[41] V. R. Coffman, J. P. Sethna, a. R. Ingraffea, J. E. Bozek, N. P. Bailey, and E. I. Barker. Challenges in Continuum Modelling of Intergranular Fracture. *Strain*, 47:99–104, dec 2011.

[42] A. P. Sutton and R. W. Balluffi. *Interfaces in Crystalline Materials*. Oxford University Press, New York, 1995.

[43] M. Baier, R. Wordel, F.E. Wagner, T.E. Antonova, and V.E. Antonov. Mössbauer study of the hydrides of Nb3Me with A15 structure. *Journal of the Less Common Metals*, 172-174:358–365, aug 1991.

[44] H. J. Niu and D. P. Hampshire. Disordered Nanocrystalline Superconducting PbMo6S8 with a Very Large Upper Critical Field. *Physical Review Letters*, 91(2):027002, jul 2003.

[45] Stephan Lany and Alex Zunger. Accurate prediction of defect properties in density functional supercell calculations. *Modelling and Simulation in Materials Science and Engineering*, 17(8):084002, 2009.

[46] Vinayak Keshavlal Patel. *Lattice constants, thermal expansion coefficients, densities, and imperfections in gold and the alpha-phase of the gold-indium system*. PhD thesis, University of Missouri at Rolla, 1967.

[47] R Flükiger, D Uglietti, V Abächerli, and B Seeber. Asymmetric behaviour of J c (ϵ) in Nb 3 Sn wires and correlation with the stress induced elastic tetragonal distortion. *Superconductor Science and Technology*, 18(12):S416–S423, dec 2005.

[48] M. Needels, A. M. Rappe, P. D. Bristowe, and J. D. Joannopoulos. Ab initio study of a grain boundary in gold. *Physical Review B*, 46(15):9768–9771, oct 1992.

[49] R. Flükiger, D. Uglietti, C. Senatore, and F. Buta. Microstructure, composition and critical current density of superconducting Nb3Sn wires. *Cryogenics*, 48(7-8):293–307, jul 2008.

[50] Philip Allen. Neutron Spectroscopy of Superconductors. *Physical Review B*, 6(7):2577–2579, oct 1972.

[51] W Weber and L. F. Mattheiss. Electronic structure of tetragonal Nb_{3}Sn. *Physical Review B*, 25(4):2270–2284, feb 1982.

[52] B.D. Josephson. Possible new effects in superconductive tunnelling. *Physics Letters*, 1(7):251–253, jul 1962.

[53] Georg Brauer and Jochen Jander. Die Nitride des Niobs. *Zeitschrift fur anorganische und allgemeine Chemier anorganische und allgemeine Chemie*, 270(1-4):160–178, oct 1952.

[54] Svend Erik Rasmussen, Guy Magniez, Jean-Pierre Chaminade, Michel Pouchard, Paul Hagenmuller, and Arne F. Andresen. Preparation of Single Phases and Single Crystals of Niobium–Germanium Compounds. *Acta Chemica Scandinavica*, 31a:79–82, 1977.

[55] M. E. Straumanis and S. Zyszczynski. Lattice parameters, thermal expansion coefficients and densities of Nb, and of solid solutions Nb–O and Nb–N–O and their defect structure. *Journal of Applied Crystallography*, 3(1):1–6, feb 1970.

[56] R. K. Bollinger, B. D. White, J. J. Neumeier, H. R. Z. Sandim, Y. Suzuki, C. A. M. dos Santos, R. Avci, A. Migliori, and J. B. Betts. Observation of a Martensitic Structural Distortion in V, Nb, and Ta. *Physical Review Letters*, 107(7):075503, aug 2011.

[57] Stefano Baroni, Paolo Giannozzi, and Andrea Testa. Green's function approach to linear response in solids. *Physical Review Letters*, 58(18):1861–1864, may 1987.

[58] W. McMillan. Transition Temperature of Strong-Coupled Superconductors. *Physical Review*, 167(2):331–344, mar 1968.

[59] P. B. Allen and R. C. Dynes. Transition temperature of strong-coupled superconductors reanalyzed. *Physical Review B*, 12(3):905–922, aug 1975.

[60] P. Morel and P. W. Anderson. Calculation of the superconducting state parameters with retarded electron-phonon interaction. *Physical Review*, 125(4):1263–1271, 1962.

[61] Lars Hedin. New Method for Calculating the One-Particle Green's Function with Application to the Electron-Gas Problem. *Phys. Rev.*, 139(3A):796, 1947.

[62] Charles P. Poole, Horacio A. Farach, and Richard J. Creswick. *Superconductivity*. Academic Press, Amsterdam, 2007.

[63] Andrew J. Morris, R. J. Nicholls, C. J. Pickard, and Jonathan R. Yates. OptaDOS : A Tool for Obtaining Density of States, Core-level and Optical Spec tra from Electronic Structure Code. *Comp. Phys. Comm.*, 185(5):1477–1485, 2014.

[64] L. Vegard. VI. Results of crystal analysis. *Philosophical Magazine Series 6*, 32(187):65–96, jul 1916.

[65] H. E. Swanson and E. Tatge. Standard X-ray diffraction powder patterns I. *National Bureau of Standards (U.S.), Circular*, 539(1):1–95, 1953.

[66] A. W. Hull. Crystal structure of Ti and Zr. *Physical Review*, 18(2):88–89, 1921.

[67] Cui-E. Hu, Zhao-Yi Zeng, Lin Zhang, Xiang-Rong Chen, and Ling-Cang Cai. Density functional study of the phase diagram and thermodynamic properties of Zr. *Computational Materials Science*, 50(3):835–840, 2011.

[68] E. L. Wolf, John Zasadzinski, G. B. Arnold, D. F. Moore, J. M. Rowell, and M. R. Beasley. Tunneling and the electron-phonon-coupled superconductivity of Nb3Sn. *Physical Review B*, 22(3):1214–1217, aug 1980.

[69] R. Bauer, A. Schmid, P. Pavone, and D. Strauch. Electron-phonon coupling in the metallic elements Al, Au, Na, and Nb: A first-principles study. *Physical Review B*, 57(18):11276–11282, may 1998.

[70] M. Lüders, M. A. L. Marques, N. N. Lathiotakis, A. Floris, G. Profeta, L. Fast, A. Continenza, S. Massidda, and E. K. U. Gross. Ab initio theory of superconductivity. I. Density functional formalism and approximate functionals. *Phys. Rev. B*, 72(2):024545, 2005.

[71] M. A. L. Marques, M. Lüders, N. N. Lathiotakis, G. Profeta, A. Floris, L. Fast, A. Continenza, E. K. U. Gross, and S. Massidda. Ab initio theory of superconductivity. II. Application to elemental metals. *Phys. Rev. B*, 72(2):024546, 2005.

[72] James P. Harbison and J. Bevk. Superconducting and mechanical properties of in situ formed multifilamentary Cu-Nb3Sn composites. *Journal of Applied Physics*, 48(12):5180, 1977.

[73] Jiao Zhengkuan, Chen Zhuomin, Han Hanmin, Wang Futang, Shi Airu, and Han Guchang. Development of stable high field Nb-Ti superconducting magnets. *Cryogenics*, 27(8):416–420, 1987.

[74] D. Ciazynski. Review of Nb3Sn conductors for ITER. *Fusion Engineering and Design*, 82(5-14):488–497, 2007.

[75] A Nijhuis, R P Pompe van Meerdervoort, H J G Krooshoop, W a J Wessel, C Zhou, G Rolando, C Sanabria, P J Lee, D C Larbalestier, A Devred, A Vostner, N Mitchell, Y Takahashi, Y Nabara, T Boutboul, V Tronza, S-H Park, and W Yu. The effect of axial and transverse loading on the transport properties of ITER Nb3Sn strands. *Superconductor Science and Technology*, 26(8):084004, 2013.

[76] Jian Zhou, Younjung Jo, Zu Hawn Sung, Haidong Zhou, Peter J Lee, and David C Larbalestier. Evidence that the upper critical field of Nb 3 Sn is independent of whether it is cubic or tetragonal. *Applied Physics Letters*, 99(12):122507, sep 2011.

[77] A Godeke. A Review of the Properties of Nb3Sn and Their Variation with A15 Composition, Morphology and Strain State. *arXiv*, 94720:1–15, 2008.

[78] David M J Taylor and Damian P Hampshire. The scaling law for the strain dependence of the critical current density in Nb 3 Sn superconducting wires. *Superconductor Science and Technology*, 18(12):S241–S252, dec 2005.

[79] Gianluca De Marzi, L. Morici, Luigi Muzzi, and Marco Buongiorno Nardelli. Strain sensitivity and superconducting properties of Nb3Sn from first principles calculations. *Journal of Physics: Condensed Matter*, 25(13):135702, 2012.

[80] B Bordini, P Alknes, L Bottura, L Rossi, and D Valentinis. An exponential scaling law for the strain dependence of the Nb3Sn critical current density. *Superconductor Science and Technology*, 26:075014, 2013.